

Study on 2K Heat Exchanger for Superfluid Helium Cryogenic Systems of Superconducting Accelerators

Dissertation

For the degree of
DOCTOR OF PHILOSOPHY

By

Ashish Kumar

Department of Accelerator Science

School of High Energy Accelerator Science

The Graduate University for Advanced Studies, SOKENDAI



June, 2020

Supervisor:

Prof. Nakai Hirotaka

Chief Examiner:

Assoc. Prof. Kimura Nobuhiro

Examiners:

Assoc. Prof. Nakanishi Kota

Assoc. Prof. Okamura Takahiro

Assis. Prof. Shimizu Hirotaka

Assis. Prof. Takada Suguru

TABLE OF CONTENTS

Abstract.....	1
Chapter 1. Introduction.....	4
1.1. Particle Accelerators	4
1.1.1. Accelerators based on types of accelerating cavities	5
1.2. Helium as a Coolant for Superconducting Accelerators.....	7
1.2.1. Introduction.....	7
1.2.2. Phase diagram and its specific heat capacity	7
1.2.3. Why superfluid helium for superconducting magnets and cavities?.....	9
1.3. Basics of He II Production.....	12
1.3.1. Normal liquid helium liquefaction	12
1.3.2. He II liquefaction	14
1.3.3. Pumping system for He II	16
1.4. Background on 2K Heat Exchanger Research.....	18
1.5. Motivation.....	21
1.6. Composition of the Thesis	22
Chapter 2. Superfluid Helium Cryogenic Systems at KEK.....	24
2.1. Introduction.....	24
2.1.1. Superconducting RF test facility	26
2.1.2. Compact energy recovery linac (cERL).....	29
2.1.3. Pumping system at KEK	31
2.2. 2K Heat Exchanger at KEK.....	33
2.2.1. Laminated-finned type heat exchanger	33
2.2.2. 2K heat exchanger manufacturing procedure.....	35
Chapter 3. Objective of the Study	38
3.1. Performance of the 2K HX_1	38
3.2. Optimization of the 2K HX_1	38

3.3. Assumptions for Heat Transfer Analysis.....	39
Chapter 4. Computational Fluid Dynamics	41
4.1. Introduction.....	41
4.1.1. Governing equations of fluid dynamics	41
4.2. ANSYS CFX® for CFD Analysis	42
4.2.1. Geometry	43
4.2.2. Meshing.....	44
4.2.3. Mesh independency test	46
4.2.4. CFX-Pre setup.....	47
4.2.5. Material properties	47
4.2.6. Domains	48
4.2.7. Boundary conditions	48
4.2.8. Solver Control	50
4.3. Modelling Flow near the Wall.....	51
4.3.1. Heat Flux in the Near-Wall Region.....	54
4.4. Turbulence Modelling.....	55
4.4.1. Two equation turbulence models	55
4.4.2. The k-epsilon model in ANSYS CFX.....	56
4.4.3. The k-omega model in ANSYS CFX.....	57
4.4.4. The Wilcox k- ω model.....	58
4.4.5. The baseline (BSL) k- ω model.....	59
4.4.6. The shear stress transport model (SST).....	60
4.4.7. Selection of the turbulence model for the 2K HX geometry.....	61
Chapter 5. Methodology for Effectiveness Determination of 2K HX.....	63
5.1. Logarithmic Mean Temperature Difference (LMTD) Method.....	63
5.2. Effectiveness of a Heat Exchanger	65
5.2.1. Effectiveness with variable thermo-physical properties	67
5.3. Fin Efficiency	69
5.3.1. Fin efficiency for the 2K HX_1 fin.....	70
5.3.2. Overall surface efficiency	71

5.4. Effect of Longitudinal Conduction on Effectiveness	72
5.4.1. Longitudinal conduction effect on 2K HX_1	74
5.5. Thermal Conductivity of OFC	75
5.5.1. Experimental determination of RRR for a copper fin	75
5.6. Thermo-Physical Properties for Helium	77
5.6.1. Heat transfer coefficient for GHe	78
5.6.2. Colburn and friction factor for the GHe flowing through 2K HX	81
5.6.3. Heat transfer coefficient and pressure drop for LHe	83
Chapter 6. Experimental and Numerical Investigation of the 2K HX_1	85
6.1. Heat Exchanger Test Stand	85
6.1.1. Flow control	86
6.1.2. Temperature and pressure sensors	87
6.1.3. Instrumentation	88
6.2. Studies Conducted to Improve the Heat Exchanger Test Stand	90
6.2.1. Thermometry	91
6.2.2. Thermo-acoustic oscillations in pressure sensing tubes	94
6.3. Experimental Procedure	96
6.4. Results and Discussion	97
6.4.1. 2K HX_1 experimental result	98
6.4.2. Flow meter accuracy measurement	102
6.5. Performance of the 2K HX_1	103
6.5.1. 2K HX_1 numerical model	104
6.5.2. Results and discussion	105
6.5.3. GHe flow behavior through 2K HX_1	108
Chapter 7. Parametric Study of the 2K HX_1	111
7.1. Objective	111
7.2. Parameters for the Design Study	113
7.3. Results and Discussion	115
7.3.1. Effect of the bypass area and helical angle	115
7.3.2. Effect of helical pitch	121

7.3.3. Improved designs for the 2K HX	122
7.3.4. Improved 2K HX without axial length restriction	125
Chapter 8. Optimization of the Superfluid Helium Cryogenic Systems at KEK	128
8.1. Objective	128
8.2. Effect of the GHe Pressure Drop on the Pumping System Capacity	129
8.3. Optimized 2K HX for the Cryogenic Systems at KEK	131
Chapter 9. Experimental and Numerical Verification of the Optimization Study	135
9.1. 2K Heat Exchanger for Experimental Verification	135
9.2. Experimental Results	137
9.3. Comparison of the Numerical and Experimental Results for the 2K HX_2	139
Chapter 10. Conclusion	141
Chapter 11. Suggestion for Further Improvement.....	143
References	144
Acknowledgments	149
Appendices	150

LIST OF FIGURES

Figure 1-1: Linear accelerator at SLAC, Stanford, USA [42].	4
Figure 1-2: Circular accelerator at KEK, Japan [43].	5
Figure 1-3: A 9-Cell 1.3 GHz superconducting cavity.	6
Figure 1-4: Phase diagram for helium.	8
Figure 1-5: Specific heat capacity of liquid helium as a function of temperature (T): Lambda point).	9
Figure 1-6: Basic layout of the helium liquefier for the SuperKEKB accelerator.	13
Figure 1-7: T-S diagram of the SuperKEKB helium cryogenic system.	14
Figure 1-8: T-S diagram for the He II production with and without subcooling.	15
Figure 1-9: Basic layout for the He II production system with and without heat exchanger.	16
Figure 1-10: Various types of the He II liquefaction cycles [8].	17
Figure 1-11: Different types of the 2K heat exchangers tested for CERN cryogenic system.	19
Figure 1-12: Coil-Finned 2K heat exchanger for vertical test cryostat at XFEL, DESY [16].	20
Figure 1-13: Optimal operating temperature for a superconducting cavity [8].	21
Figure 2-1: A schematic illustration of the superfluid helium cryogenic system at KEK.	25
Figure 2-2: Layout of the superconducting test facility for International Linear collider cryomodule testing at KEK.	27
Figure 2-3: Schematic illustration of the cryogenic system for STF facility.	28
Figure 2-4: ILC cryomodule testing at the STF facility.	28
Figure 2-5: Layout of the cERL facility at KEK.	29
Figure 2-6: Schematic illustration of the cryogenic system for cERL facility.	30
Figure 2-7: Pumping capacity of the cryogenic systems with respect to the inlet pressure to the pumps for 2.0 K operation.	31

Figure 2-8: Pumping capacity of the cERL pumping system for the Main Linac 2K Cold box operation.	32
Figure 2-9: Cross section of the 2K HX_1 (on the left) and its helically coiled tube (on the right).	34
Figure 2-10: 2K heat exchanger manufacturing process	37
Figure 4-1: Flow diagram for numerical analysis on ANSYS CFX.....	43
Figure 4-2: 2K heat exchanger CAD geometry from AutoDesk Inventor®	44
Figure 4-3: Inflation and Proximity mesh around Fins.	45
Figure 4-4: Y^+ for different region of turbulent boundary layer [28].....	54
Figure 5-1: Heat transfer through a differential element of a heat exchanger between hot and cold fluid.	63
Figure 5-2: Temperature profile for a counterflow heat exchanger.	64
Figure 5-3: Specific heat capacity variation with respect to temperature for LHe and GHe.	67
Figure 5-4: Fin efficiencies for annular and straight fins [11].	70
Figure 5-5: Fin structure employed for the 2K HX_1.	71
Figure 5-6: Experimental setup for RRR measurement at KEK (left) ; 4 wire RRR measurement on the OFC fin (right).....	76
Figure 5-7: Thermal conductivity versus temperature for OFC.	77
Figure 5-8: Gaseous helium flow through the stacked fins along helical tube.....	79
Figure 5-9: Example of the CFD model for the 2K HX.	80
Figure 5-10: a) 2K heat exchanger geometry in a SS316L shell (left), b) Volume surrounding the 2K Heat exchanger body (right).	82
Figure 6-1: Joule-Thomson valve tip for level and pressure control.....	87
Figure 6-2: Schematic diagram of the 2K heat exchanger test stand.	89
Figure 6-3: Complete layout for the 2K heat exchanger test stand.	89
Figure 6-4: 2K Cold box for the heat exchanger test stand.	90
Figure 6-5: Various sensor attaching methodology outside the pipe (left), and view from inside pipe showing the thermowell technique (right).	92

Figure 6-6: The behavior of various attached sensors during refilling of LHe.	92
Figure 6-7: Comparison of different sensor attaching methodologies at low temperatures. 93	
Figure 6-8: Kyowa sensor in an Al block attached on the 10 K thermal shield.	95
Figure 6-9: Calibration curve for the Kyowa® PHS-B sensor from 7 to 300 K.	95
Figure 6-10: (a) Temperature data with respect to mass flow rate for the 2K HX_1, (b) Schematic view of the fluid flow through the heat exchanger test stand.	99
Figure 6-11: Experimental effectiveness and GHe ΔP of the 2K HX_1.	100
Figure 6-12: Thermal load from surroundings to the GHe flowing through 2K HX_1 shell.	101
Figure 6-13: Thermal load obtained from the flow meter with respect to heat load to He II.	102
Figure 6-14: Algorithm for determining 2K HX effectiveness.	103
Figure 6-15: CAD model for the 2K HX_1 performance analysis at various flow rates. ..	104
Figure 6-16: Temperature profile of the fluids flowing through the 2K HX_1 at various flow rates.	106
Figure 6-17: Comparison experimental and numerical results for the 2K HX_1 performance.	107
Figure 6-18: Colburn and friction factors for the GHe flowing through the 2K HX_1 geometry.	108
Figure 6-19: Velocity streamline for the GHe flowing through the 2K HX_1.	109
Figure 6-20: Turbulence kinetic energy for the GHe flowing through the 2K HX_1.	110
Figure 7-1: Algorithm for the parametric study of the 2K HX_1.	112
Figure 7-2: Bypass area for the 2K HX.	113
Figure 7-3: Helix angle for the CFD analysis of the 2K HX.	114
Figure 7-4: Helical pitch for the 2K HX.	115
Figure 7-5: Effectiveness for the 2K HX with variation in helix angle and bypass area. ..	116
Figure 7-6: GHe ΔP for the 2K HX with variation in helix angle and bypass area.	116
Figure 7-7: Colburn factor for the GHe at different helix angle with varied bypass area. ..	118
Figure 7-8: Friction factor for the GHe at different helix angle with varied bypass area. ..	118

Figure 7-9: friction to Colburn factor ratio for the GHe at different helix angle with varied bypass area.....	119
Figure 7-10: Colburn factor for the GHe with varied bypass area at a constant friction factor.....	120
Figure 7-11: Effect of the varied helical pitch on the effectiveness and GHe ΔP of the 2K HX.	121
Figure 7-12: Effectiveness and GHe ΔP for various helix angles with 4.7% bypass area and 8 mm helical pitch. This data is for 3 g/s flow rate and at a constant wall temperature of 3.6 K.	124
Figure 7-13: Colburn and friction factors and their ratio for the GHe at various helix angles with 4.7% bypass area and 8 mm helical pitch.....	124
Figure 7-14: Required axial length for the 2K HX to obtain 84% effectiveness with various helix angles at 3 g/s flow rate.	126
Figure 8-1: Algorithm for the optimization study for the superfluid helium cryogenic systems.	128
Figure 8-2: Pumping capacity determination using the data from the parametric study conducted for the 2K HX_1.....	129
Figure 8-3: Effectiveness and GHe ΔP of the 2K HXs with varied helix angles and at different flow rates with bypass area of 4.7% and helical pitch of 8 mm.	132
Figure 8-4: Cooling capacity and effectiveness of the 2K HXs with respect to the GHe ΔP at the limiting point with axial length restriction.	133
Figure 8-5: Cooling capacity of cryogenic systems for various helix angles at 84% effectiveness and 3 g/s flow rate without axial length restriction.	133
Figure 9-1: CAD model of the 2K HX_2 (above); the manufactured 2K HX_2 (below)..	136
Figure 9-2: 2K HX_2 temperature data compared with the 2K HX_1 at various flow rates.	137
Figure 9-3: 2K HX_2 effectiveness and GHe ΔP compared to the 2K HX_1.	138
Figure 9-4: Effectiveness and GHe ΔP for the experimentally tested 2K HX_2 and its numerical model.	140

LIST OF TABLES

Table 2-1: Geometric parameters of the 2K HX_1.	35
Table 4-1: Mesh independency test results	46
Table 4-2: Initial conditions for the OFC Domain	48
Table 4-3: Initial conditions for the GHe	48
Table 4-4: Boundary Conditions for fluid and solid boundaries in the domains.	49
Table 5-1: Experimental results for RRR measurement of the 2K HX_1 fins.....	76
Table 5-2: 2K HX domains and the initializing conditions.....	80
Table 5-3: Boundary conditions for the 2K HX in ANSYS CFX®.....	80
Table 6-1: Process parameters of the 2K HX_1.....	105
Table 6-2: 2K HX_1 domain and the initializing conditions.	105
Table 6-3: Boundary conditions for the 2K HX_1 in ANSYS CFX®.....	105
Table 6-4: Summarized performance parameters for the 2K HX_1.	106
Table 7-1: Effect of varied helical pitch on the effectiveness of 2K HXs.....	122
Table 7-2: Comparison of improved 2K HXs with axial length restriction with respect to the 2K HX_1.....	125
Table 7-3: Comparison of improved 2K HX without axial length restriction with respect to the 2K HX_1 in the cryogenic systems.	126
Table 8-1: Comparison of the cooling capacity for 2K HXs with axial length restriction.	134
Table 8-2: Comparison of the cooling capacity for 2K HXs without axial length restriction.	134
Table 9-1: Geometric parameters of the 2K HX_2 compared to the 2K HX_1.....	135
Table 9-2: Comparison of experimentally tested 2K HX_2 with respect to 2K HX_1.....	139

ABSTRACT

The superfluid helium cryogenic systems are widely employed for the operation of superconducting magnets and cavities below 2.0 K. At KEK, superconducting radio frequency (SRF) cavities are used for electron beam acceleration at the compact Energy Recovery Linac (cERL) and the Superconducting RF Test Facility (STF) for the International Linear Collider (ILC). The SRF cavities operate at temperatures of 2.0 K or below, due to their higher resonant frequency of 1.3 GHz. To obtain temperature < 2.0 K, SRF cavities are cooled with saturated superfluid helium (He II), which is another phase of liquid helium (LHe or He I) when its temperature is below 2.17 K, under saturation condition. The superfluid helium is produced continuously via a Joule-Thomson (JT) valve in the cryogenic system, which maintains the level of He II in the helium tanks of SRF cavities. Also, a 2K heat exchanger (2K HX) is introduced in series with the JT valve to recover the coldness from evaporating saturated 2.0 K gaseous helium (GHe). This increases the production rate of superfluid helium by reducing the incoming LHe temperature from 4.4 K to 2.2 K or above, before the JT valve. As such, the vapor flash loss (dryness) is also reduced from 40% to 9.4% during the JT expansion for production of 2.0 K saturated superfluid helium. The saturated vapor pressure (3.13 kPa) on the 2.0 K He II is maintained with the aid of rotary vane vacuum pumps in series with roots blowers, operating at room temperature and pressure. The capacity of these pumps to maintain 3.13 kPa vapor pressure is limited and will reduce with further lowering of inlet pressure. If the GHe pressure drop through the 2K HX is high, it can reduce the inlet pressure to the vacuum pumps, hence reducing the flow rate through the 2K HX to maintain the level of He II.

At KEK, we have a 2K heat exchanger (2K HX_1) consisting of helically coiled tubes and laminated fins made of oxygen-free copper (OFC), designed by Prof. K. Hosoyama. It was designed to handle mass flow rates of ~ 3.5 g/s in counterflow arrangement. The laminated fins on the helical tube are to increase the surface area for the 2.0 K GHe and the enthalpy extraction is thus improved from the LHe flowing through the helical tubes. Two 2K HX_1

Abstract

in series for each 2K refrigerator cold box are employed to obtain 84% effectiveness at the maximum operating flow rate for the cryogenic systems (~4 g/s). The focus of this research will be on determining the performance of the 2K HX_1 and the GHe pressure drop through it. Moreover, its design will be optimized to improve the He II production rate from the superfluid helium cryogenic systems. The performance of a heat exchanger is characterized by a factor known as “effectiveness”, which is the ratio of actual heat transfer to the maximum possible heat transfer between the fluids. The challenge in determining its effectiveness theoretically is the unknown heat transfer properties of GHe flowing through the unique design of this 2K heat exchanger, hence it needs to be determined experimentally using a heat exchanger test stand. Also, a numerical model based on computational fluid dynamics (CFD) and finite difference methods (FDM) is employed to validate the experimental results and to study the heat exchanger design.

The performance of the 2K HX_1 was determined experimentally with the heat exchanger test stand to be 75% with a GHe pressure drop of 136 Pa at 3 g/s of mass flow rate. The quality of He II (wetness) obtained at the exit of the JT valve was 86% (vapor flash loss – 14%). CFD simulations were performed with the aid of ANSYS CFX® to determine the heat transfer properties of GHe flowing through the 2K HX_1. The obtained results from the CFD simulations were fed to the numerical model to determine the effectiveness, using FDM performed with the aid of Mathematica®. The effectiveness from CFD simulations and FDM was determined to be 73.2% with a GHe pressure drop of 118 Pa at 3 g/s.

A CFD based parametric study was also conducted to optimize the 2K HX_1 design, with the goal of improving its performance and maximizing the He II production (or cooling capacity) for the cryogenic systems. The current setup of the two 2K HX_1 in series for each cold box, produces 70 W and 80 W of cooling capacity at 2.0 K for STF and cERL cryogenic systems, with 84% effectiveness. The optimized 2K HX (2K HX_3) design has 84% effectiveness with 430% lower GHe pressure drop compared to the two 2K HX_1 in series in the cryogenic facilities. Due to the lower GHe pressure drop of the 2K HX_3, the cooling capacity of STF and cERL cryogenic system can be improved by 15%. From the parametric

Abstract

study, 2K HX_2 was manufactured and tested experimentally to prove the reliability of the numerical model of the 2K HX. It provided higher effectiveness (by 4%) with lower GHe pressure drop (by 40 Pa) at 3 g/s flow rate, compared to the 2K HX_1, and the obtained experimental results were in agreement with its numerical model.

In conclusion, the performance of the 2K HX_1 was determined numerically and verified experimentally with the aid of heat exchanger test stand. A parametric study of the 2K HX_1 design was conducted and its design was optimized. The optimized design (2K HX_3) improves the cooling capacity of the capacity of the STF and cERL cryogenic systems. The parametric study was validated experimentally using the heat exchanger test stand at STF.

Chapter 1. INTRODUCTION

1.1. Particle Accelerators

Particle accelerators are devices that produce energetic beams of particles which are used for understanding the fundamental building blocks of nature and the forces that act upon them. They have other uses such as: understanding material structures and their properties, production of light source, X-rays, medical isotopes, neutrons etc [1]. A basic particle accelerator accelerates beams of positrons and electrons to near light speed. The collision between the beams of these two particles produces many sub atomic particles, which are studied by physicists all over the world. Some of the well-known types of particle accelerators are:

- **Linear Accelerators:** In this type of accelerator, a series of accelerating radio frequency cavities are used to accelerate particle beams to near light speed. The particle beam only passes once through the accelerating cavities [2]. Examples of some of the well-known large-scale linear accelerators are: LCLS-II in SLAC (USA), XFEL in DESY (Germany). The largest linear accelerator, the International linear collider (ILC) is in approval phase.



Figure 1-1: Linear accelerator at SLAC, Stanford, USA [42].

- **Circular Accelerators:** Particles travel in circular orbits and are accelerated to near light speed using one or a small number of radiofrequency accelerating cavities [2]. This approach is realized in circular accelerators such as, LHC at CERN (Europe) and SuperKEKB in KEK (Japan).

Introduction

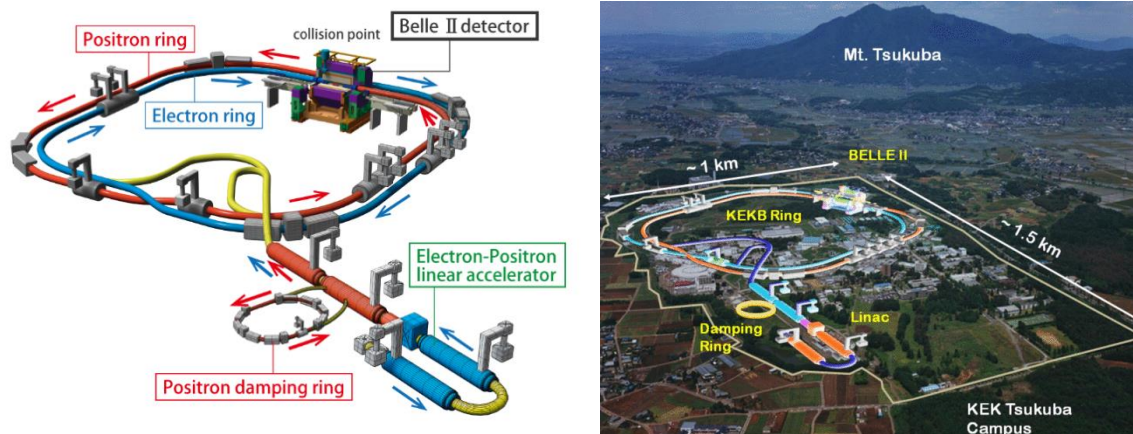


Figure 1-2: Circular accelerator at KEK, Japan [43].

1.1.1. Accelerators based on types of accelerating cavities

A radiofrequency (RF) cavity is a metallic chamber that contains an electromagnetic field. Its primary purpose is to accelerate charged particles. RF cavities can be structured like beads on a string, where the beads are the cavities and the string is the beam pipe of a particle accelerator, through which particles travel in a vacuum. Very high accelerating voltages can be obtained with RF cavities far exceeding those of electrostatic accelerators. Basically, the RF accelerating cavities can be divided in two types: a normal conducting and a superconducting cavity:

Normal Conducting RF Cavity

Normal conducting cavities make use of high RRR copper as the material for cavity and it can be operated at room temperature. The disadvantage of these cavities is the very low Q_0 value in the range of 10^4 , due to the copper's high resistivity compared to superconducting material. For a similar accelerating gradient, the power loss in copper cavities is of several magnitudes higher due to its higher surface resistivity, compared to a superconducting cavity. For an accelerating gradient of 1 MV/m in a 10 cm long and 7.65 cm radius normal conducting cavity, the power loss is 0.2 MW compared to just 0.4 W in superconducting cavities for 1.5 GHz resonant frequency [3].

Introduction

Superconducting RF Cavity:

Major superconducting cavities are made of pure niobium and are operated at liquid helium temperatures. The superconducting transition temperature of niobium is < 9.2 K and most of the niobium based accelerating cavities are operated at liquid helium temperatures (< 4.21 K), usually cooled with liquid helium baths. The low electrical resistivity of a superconducting material allows an RF resonator to obtain an extremely high quality factor (Q_0).

For example, it is commonplace for a 1.3 GHz niobium SRF resonant cavity, as seen in Figure 1-3, at 1.8 K to obtain a quality factor of $Q_0=5 \times 10^{10}$. Such a very high Q_0 resonator stores energy with very low loss and narrow bandwidth. The motivation for using superconductors in RF cavities is not to achieve a net power saving, but rather to increase the "quality" of the beam attunement. The cavities have to be operated in a superfluid helium bath at a temperature of 1.6-1.8 K to achieve an optimized relation between quality factor and the cryogenic efficiency. The cost of a refrigeration plant also plays a large role in determining the operating temperature of the cavity.



Figure 1-3: A 9-Cell 1.3 GHz superconducting cavity.

Many of the accelerator facilities around the world employ superconducting technologies for various applications, the largest being Large Hadron Collider at CERN in Europe. The said collider is a two-ring superconducting hadron accelerator, and is installed in a 26.7 km tunnel. It makes use of superconducting magnets and cavities to circulate proton-proton beams in a counter-rotating motion. The LHC machine accelerates the proton-proton beam

Introduction

to 14 TeV energy [4]. At KEK, SuperKEKB is a 3 km in circumference circular collider, which uses superconducting cavities to accelerate particles to near light speed. At XFEL in DESY, a 3.4 km superconducting linear accelerator, which is also the longest in the world, makes use of superconducting cavities to produce electron beams for researchers to study X-ray flashes. The electron beams through the superconducting RF cavities are energized to 17 GeV at this accelerator facility [5].

1.2. Helium as a Coolant for Superconducting Accelerators

1.2.1. Introduction

Helium is a noble gas and the second lightest element in the world. Its boiling point is the lowest among the known elements, at around $-269\text{ }^{\circ}\text{C}$ or 4.21 K under atmospheric pressure. It was liquefied for the first time by Kammerlingh Onnes in Leiden, 1908. In 1938, it was independently discovered by Allen, Misener and Kapitza that liquid helium below lambda point showed frictionless flow, which is now known as “Superfluid”. Fritz London was the one who suggested the connection between superfluidity, Bose-Einstein condensate and superconductivity [6]. In 1941, Landau suggested that superfluidity can be understood in terms of phonons and rotons, and realized to the idea of “two-fluid model”. In 1957 Bardeen, Cooper and Schrieffer presented the theory of superconductivity leading to better understanding of the connection between superconductivity and superfluidity.

1.2.2. Phase diagram and its specific heat capacity

In Figure 1-4, several unique features of helium can be seen in addition to conventional characteristics such as the critical point and the two-phase co-existence and solid. Another phase of helium can be observed, called as superfluid helium or He II, seeing as helium has the unique property of having two liquid phases.

Introduction

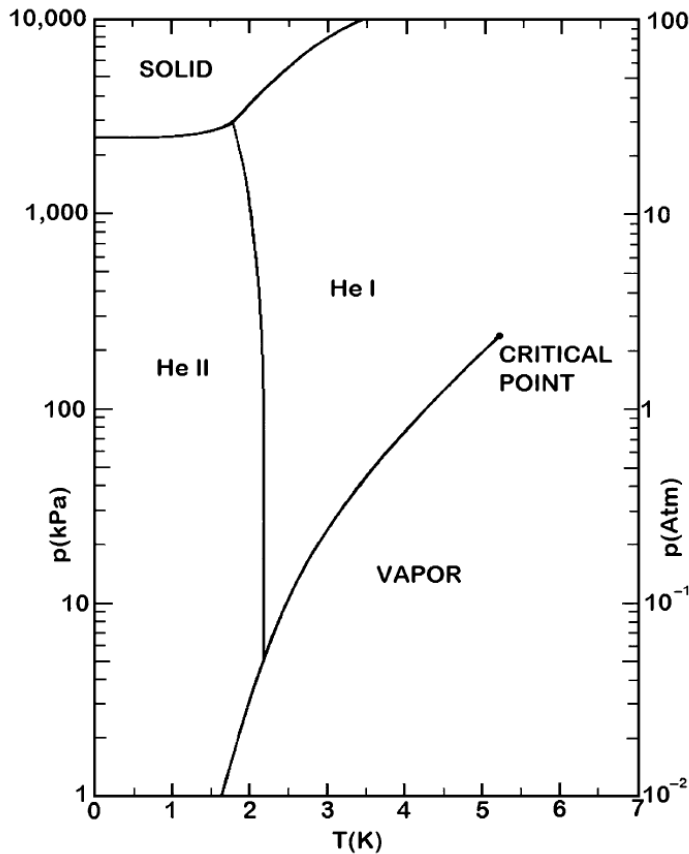


Figure 1-4: Phase diagram for helium.

Normal liquid helium or He I shows similar characteristics to classical fluids. It acts like a weakly interacting gas due to its weak intermolecular interaction and low viscosity [5]. Superfluid Helium or He II has specific physical properties unique to it, such as its non-existent viscosity and its high apparent thermal conductivity, even higher than the high conductivity solids such as copper [5]. There is a discontinuity that exists in the specific heat capacity in He I transition to He II, which is at around 2.176 K temperature at its saturation pressure. The discontinuity in specific heat is called as a lambda (λ) point, the name since the discontinuity looking like the Greek letter lambda. The lambda transition is a second order phase transition and it has no latent heat of formation for the He II state. He II fluid can be treated as quantum fluid, and its behavior is partly explained by BCS theory and London's two-fluid model.

Introduction

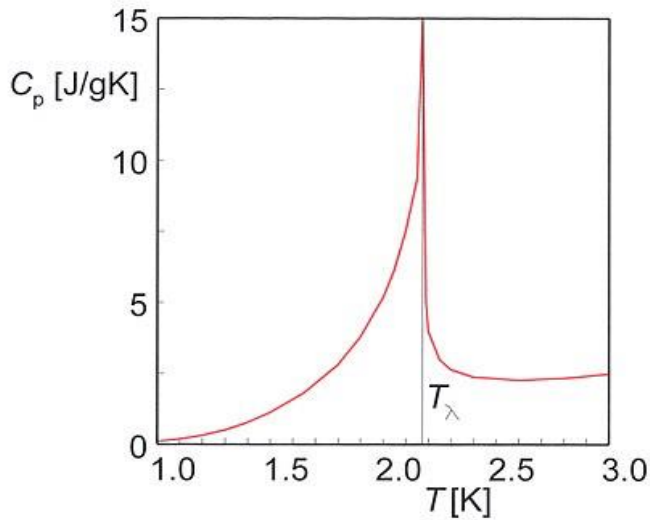


Figure 1-5: Specific heat capacity of liquid helium as a function of temperature (T_λ : Lambda point).

1.2.3. Why superfluid helium for superconducting magnets and cavities?

The high heat transport capability of superfluid helium makes it a prime candidate for cooling SRF cavities, due to the stability of its bath during evaporation and its apparent thermal conductivity at solid/liquid interface which is better than any known solids. The requirement of such low temperature cooling arises due to the dependence of the BCS losses on the ratio of the operating temperature to its critical temperature. The lack of viscosity of the superfluid helium makes it easier to permeate through superconducting magnet windings and to cool them efficiently through its apparent high thermal conductivity (approximately 100 times the oxygen free copper).

Two-fluid model

The two-fluid model predicts He II to be comprised of two fluid components: normal fluid and the superfluid. The normal component behaves as an ordinary liquid and its properties are denoted with subscript 'n', and density can be denoted as ρ_n . The superfluid term is denoted with subscript 's', but it has no viscosity and the entropy is 0. The density of the superfluid helium is the sum of both densities [6]:

$$\rho = \rho_s + \rho_n. \quad (1.1)$$

Introduction

The superfluid has no entropy, so the He II entropy can be written in terms of normal fluid alone:

$$\rho s = \rho_n s_n. \quad (1.2)$$

Here, s , is the specific entropy. Between the temperature of Lambda point (2.176 K) and 1.1 K the entropy is heavily temperature dependent, approximately $T^{5.6}$.

For viscosity, the model assumes $\mu_s = 0$ with dissipative interaction being only due to normal fluid. These assumptions correspond to the fact that the superfluid experiences no resistance to component flow and therefore no turbulence, but this assumption is only partially true because above certain critical velocity the superfluid does transitions to the so called “turbulent state”.

Equation of motion

For a special case where He II is cooling a sample via bath cooling, the net mass flow between the normal component and the superfluid component becomes zero, hence the momentum density becomes zero [6],

$$\begin{aligned} j &= \rho_n v_n + \rho_s v_s, \\ \text{if } j &= 0, \quad \rho_s v_s = -\rho_n v_n, \end{aligned} \quad (1.3)$$

where, v , is the velocity and the above expression leads to internal convection or counterflow. With internal convection the fluids can carry entropy without experiencing mass flow. The continuity equations describe the rate of change of density in a given volume of space for each component of the He II. For an ideal fluid with no shear stress and negligible viscosity, the only force that acts on it is due to pressure gradient (∇p) [6]:

$$\frac{\partial v}{\partial t} + v \cdot \Delta v = -\frac{1}{\rho} \nabla p. \quad (1.4)$$

To develop the behavior of entropy flow in He II, Euler’s equation is applied. In Euler’s equation, the fluid does not experience dissipative interaction and all processes are reversible.

Introduction

The expression analogous to the continuity equation of mass conservation is obtained from the Euler's equation [6]:

$$\frac{\partial}{\partial t}(\rho s) = -\nabla \cdot (\rho s \mathbf{v}_n). \quad (1.5)$$

To develop the equation of motion for He II, at first the superfluid component is considered, and a system where a volume is connected to other volume with a special valve which only allows superfluid component to pass through. The Gibbs energy equation is considered to describe the change in internal energy of the system, associated with the change in mass. The equation of motion for the superfluid component is,

$$\frac{\partial \mathbf{v}_s}{\partial t} = s \nabla T - \frac{1}{\rho} \nabla p. \quad (1.6)$$

Heat Transport in He II

Let's assume that He II obeys the two fluid model, then London's equation establishes the relationship between temperature difference and pressure difference [6],

$$\Delta p = \rho s \Delta T. \quad (1.7)$$

The two fluid equations are combined to solve the heat flow problem in a steady state condition, which is also called as the Poiseuille equation.

$$\nabla p = \mu_n \nabla^2 \mathbf{v}_n. \quad (1.8)$$

For 1-dimensional channel with constant diameter, d , the Equation 1.8 can be simplified:

$$\frac{dp}{dx} = \rho s T v_n = -\frac{\beta \mu_n v_n}{d^2}. \quad (1.9)$$

where β is the numerical constant determined by geometrical conditions.

Introduction

The He II can only transport heat by its normal fluid component. For the case where it is a closed system the net mass flow rate is zero, $v = 0$, and the heat flux density is directly proportional to v_n [6]:

$$q = \rho s T v_n. \quad (1.9)$$

The heat conductivity equation obtained from eliminating v_n from the Poiseuille equation describes the behavior of ideal He II [6]:

$$q = - \frac{d^2(\rho s)^2 T}{\beta \mu_n} \frac{dT}{dx}. \quad (1.10)$$

The expression given in Equation 1.10 is a form similar to pure conduction, which is like an effective thermal conductivity, k_{eff} , varying as the square of the diameter. For He II at 1.9 K in a circular tube with diameter of 10 μm , the effective thermal conductivity of He II is 49 kW/mK. The effective thermal conductivity from this expression is dominated by the dependence of $(\rho s)^2 T \approx T^{0.5}$. So, even if the thermal conductivity of He II at 1.9 K is 100 times higher than OFC copper, it is only 25 W/mK at 1 K [3].

1.3. Basics of He II Production

1.3.1. Normal liquid helium liquefaction

To produce superfluid helium, first it is necessary to produce liquid helium. Production of liquid helium is achieved by liquefiers/refrigerators which operate basically on the principle of Claude or Collins cycle [7]. At first, helium gas is compressed isothermally to 16-17 bar pressure and then either precooled by liquid nitrogen or part of the high-pressure gas is expanded through expanders to precool the other high-pressure gas. This precooled high-pressure gas is allowed to rejoin the returning line to cool the high-pressure gas below 45 K (inversion temperature of helium gas) getting to as low as approximately 5.1 K. The cooled high-pressure gas is expanded through a Joule-Thomson valve for liquefaction. The liquefied

Introduction

helium is stored in a helium storage Dewar and the cold gas is returned back in the cycle through heat exchangers to act as a precooler for the hot high-pressure incoming gas. In the Figure 1-6, a 6.8 kW helium liquefier's cycle is shown. It consists of helium compressors, heat exchangers, turbines, a JT valve and a 12,000 L Dewar to store the liquid helium.

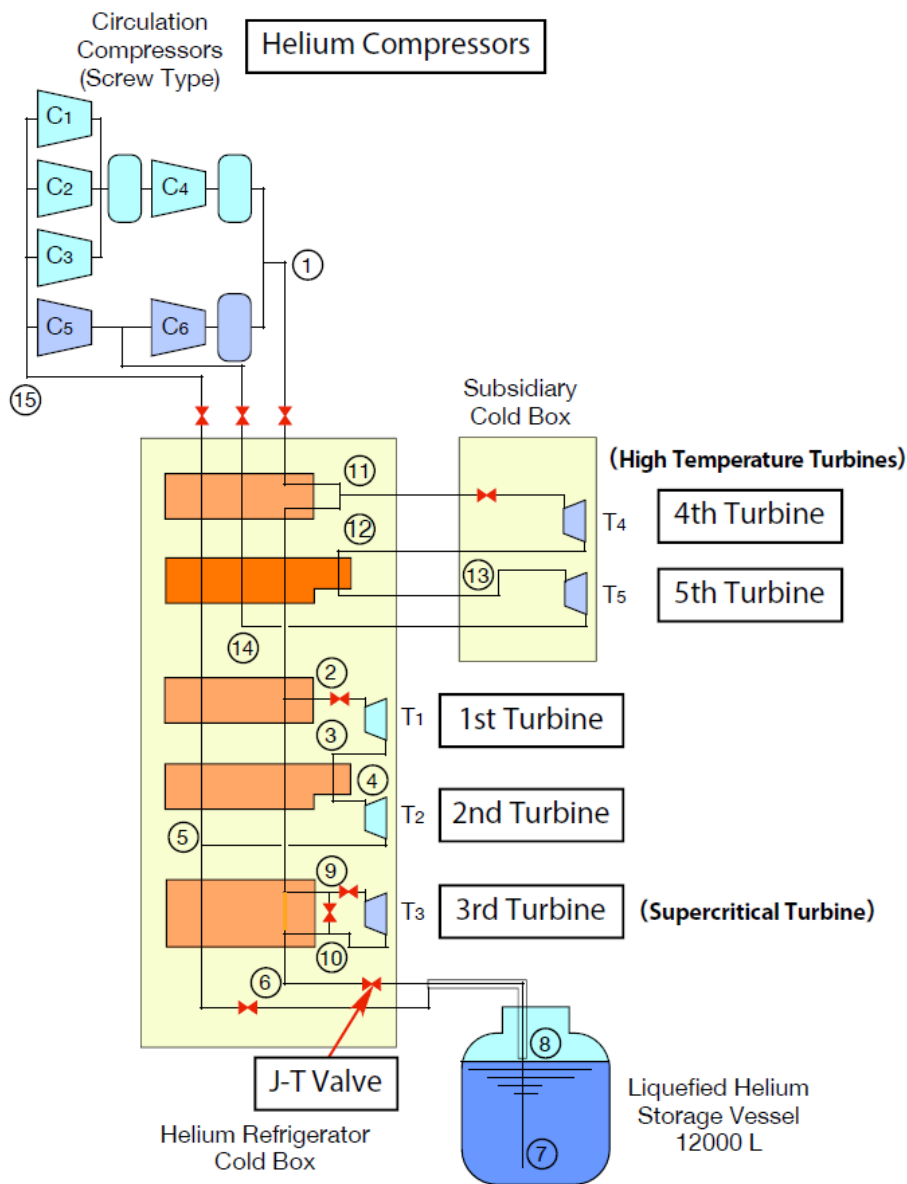


Figure 1-6: Basic layout of the helium liquefier for the SuperKEKB accelerator.

Introduction

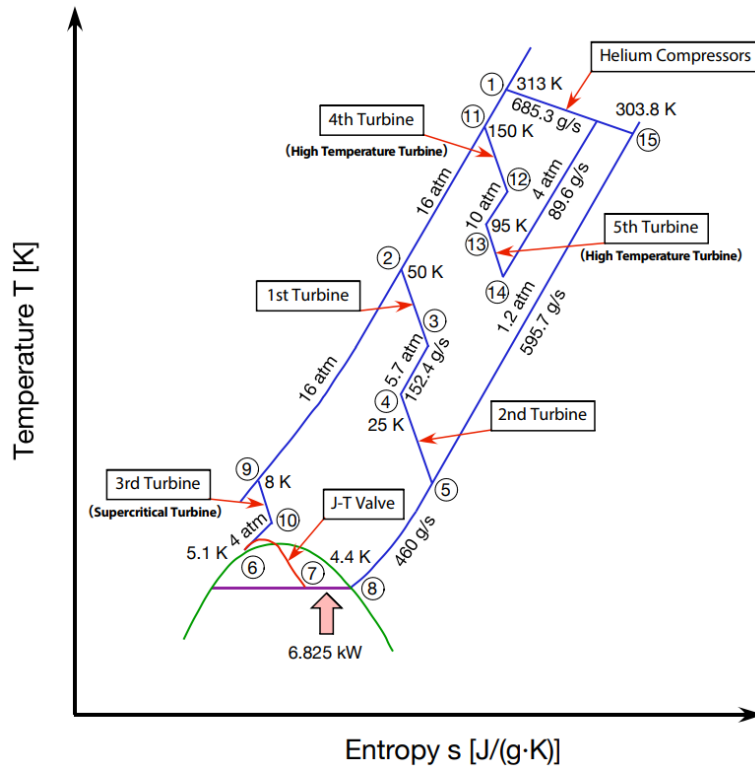


Figure 1-7: T-S diagram of the SuperKEKB helium cryogenic system.

1.3.2. He II liquefaction

Unlike normal liquid helium liquefiers, the He II liquefiers are not mass produced. Most of the He II production is incorporated in the normal liquid helium cycle to make it a closed cycle process [6]. Once the liquid helium is stored in a Dewar at atmospheric pressure (4.21 K), there are two ways to produce superfluid helium (< 2.17 K):

1. Pumping on the liquid helium to reduce its vapor pressure from 125 kPa (atmospheric pressure) to < 5.03 kPa, which is the saturation pressure at lambda point. As the vapor pressure keeps on reducing, the temperature of liquid helium keeps on dropping. To produce 2.0 K He II, the required vapor pressure is 3.13 kPa. The disadvantage is that during this procedure approximately 40% of liquid helium is boiled off, hence around 60% of the He II is produced for cooling superconducting cavities. Usually a JT valve separates the high-pressure line from 4.4 K liquid helium to 2.0 K He II.

Introduction

2. The better way, which is employed in all large-scale superfluid helium cryogenic systems, is to recover the specific heat of evaporating cold 2.0 K gaseous helium to subcool 4.4 K or 4.21 K liquid helium via a *2K heat exchanger* to approximately 2.2 K or above. The subcooled liquid helium is then expanded isenthalpically through a JT valve, from 125 kPa to 3.13 kPa to produce 2.0 K He II continuously. This way it is possible to reduce vapor flash losses from 40% to 9.4%, as shown in Figures 1-8 and 1-9. The reasoning for limiting the outlet temperature from 2K heat exchanger to ~ 2.2 K is described below:
- At 2.2 K, the specific heat capacity of the LHe is almost equal to the GHe and at near the lambda point it is almost 2 times that of the GHe, hence to reach temperatures below 2.2 K the size of the 2K HX needs to be larger.
 - Below the lambda point, the phase transition from He I to He II occurs and the high He II thermal conductivity tends to reduce the heat transfer coefficient considerably, since heat is transported through He II rather than to the wall.
 - Another factor that reduces heat transport capabilities for He II is the Kapitza resistance for He II-Cu boundary, which cannot be ignored below the lambda point.

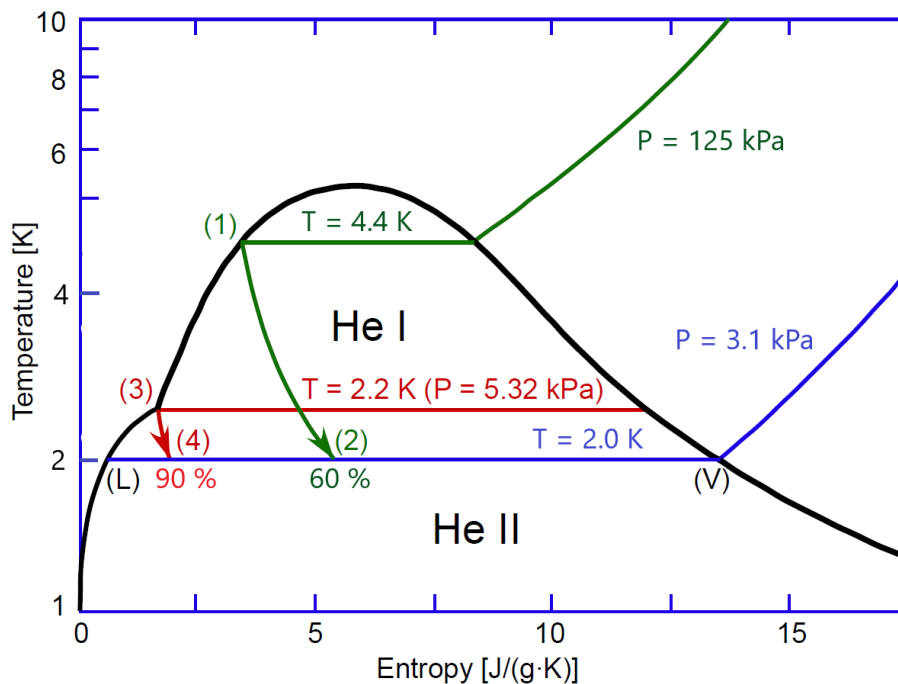


Figure 1-8: T-S diagram for the He II production with and without subcooling.

Introduction

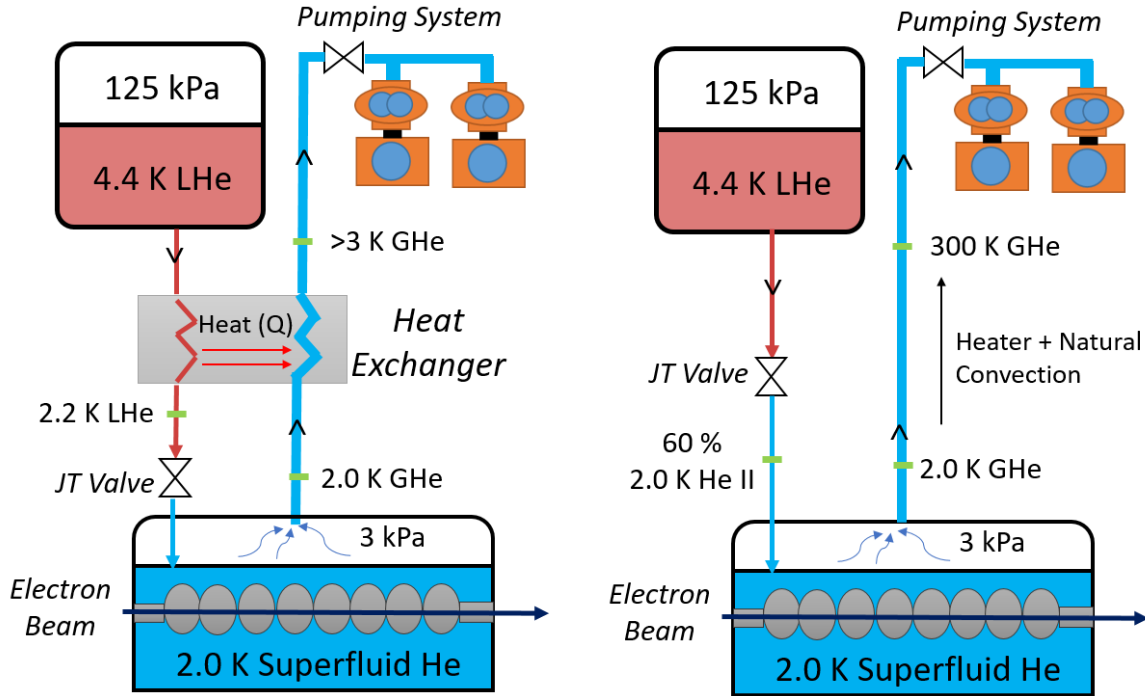


Figure 1-9: Basic layout for the He II production system with and without heat exchanger.

1.3.3. Pumping system for He II

The pumping systems that are employed to maintain sub atmospheric low vapor pressure on the 2.0 K He II bath are described in Reference [8] and is shown in Figure 1-10:

- **Warm compression:** In this system, < 5 kPa vapor pressure is maintained on the superfluid helium with the aid of a series of rotary vane vacuum pumps. These pumps operate at room temperature, and are usually employed for flow rates < 4.5 g/s or 100 W. Before supplying them to compressors, the helium gas is heated to room temperature with the help of kW range heaters. The disadvantage of this methodology is the exergy loss in the heater before the helium gas is compressed [9].
- **Cold compression:** It makes use of a series of cold compressors operating at inlet temperatures of 2.0 K or below, right after the evaporation of He II. This kind of compression usually require 4-5 cold turbo-compressors in series to compress the sub

Introduction

atmospheric 2.0 K gaseous helium to atmospheric pressure, hence increasing its temperature to 20-30 K in the process. This way the cold helium at atmospheric pressures can be returned back to liquefiers to recover the sensible heat of returning cold helium [9]. This kind of cycle is usually employed for flow rates > 4.5 g/s. This kind of cycle is in commission at SLAC for the LCLS-II cryogenic system [10].

- **Mixed Compression cycle:** It is based on a combination of cold compressors working at low temperatures in series with warm compressors at room temperature. This kind of cycle is employed at CERN for the Large Hadron Collider's cryogenic system [8].

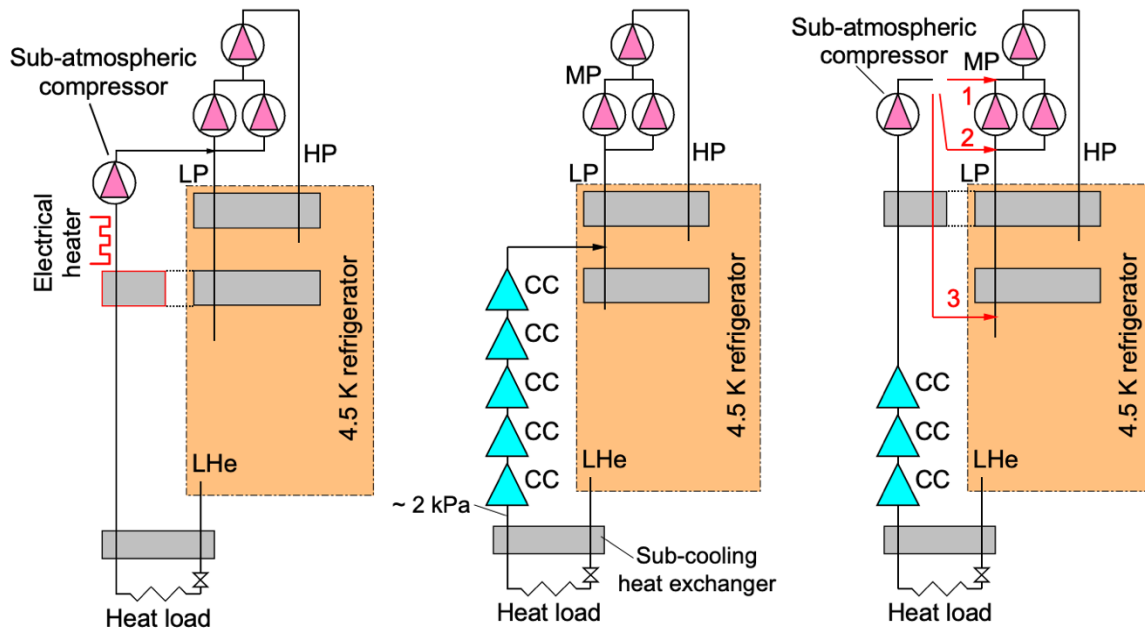


Figure 1-10: Various types of the He II liquefaction cycles [8].

1.4. Background on 2K Heat Exchanger Research

A heat exchanger is simply a device that transfers heat from hot fluid to cold fluid. The fluids are separated through a solid wall and the enthalpy transfer happens through the temperature difference between the fluid elements through the wall. Basically, heat exchangers are divided into three categories according to direction of fluid flow: parallel flow, counter flow and cross flow heat exchanger. Each of the flow arrangements have their own advantages, disadvantages, and respective applications in industries. Some of the commonly used heat exchangers are shell and tube, plate heat exchanger and plate and fin heat exchangers [11]. The main requirements of the 2K heat exchanger in a superfluid helium cryogenic system are:

1. To reduce the He I temperature to 2.2 K or above using the sensible heat carrying capacity of the outgoing helium gas at < 2.1 K.
2. To keep the GHe pressure drop through its geometry to a fraction of the absolute saturation vapor pressure of the superfluid helium bath. Usually the 2K heat exchangers are designed to have a GHe pressure drop of < 100 Pa for maximum allowable flow rate.

For large scale cryogenic systems, these heat exchangers were employed at CERN for the LHC's cryogenic systems for very first time. The superconducting magnets of the LHC are cooled to 1.9 K by distributed cooling loops working with saturated two-phase helium. The needed operating conditions for the heat exchanger were a maximum flow rate of 5 g/s and a GHe pressure drop limit of 100 Pa. In order to produce temperatures below 2.2 K using 1.8 K GHe, the counter-flow heat exchangers designed by three manufacturers DATE, Romabau and SNLS delivered prototypes of different technologies for extensive cryogenic testing at CEA Grenoble [12], the 2K heat exchangers are shown in Figure 1-11. The heat exchanger designed by DATE was a stack of 50 stainless steel plate heat exchanger, oriented parallel to flow direction. The heat exchanger designed by SNLS was a stack of high thermal conductivity perforated copper plate. The heat exchanger type developed and manufactured by Romabau is composed of a bank of twenty tubes, wounded in 9 parallel coils with varying diameters. The performance of all the heat exchanger was measured at a test bench. The

Introduction

stacked plate type heat exchangers had a good thermal load range until 5g/s flow rate and the coiled multiple tube type by Romabau had a good GHe pressure drop range for higher flow rates, up to 5g/s [12].

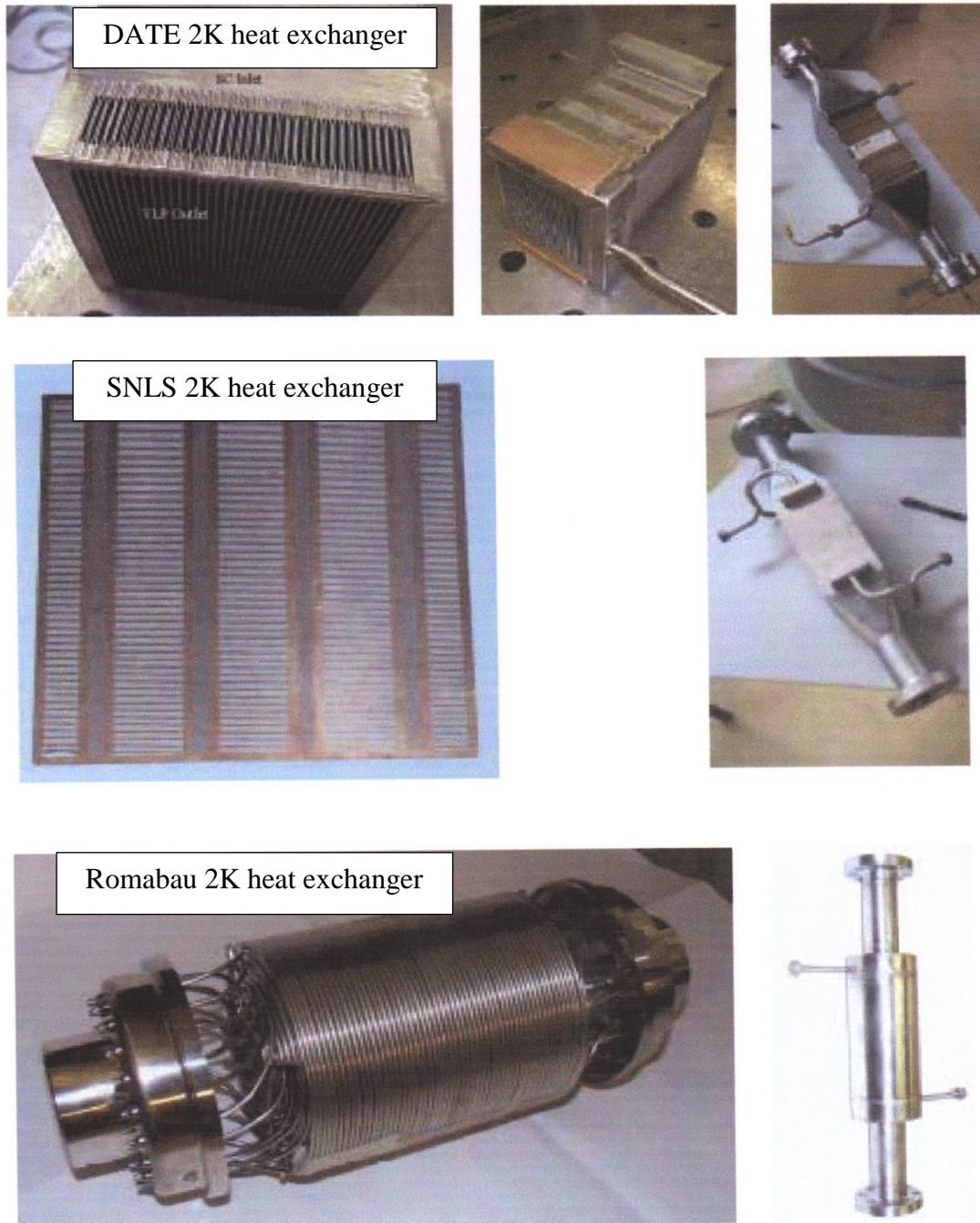


Figure 1-11: Different types of the 2K heat exchangers tested for CERN cryogenic system.

Introduction

KEK has two test facilities that employ SRF cavities: cERL(Compact Energy Recovery Linac) and STF (Superconducting RF Test Facility). Initially the testing capacity of the superfluid helium cryogenic system was 30 W at 2 K to test 8 SRF cavities [13]. The superfluid helium cryogenic system at KEK employs laminated finned type 2K heat exchangers. The efficiency of these types of 2K heat exchangers is unknown due to their unconventional design. Also, no temperature sensors were attached around the heat exchanger in the cold box, hence there is no experimental data to quantify its performance.

The FermiLab's vertical test stand has a coiled finned tube 2K heat exchanger currently in operation to test superconducting RF cavities. Numerical analysis was done on the coiled finned tube heat exchanger by using Engineering Equation Solver, the results having been verified with experimental results [14]. In the case of ILC, the thermal capacity required for 2K heat exchanger will be very large, approximately 3.67 kW [15]. At DESY, a recuperative heat exchanger primarily designed by FermiLab for mass flow rates of 10 g/s and vapor pressure of 16 mbar is adopted, as shown in Figure 1-12. The heat exchanger consists of two parallel coils made of externally finned tubes. The supplied helium is divided into two streams to flow in the copper tubes and is cooled with low pressure gaseous helium flowing through the heat exchanger geometry [16].



Figure 1-12: Coil-Finned 2K heat exchanger for vertical test cryostat at XFEL, DESY [16].

Introduction

All the designed 2K heat exchangers mentioned above are specifically for a certain flow rates and the maximum GHe allowable pressure drop at that flow rate. Therefore, there is no unified design for the 2K heat exchanger and each has its advantages and disadvantages.

1.5. Motivation

The need of a 2K heat exchanger arises due to the requirement for reduction of flashed liquid helium volume and the excess heat load from the 4.4 K liquid helium for the SRF cavities or magnet systems. To achieve superconductivity for RF cavities, low temperature cryogenics like liquid helium and superfluid helium are used to attain temperatures in the range of 1.8 K to 4.5 K. Nowadays superfluid helium is preferred over normal liquid helium because as the temperature of Nb cavity is lowered from 4.2 K to 1.8 K, superconducting cavity loss reduces a lot and hence the required cooling power reduces. The temperature range of 1.6 – 1.8 K is considered as an ideal cavity operating range since going below this temperature will reduce the cavity loss but in comparison to the power requirement for the refrigerator, it is not efficient. It can be said that 1.8 - 2.0 K is an optimum range for operating a superconducting cavity, as shown in Figure 1-13.

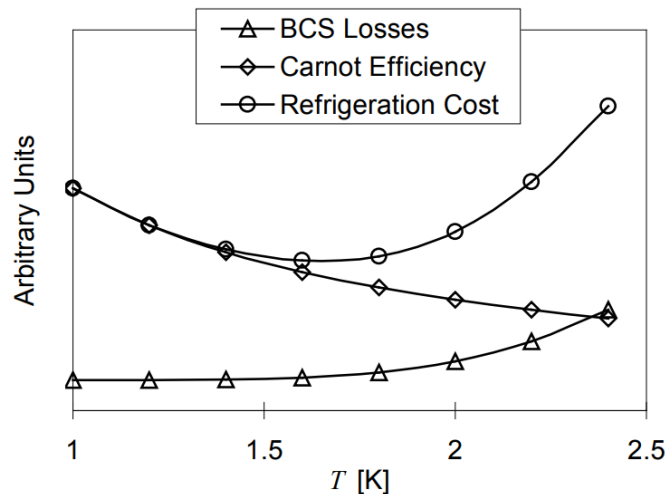


Figure 1-13: Optimal operating temperature for a superconducting cavity [8].

Introduction

The research on 2K heat exchangers is limited and there is a lack of understanding on their behavior at variable heat loads from the cryomodules housing the superconducting RF cavities. The main objective is to determine the effectiveness of the 2K heat exchanger at KEK (2K HX_1) and to optimize its design according to the required specification. The heat exchanger at KEK is a unique design, so to understand its behavior experimental and numerical studies have to be conducted. Moreover, it is necessary to study the effect 2K heat exchangers have on the gaseous helium pumping systems, as the pumping system dictates the amount of superfluid helium that can be produced while maintaining constant pressure on its bath. The main source of GHe pressure drop is due to the 2K heat exchangers, and the high pressure drop can compel the pumping system to operate at lower pressures, hence lowering the cooling capacity at 2.0 K for He II.

1.6. Composition of the Thesis

In this chapter, the background on the superconducting cavity-based particle accelerators were described. Afterwards, some basics on how to achieve superconductivity by using liquid helium as a cryogen were detailed. Moreover, various techniques on producing liquid helium and its other phase of superfluid helium were described. The background on the various types of 2K heat exchangers employed in the research facilities worldwide are also summarized. In Chapter 2, the superfluid helium cryogenic systems that are employed for the superconducting accelerator testing facilities at KEK are detailed. Then, the 2K heat exchangers that are employed in the testing facilities will be described. In Chapter 3, the objective of the study and the techniques employed to carry out the research work will be detailed. In Chapter 4, the computational fluid dynamics (CFD) based numerical methodology will be explained. For the research work, CFD simulations were employed to simulate the flow of fluids through the 2K heat exchanger. In Chapter 5, the details on the theory used to obtain the heat transfer properties of the fluids flowing through 2K heat exchangers were explained. The focus would be on the effectiveness analysis, heat transfer coefficients of the fluids and their pressure drop through the 2K heat exchanger geometry. In

Introduction

Chapter 6, the experimental setup manufactured to determine the 2K heat exchanger effectiveness will be shown. Moreover, the experimental methodology is described and the performance of the 2K heat exchanger is shown. The obtained experimental results are compared with the results obtained from the numerical model of the 2K heat exchanger. In Chapter 7, a parametric study would be conducted on the 2K heat exchanger design to improve its performance. In Chapter 8, the improved 2K HXs will be studied in conjunction with the GHe pumping systems to maximize the He II production rate from the cryogenic systems at KEK, for the operation of superconducting cavities. In Chapter 9, the optimization study is validated by manufacturing an optimized 2K HX and verifying it experimentally and numerically. In Chapter 10, concluding remarks will be summarized.

Chapter 2. SUPERFLUID HELIUM CRYOGENIC SYSTEMS AT KEK

2.1. Introduction

The superfluid helium cryogenic systems are widely employed for the operation of cryomodules, housing 1.3 GHz niobium superconducting radio frequency cavities (SRF) at 2.0 K. These cavities are used for electron beam acceleration at the Compact Energy Recovery Linac (cERL) and the Superconducting RF Test Facility (STF) for the International Linear Collider (ILC) at KEK. The superfluid helium cryogenic system consists of a helium liquefier, a 2K cold box, transfer lines and a gaseous helium pumping system, as shown schematically in Figure 2-1. The liquid helium (LHe) is liquefied with helium liquefiers and then stored in the 3000 litres Dewar [3]. The LHe is then supplied to the 2K cold box and then to the helium vessels of the SRF cavities. The pumping system then depressurizes the LHe in the helium vessels to transform the LHe to superfluid helium. A 2K heat exchanger (2K HX) in series with a Joule-Thomson (JT) valve is an essential part of the superfluid helium cryogenics system to subcool the LHe. As it recovers the coldness from the outgoing 2.0 K gaseous helium (GHe) at 3.13 kPa, it evaporates from the helium tanks of the SRF cavities. This reduces the LHe temperature from 4.4 K to ~2.2 K or above, before the JT valve, using the sensible heat of the cold GHe at 2.0 K. Lower inlet temperature results in vapor flash loss reduction from 40% to ~10% during the JT expansion, and hence a higher production rate of superfluid helium (He II).

The helium pumping system employs oil sealed rotary vane pumps and mechanical booster pumps. The vapor pressure on the 2.0 K superfluid helium is maintained with a control valve placed at the inlet of the pumping system and a pressure sensor, measuring the pressure on the superfluid helium in the He II tank of the 2K cold box. The refrigeration capacity of the superfluid helium cryogenic system is determined by the pumping capacity of the vacuum pumps. The evacuated gas helium by the pumping system is sent directly to the recovery compressor, purified with a helium purifier, and then liquefied again with the

Superfluid Helium Cryogenic Systems at KEK

helium liquefier/refrigerator in the initial operation of the cryogenic system. During the stable operation, the evacuated helium gas is returned directly to the main helium compressors. The returning helium gas from the He I tank and the 5K thermal shield is sent back to the liquefier to recover its enthalpy and hence improving the efficiency of the liquefier. The thermal load to the superfluid helium comes from two sources: static and dynamic heat loads. The static heat load comes from the heat of the surrounding room temperature (300 K). The sources for the static heat load are cryogenic components, such as cryogenic transferlines, cryomodules, 2 K cold box etc. The dynamic heat load comes from the heat being generated by the SRF cavities. The amount of heat generated depends on the quality factor (Q_0) of the cavities, acceleration voltages and can be estimated once these factors are known.

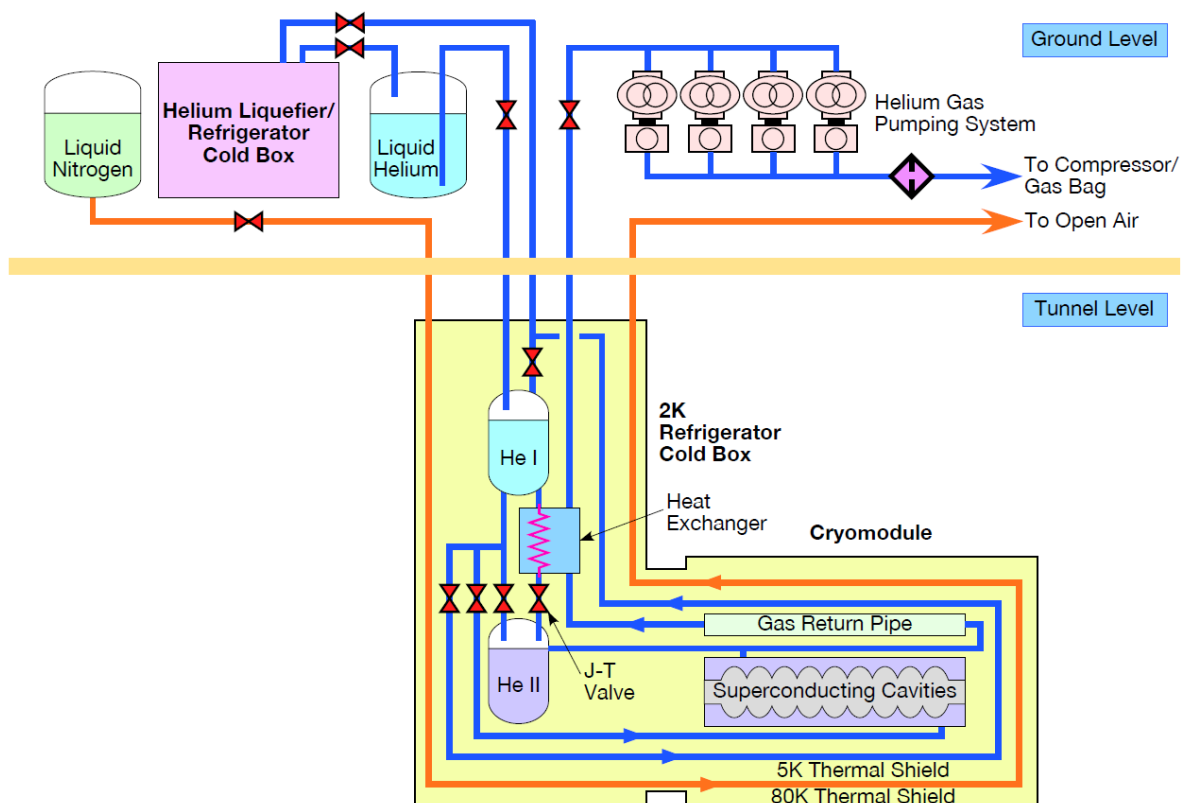


Figure 2-1: A schematic illustration of the superfluid helium cryogenic system at KEK.

2.1.1. Superconducting RF test facility

The main purpose of STF (Superconducting RF Test Facility) at KEK, is to develop the cryomodule, as well as the high performance cavities and to establish the industrial design of a main-linac unit for ILC (International Linear Collider). One of the important tasks is to carry out high power tests of the STF cryomodule, which includes four TESLA-type STF-Baseline 9-cell cavities and Low Loss-type High-Gradient 9-cell cavities. Not only the $Q_0 - E_{acc}$ curve and x-ray radiation level, but also the E_{acc} max in each cell is determined by passband mode measurements. The superconducting cavity system usually tested has a niobium cavity with thick titanium endplates, an input power coupler with cold and warm RF windows, two types of higher order modes (HOM) couplers, a mechanical tuner with a stepping motor and a piezo element, a titanium He tank and a magnetic shield inserted in the He tank.

At STF, the SRF cavities and their cryomodules are researched and developed for ILC. The 9 – cell SRF cavities employed for the ILC will be operated at 1.3 GHz. The SRF cavities have to be cooled down to temperatures of 2.0 K, to extract the heat generated by cavities at this frequency. The flow diagram of the superfluid helium cryogenic system for STF is drawn schematically in Figure 2-1. The helium liquefier/refrigerator employed for the cryogenic system is Sulzer (Linde) TCF 200. The refrigeration capacity for the TCF 200 is 600 W at 4.4 K and it can produce LHe at the rate of 250 L/h, in liquefier mode (approximately 180 W). The helium liquefier/refrigerator, the 2000 L liquefied helium storage vessel and the helium pumping system are installed on the ground level of the STF building [13]. The 2 K refrigerators and the SRF cavity cryomodules are installed on the underground tunnel level. The compressors can circulate helium at the rate of 2860 m³/hr. The superfluid helium cryogenic system for STF has two 2K refrigerators and each refrigerator has two heat exchangers in series. Initially these 2K heat exchangers were designed to produce about 40 W refrigeration capacity at 2 K. The two tanks in the 2K cold box can hold 65 L of He I and He II, respectively. Liquid helium is supplied to the 5K thermal shield to cool it down to approximately 10 K and to maintain that temperature. Also, LHe from the He I tank is

Superfluid Helium Cryogenic Systems at KEK

supplied to the He II tank via the JT valve and the 2K heat exchanger, to produce 2.0 K superfluid helium. A two-phase supply line connects the He II tank to the helium tanks of the SRF cavities in the cryomodule at the same level. The level of the superfluid helium in the He II tank is controlled by the JT valve, hence consequently in the two-phase pipe in the 2K cold box. The GHe pumping system has 8 rotary vane vacuum pumps and each pump has its own mechanical booster pump to increase the pumping capacity of the pumps. The pumping system produces 70 W of cooling capacity at 2.0 K for the STF system. A multi-channel transfer line connects the piping coming from 2K refrigerator cold box to the components that exist on the ground level. The capture cavity cryomodule contains two 9-cell cavities and is connected to one of the two 2K refrigerator cold boxes. The cryomodule has two stages of thermal shielding, one at 80 K cooled with liquid nitrogen and the other one at 5 K cooled with LHe. The total static heat loss at 2.0 K is about 9.5 W, the majority of the static load being 7 W, from the cryomodule itself. The dynamic loss from each of SRF cavities was 1 W and would vary with change in accelerating gradient. The cryomodule (STF2-CM1) accommodates eight 9-cell superconducting RF cavities and a superconducting quadrupole magnet in it to demonstrate the realization of a full-size ILC cryomodule.

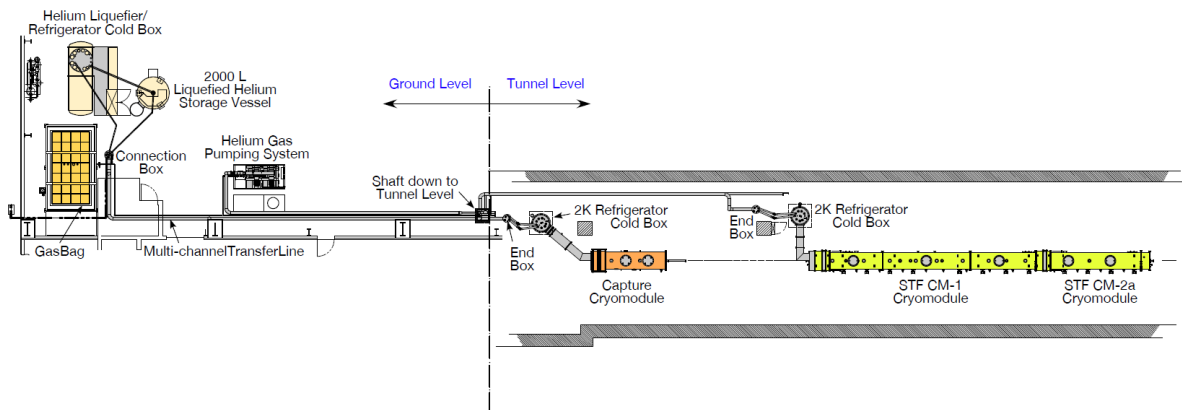


Figure 2-2: Layout of the superconducting test facility for International Linear collider cryomodule testing at KEK.

Superfluid Helium Cryogenic Systems at KEK

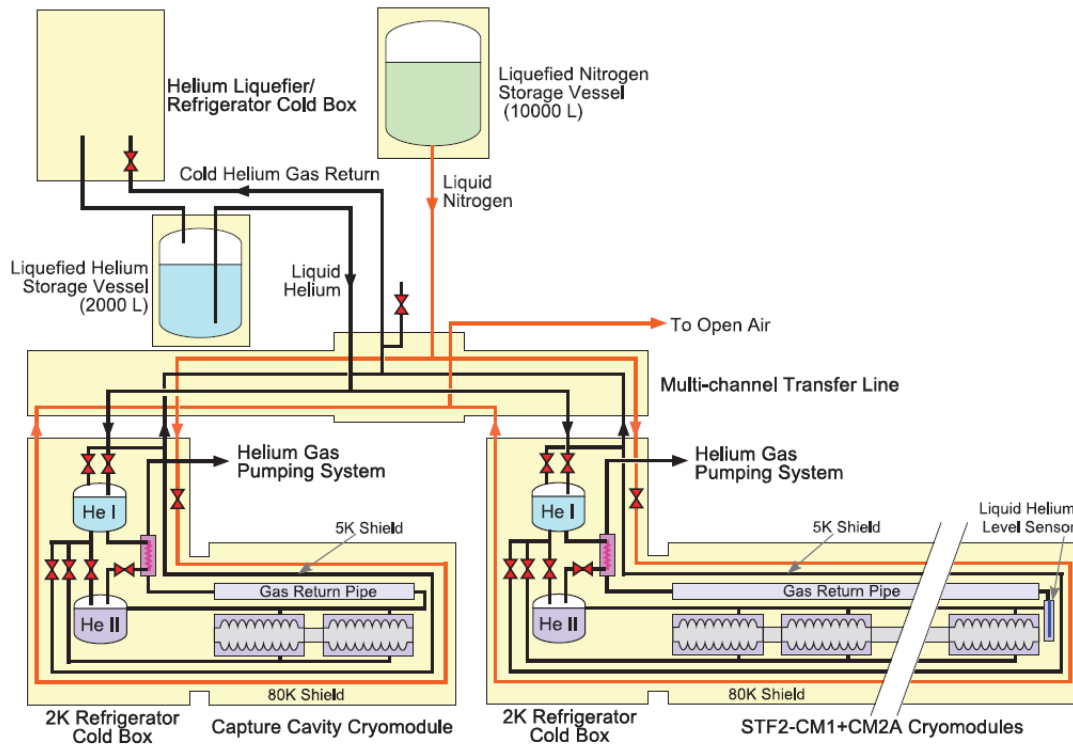


Figure 2-3: Schematic illustration of the cryogenic system for STF facility.



Figure 2-4: ILC cryomodule testing at the STF facility.

2.1.2. Compact energy recovery linac (cERL)

In the cERL accelerator project there are two types of SRF cavities, i.e. the Injector Linac cavities and the Main Linac cavities, as shown in Figure 2-5. The injector Linac has three 2-cell superconducting cavities, and the main ones have two 9-cell superconducting cavities. The cavities operate at a similar resonant frequency as the once in STF, but these cavities operate in continuous wave (CW) mode. This operation mode produces larger dynamic heat load than the pulse mode from the STF system. The estimated heat load from an SRF cavity of the Main Linac is about 25 W at 15 MV/m of accelerating voltage. The helium liquefier/refrigerator and its storage vessel is of the same specification as the STF cryogenic system. The compression capacity of the helium circulation compressor is 2500 m³/hr.

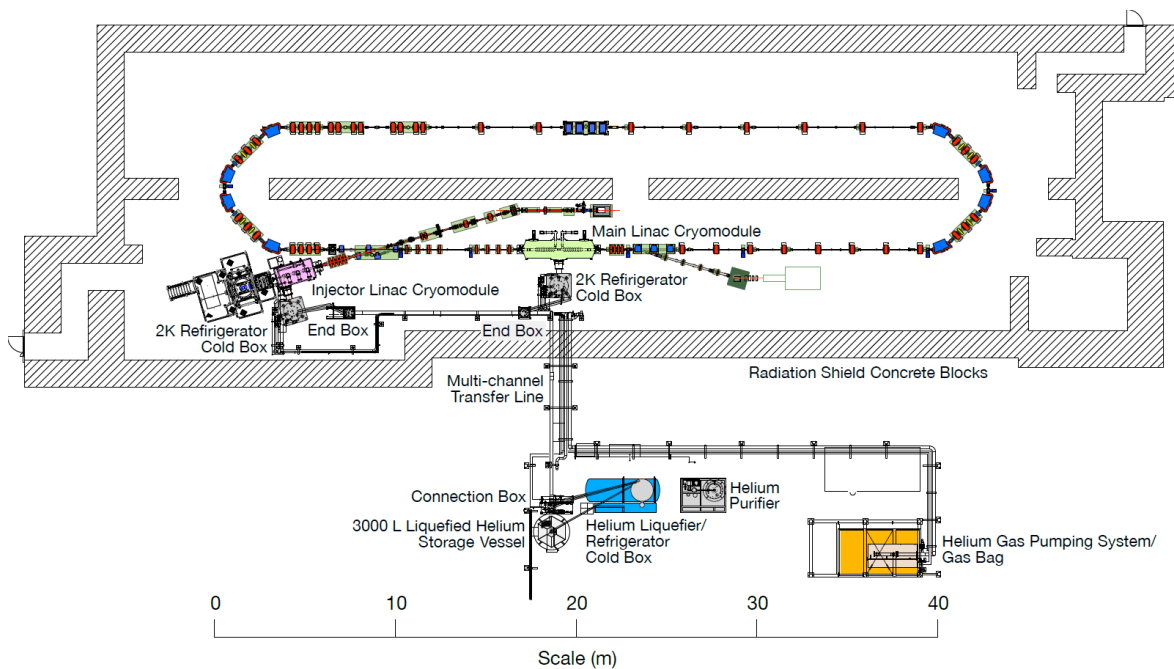


Figure 2-5: Layout of the cERL facility at KEK.

Superfluid Helium Cryogenic Systems at KEK

The helium pumping system consists of 8 rotary vane pumps (EM275 + EH1200) that have the ability to produce 80 W of refrigeration capacity at 2.0 K. The superfluid helium cryogenic system and the cryomodules are located on the ground level of the cERL test facility. The two 2K refrigerator cold boxes and the cryomodules are placed inside the radiation shield, surrounded with concrete blocks for radiation protection. The multi-channel transfer line connects the helium liquefier/refrigerator, the 3000 L liquefied helium storage vessel and the 2K refrigerators through the concrete blocks [17]. The static heat load from the Injector Linac cryomodule and the Main Linac cryomodules is 16 W and 14 W, respectively. The dynamic heat loss from each cavity is about 8.5 W at 5 MV/m accelerating voltage, with the total dynamic heat loss of about 76 W under simultaneous operation of both the Injector and the Main Linac [17].

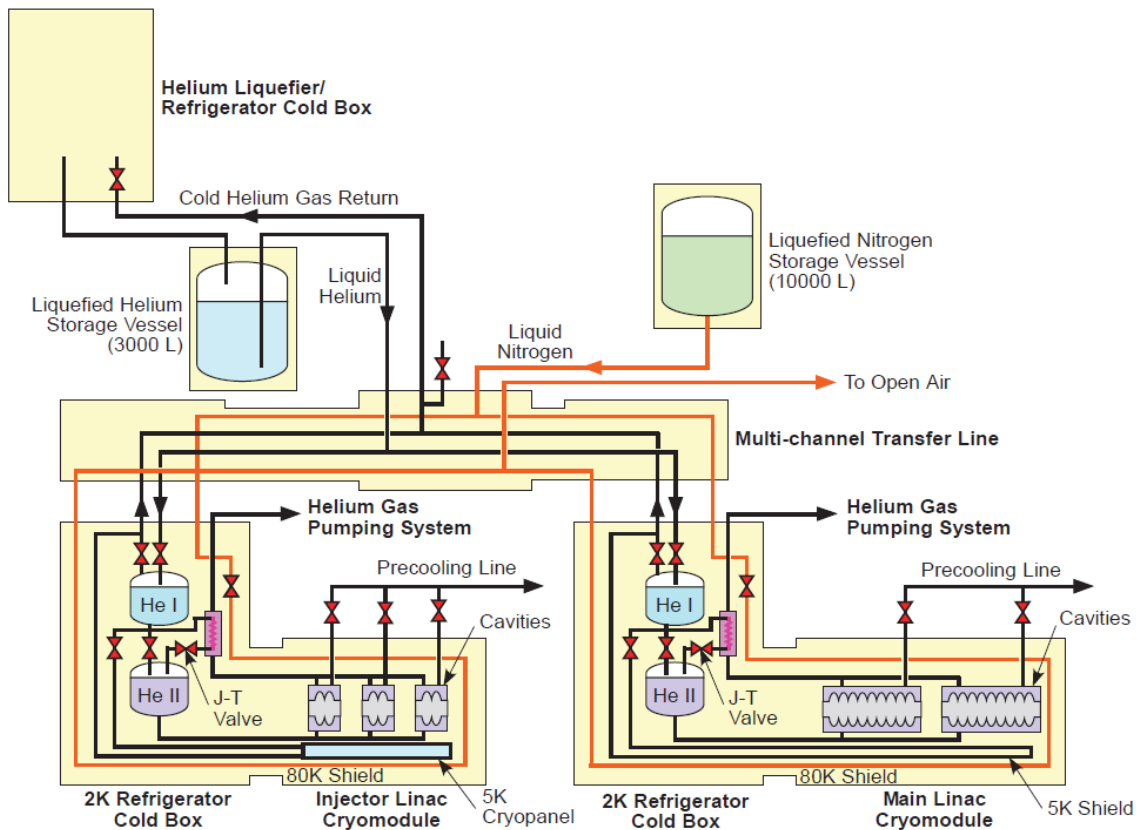


Figure 2-6: Schematic illustration of the cryogenic system for cERL facility.

2.1.3. Pumping system at KEK

The pumping system is one of the most important components for the superfluid helium cryogenic system. It is employed to produce 3.13 kPa absolute pressure on the 2.0 K He II bath to cool the SRF cavities to their operating temperatures. In large scale cryogenic systems (kW range), such as for Large Hadron Collider (CERN) and LCLS-II (SLAC). They employ cold compressors to compress the outgoing low-pressure gas to atmospheric pressures. Small-scale cryogenic systems installed at cERL and STF employ a combination of Edwards EM175 or EM275 vacuum pumps in series with Edwards's mechanical booster pump EH1200. These pumps operate at warm conditions with the inlet temperature of GHe being at room temperature. The data provided by the manufacturer suggests that each EM175 and EM275 pump in series with EH1200 should produce 15 W and 20.2 W of pumping capacity respectively, at 3.13 kPa inlet pressure. Due to an unknown reason, the measured capacity is 10.4 W and 13.6 W, respectively. The pumping capacity data for both cryogenic systems is shown in Figure 2-7. The flow meter's operational pressure and temperature was approximately 105 kPa and 303 K.

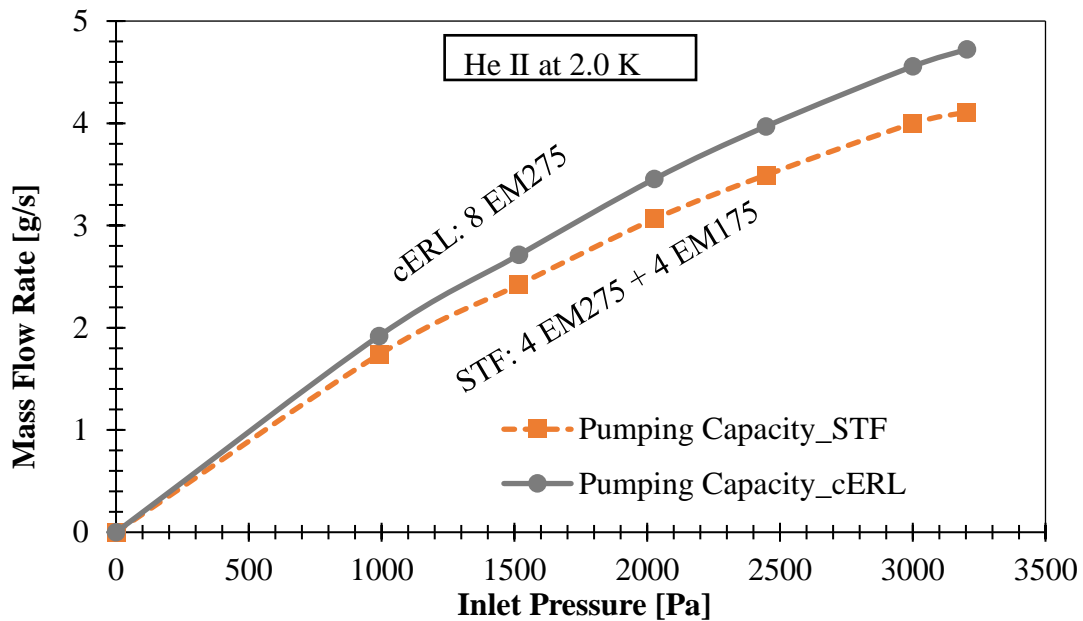


Figure 2-7: Pumping capacity of the cryogenic systems with respect to the inlet pressure to the pumps for 2.0 K operation.

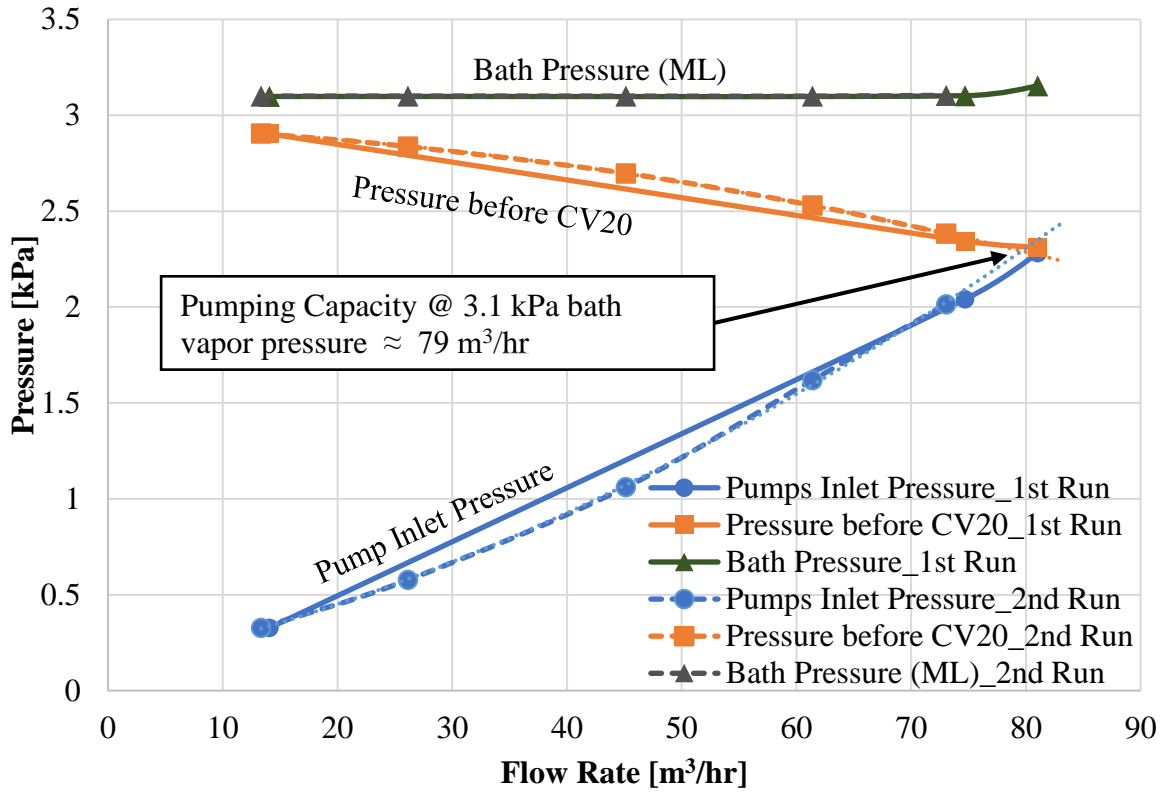


Figure 2-8: Pumping capacity of the cERL pumping system for the Main Linac 2K Cold box operation.

Furthermore, the pumping capacity of the vacuum pumps keeps on decreasing with a lower inlet pressure of the GHe to vacuum pumps, as seen in Figure 2-7. The effect of lowered inlet pressure (< 3.13 kPa) to the vacuum pumps occurs due to the GHe pressure drop (ΔP) through the 2K HX and cryogenic transfer lines, causing the pumps to operate at an inlet pressure of < 3.13 kPa, hence also reducing the density of the GHe being pumped out, as seen in figure 2-8. The pumping capacity of the cERL pumping system was measured and the pumping capacity of STF pumping system was extrapolated from it. It was determined that the pumping capacity from the Main Linac 2K cold box was approximately 79 m³/hr or (86 W) at 3.13 kPa bath pressure. The GHe ΔP at the maximum flow rate of 79 m³/hr was 800 Pa, which forces the pumps to work at lower inlet pressure, hence lowering the pumping capacity. The flow rate to the pumps below the maximum pumping capacity is controlled by the CV20 throttling valve to artificially reduce the inlet pressure to the pumps.

2.2. 2K Heat Exchanger at KEK

2.2.1. Laminated-finned type heat exchanger

A 2K heat exchanger is designed to be a gas to liquid counter flow heat exchanger, with higher surface heat transfer area for the sub atmospheric GHe. The heat exchanger should have the ability to work in LHe temperatures, especially between 1.9 K - 4.4 K. The size of the heat exchanger is also an important factor, since it has to be compact enough to satisfy space requirements in the 2K refrigerator cold box. To subcool LHe from 4.4 K to 2.2 K with 2.0 K GHe, the effectiveness should be $> 84\%$. Below 2.2 K, the specific heat capacity starts to rise steeply for LHe, hence making difficult to reduce its temperature. Moreover, with superfluid transition the heat transfer capability of the He II with solid material is significantly reduced, due to its very low heat transfer coefficient and high apparent thermal conductivity. Hence, for the required high effectiveness and compactness of the heat exchanger, it is essential to use a counter flow type heat exchanger. Only this type of flow arrangement can guarantee high effectiveness for a given surface area and specific heat capacity rate. Another important factor is the mass flow rate of both LHe and GHe. It depends on the heat load transferred to the superfluid helium from the SRF cavity housed in the cryomodules during its operation. During the steady state operation, the level of superfluid helium in the helium tank of SRF cavity is maintained, hence the mass flow rate of GHe and LHe flowing through the 2K heat exchanger remains similar to each other.

The 2K HXs consists of helically coiled tubes and laminated fins made of oxygen-free copper (OFC) with two variants: Type I (old version) for flow rates up to 1 g/s and Type II (2K HX_1) for flow rates up to 3.5 g/s, both in counterflow arrangement designed by Prof. K. Hosoyama, as shown in Figure 2-9. For this study the focus would be on the 2K HX_1, since it can handle higher flow rates and is being currently used for the cryogenic systems at KEK. The hot LHe (4.4 K) flows through the helical tube and the cold GHe (2.0 K) flows around the fins brazed on the helical tube, in counter flow direction. The laminated fins, as seen in Figure 2-9, provide extra surface area for the cold GHe to facilitate better enthalpy

Superfluid Helium Cryogenic Systems at KEK

extraction from the hot LHe flowing through the helical tube. The surface area density of the 2K HX_1 is approximately $220 \text{ m}^2/\text{m}^3$, which can be improved for the optimization of its design [18], [19]. This heat exchanger has to operate in adverse pressure conditions varying from 125 kPa to 0 kPa absolute, hence it becomes necessary to have as low amount of brazed and welded connections as possible to ensure leak tightness. This is where the advantage of this kind of heat exchanger geometry comes into play, as it has only two brazed connection point for the helical tube, separating the LHe and GHe flow streams at 125 kPa and 3.13 kPa absolute pressure. It can also pass high pressure test requirement without deformity due it geometry.

The heat load from the cryomodules is determined from the flow rate of GHe being evacuated by the GHe pumping system to maintain the required vapor pressure of 3.13 kPa (2.0 K) inside the helium cryostat, housing the SRF cavity. The level of superfluid helium in the two-phase line above the helium tank of SRF cavity is maintained during the operation by supplying LHe continuously into the cryomodule.



Figure 2-9: Cross section of the 2K HX_1 (on the left) and its helically coiled tube (on the right).

Table 2-1: Geometric parameters of the 2K HX_1.

Geometric Parameters	Dimensions
	2K HX_1
Helical tube parameters	
Tube outer diameter (thickness)	6 (t1) mm
Helix diameter (pitch)	75 (9) mm
Number of loops	30
Fin dimensions (circle sector)	With hole
Sector radius	35 mm
Sector angle	50 degrees
Fin thickness	0.5 mm
Hole diameter	10 mm
Total dimensions	
Heat exchanger axial length	277 mm
Heat exchanger diameter	82 mm

2.2.2. 2K heat exchanger manufacturing procedure

The main components of this 2K heat exchanger are OFC tube and fins, and their dimensions are summarized in Table 2-1. The tube is twisted in a helical form by twisting it over a 75 mm diameter mandrel, which is then placed on a fixture for the subsequent procedure of placing fins on the tube one by one. The fins are fixed in place using thin stainless-steel wires and the gap between adjacent fins is kept constant to create geometry according to the design. With every fin, a silver brazing wire is wound in parallel to the helical tube. This is necessary to braze the fins on the helical tube in the vacuum furnace later on.

After all the fins are placed on the helical tube, the heat exchanger assembly is inserted in a vacuum furnace, which is pumped out to pressure below 10^{-3} Pa with a diffusion pump backed by a rotary pump. When the required vacuum conditions are achieved, the heater in the furnace is turned on and the temperature of the heater is increased incrementally to > 800 °C and kept at that temperature for an hour, for the silver brazing wire to melt and flow between the fins and the helical tube. Then the heater is turned off and the heat exchanger is allowed to cool down naturally in the furnace under vacuum conditions. Cooldown under vacuum conditions is necessary to avoid oxidation of the heat exchanger body. When the

Superfluid Helium Cryogenic Systems at KEK

cooldown is completed and temperature is below 100 °C, argon gas is supplied inside to break the vacuum and the heat exchanger is removed. The stainless-steel wires are cut off and the heat exchanger is placed in a SS316L shell. The brazed stainless-steel sleeve on open ends of the helical tube is TIG welded to the ICF flange for external connections. The step by step procedure is shown in Figure 2-10.

Superfluid Helium Cryogenic Systems at KEK



Helically wound OFC tube



Fins with Silver brazing wire on helical tube



Finished 2K HX



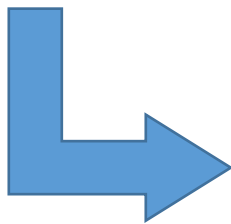
2K HX after vacuum brazing



2K HX in furnace



Vacuum furnace for brazing



2K HX in SS316L shell

Figure 2-10: 2K heat exchanger manufacturing process

Chapter 3. OBJECTIVE OF THE STUDY

3.1. Performance of the 2K HX_1

As mentioned in the previous chapter, the 2K HX_1 is employed in the superfluid helium cryogenic systems to reduce hot LHe temperature from 4.4 K to > 2.2 K with the cold GHe at 2.0 K. The performance of a heat exchanger is defined by a term known as “effectiveness” which is the ratio of actual heat transfer to the maximum possible heat transfer between the fluids flowing through it. The performance of the 2K HX_1 needs to be determined at the maximum possible flow rate through the superfluid helium cryogenic systems. In this case, the two fluids are LHe and GHe flowing through the heat exchanger in counter-flow direction. The mass flow rate of both fluids remains equal to each other during the steady state operation. Also, it is important to determine the GHe pressure drop (ΔP) through the heat exchanger body, since this parameter dictates the pumping capacity of the vacuum pumps, hence the cooling capacity of the superfluid helium cryogenic system. The methodologies employed to determine the effectiveness of the 2K heat exchanger are:

- Theoretical investigation to understand the behavior of this heat exchanger.
- Computational fluid dynamics (CFD) and finite difference methods (FDM) to form a numerical model of the 2K HX_1.
- Experimental analysis using the heat exchanger test stand.

3.2. Optimization of the 2K HX_1

Once the performance of 2K HX_1 is determined experimentally and is validated with its numerical model, the design needs to be optimized to better the performance of the 2K HX_1 for the superfluid helium cryogenic systems. Furthermore, it is necessary to study the influence of the 2K HXs’ GHe ΔP on the helium pumping system’s ability to produce superfluid helium efficiently. The optimization of the 2K HX_1 will be performed in two phases:

Objective of the Study

1. At first, a parametric study would be conducted with the aid of the 2K HX_1's numerical model to improve its current design. It will be a component-based parametric study to improve the effectiveness while keeping the GHe ΔP similar to or lower than the 2K HX_1.
2. In the next step, the cooling capacity of the superfluid helium cryogenic systems will be studied with respect to the current and improved 2K HXs designs. The main purpose of this study will be to maximize the superfluid helium production rate for the cryogenic systems. The optimized 2K HX will be the one that maximizes the superfluid helium production for STF and cERL cryogenic system.
3. The optimized design will be verified experimentally for its performance with the aid of the heat exchanger test stand.

3.3. Assumptions for Heat Transfer Analysis

For the 2K HX analyses, necessary assumptions and constraints are considered for the specified problem. The assumptions for theoretical and numerical analyses are:

- The most important assumption is that the 2K heat exchanger works under steady state condition i.e. constant flow rates and time independent fluid and material properties.
- No heat transfer is happening with the surroundings i.e. adiabatic conditions at the wall from the surroundings. For CFD analyses, heat loss or gain from surroundings can be modeled, but is usually neglected.
- The overall and individual heat transfer coefficients of fluids are constant i.e. independent of time, position and temperature.
- The specific heat capacity of fluids is varied for the 2K HX. For CFD and FDM to get solutions closer to the experiment results, it would be useful to vary specific heat capacity of fluids with respect to temperature and pressure.

Objective of the Study

- Other properties of fluids like kinematic viscosity, thermal conductivity and density are also considered constant throughout the flow field in the heat exchanger for theoretical analyses. In case of CFD, properties will be varied with respect to temperature and pressure.
- The boundary condition at the inlets and outlets are uniform through the cross section and there is no misdistribution at the inlet. This condition is also true for CFD where correct boundary conditions are important for the solver. CFD analyses also require uniform conditions at the outlet.
- In this case, there should be no volumetric phase change in the flow field. In case phase change happens on the walls, it would be at a constant pressure and temperature and then specific heat constant of that fluid will become infinite.

Chapter 4. COMPUTATIONAL FLUID DYNAMICS

4.1. Introduction

Computers have been used for decades now to solve different kind of fluid problems. The set of equations that describe the processes of momentum, heat and mass transfer are known as the Navier-Stokes equations. These partial differential equations were derived in the early nineteenth century and have no known general analytical solution but can be discretized and solved numerically.

Computational fluid dynamics (CFD) are a simulation of physical fluid dynamics system using mathematical problem formulations and numerical methods. Using the physical properties of the fluids and solids, we formulate the mathematical model of the physical problem and solve it iteratively. It solves the Navier-Stokes equation, which is the governing equation of all fluids ideal or real in fluid dynamics. The problem is solved by discretizing the physical model using finite difference, finite element or finite volume methods. The advantages of CFD are that it is cheap, time efficient, a safe way to solve a physical problem and it can be used to solve many kinds of problems like aerospace, fluid dynamics, chemical processes, hydraulics, etc.

In this chapter, the theory behind the CFD simulations is briefly given. Furthermore, the necessary steps that are followed to set up a CFD simulation for heat transfer analyses and their descriptions are provided for the researchers not versed with it.

4.1.1. Governing equations of fluid dynamics

Using general mass, energy and momentum conservation laws, momentum, continuity and energy equations can be derived for a flowing fluid [20].

Continuity equation,

$$\frac{D\rho}{Dt} + \rho \frac{\partial U_i}{\partial x_i} = 0. \quad (4.1)$$

Momentum Equation,

$$\rho \frac{DU_i}{Dt} + \rho U_i \frac{\partial U_i}{\partial x_i} = -\frac{\partial P}{\partial x_j} - \frac{\partial \tau_{ij}}{\partial x_j} + \rho g_j. \quad (4.2)$$

Energy equation,

$$\rho C_p \frac{DT}{Dt} + \rho C_p U_i \frac{\partial T}{\partial x_i} = -P \frac{\partial U_i}{\partial x_i} + \lambda \frac{\partial^2 T}{\partial x_i^2} - \tau_{ij} \frac{\partial U_j}{\partial x_i}, \quad (4.3)$$

where,

$$\tau_{ij} = -\mu \left[\frac{\partial U_j}{\partial x_i} + \frac{\partial U_i}{\partial x_j} \right] + \frac{2}{3} \delta_{ij} \mu \frac{\partial U_k}{\partial x_k}, \quad (4.4)$$

and U_i is vector of velocity $U_{x,y,z}$, p is pressure, τ_{ij} is stress tensor, T is static temperature, ρ is density, λ is thermal conductivity and C_p is specific heat capacity.

4.2. ANSYS CFX® for CFD Analysis

ANSYS® provides a comprehensive suite of CFD codes for modeling fluid flow and other related physical phenomena, to solve the governing equations for fluid dynamics and much more. With these solutions, we can simulate a wide range of phenomena: aerodynamics, combustion, hydrodynamics, mixtures of liquids/solids/gas, particle dispersions, reacting flows, heat transfer, etc. Steady state and transient flow phenomena are easily and quickly solved. The graphic results of an ANSYS CFX® or ANSYS FLUENT CFD® software simulation will show us fluid flow, particle flow, heat transfer, chemical reactions, combustion, and other parameters. The basic steps to setup a numerical problem in CFX is shown in Figure 4-1 [21];

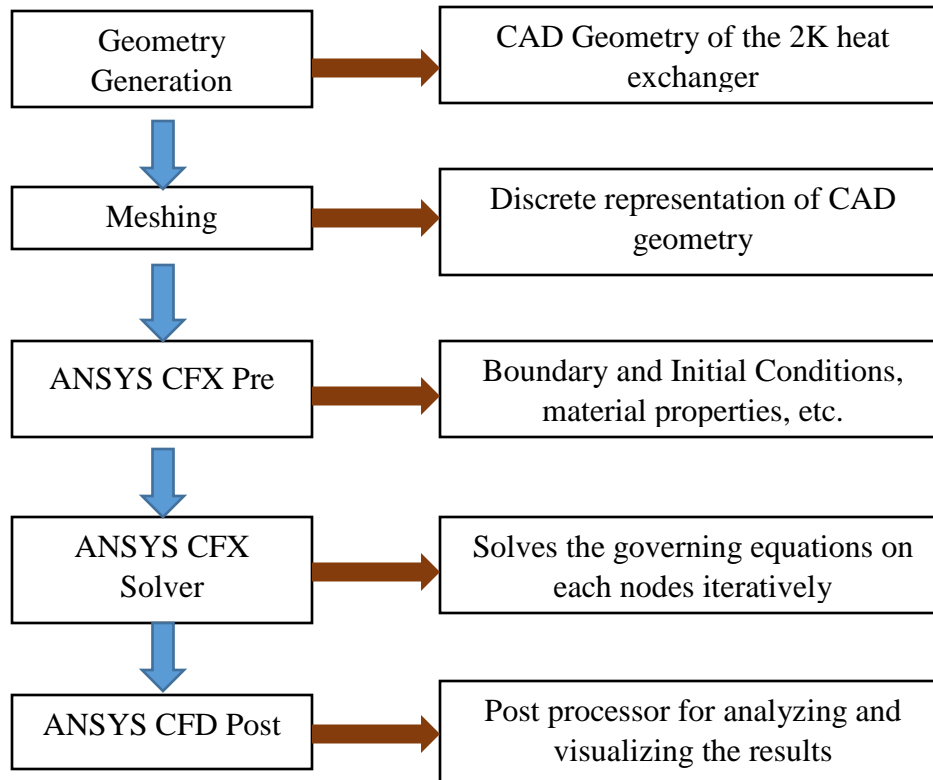


Figure 4-1: Flow diagram for numerical analysis on ANSYS CFX

4.2.1. Geometry

The first step of setting up the CFD problem is to model an accurate geometry of the problem to be discretized. For the 2K heat exchanger, it consists of three domains: liquid helium (LHe), gaseous helium (GHe) and the heat exchanger body separating the two fluid domains. The fluid domains do not transfer any mass from one fluid to another, hence no mixing of fluids happens. For the simulation, the LHe domain was not modeled to reduce the computational load on the workstation, and to save time to simulate multiple configurations at different flow rates. The CAD models for the domains were modeled with the aid of Autodesk Inventor®, and an example is shown in Figure 4-2.

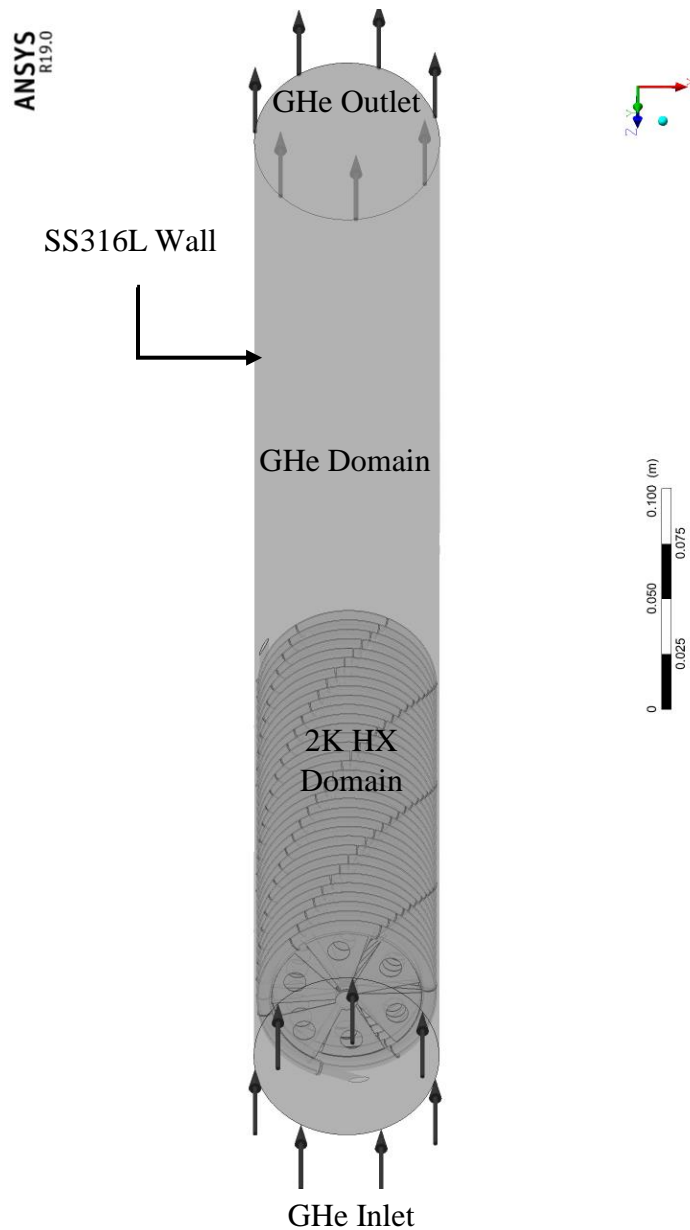


Figure 4-2: 2K heat exchanger CAD geometry from AutoDesk Inventor®

4.2.2. Meshing

Meshing is one of the most important step in any of the CFD simulations, since it can drastically affect the results obtained from a simulation. It is a discrete representation of the geometry that partitions space into elements (cells or zones) over which the equations can be

approximated. Zone boundaries can be free to create computationally best-shaped zones, or they can be fixed to represent internal or external boundaries within a model. The geometry has to be captured with sufficient mesh resolution to capture all key component of flow physics.

For the 2K HX_1 geometry, the meshes were created using proximity and curvature criteria. The proximity and curvature meshing algorithm gives sufficient refinement within the small gap and has the effect of automatic refinement in all regions of higher curvature. This was essential due to the complexity of the design of the 2K HX_1, which had small gaps and higher curvature regions, as shown in Figure 4-3. As we move closer to the walls in a flow domain, the velocity of the fluid reduces non-linearly to zero (no slip condition). To capture the velocity gradient near the walls and accurately capture the boundary layer, inflated meshes needed to be created for any wall bounded turbulent and laminar flows. Inflation meshes were created over the fins and the tube surface in the GHe flow volume to take into consideration the y^+ value for turbulence modeling. y^+ is an important factor, which helps to resolve the boundary layer of the flowing fluid over a solid surface. To check the mesh quality: orthogonal angle, expansion factor and aspect ratio have to be in an acceptable range for realistic and accurate solution.

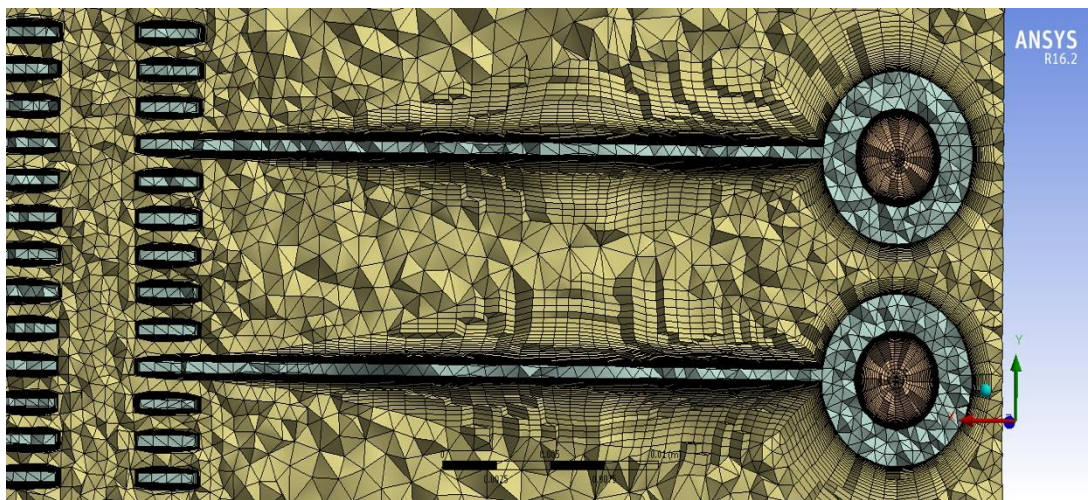


Figure 4-3: Inflation and Proximity mesh around Fins.

4.2.3. Mesh independency test

Numerical solutions are heavily dependent on the size and shape of the mesh. In the case of turbulent flow, resolving the viscous sublayer involves the full resolution of the boundary layer, and is required where wall-bounded effects are of high priority (pressure drop, heat transfer, etc.). Estimating the first cell height is an important issue in meshing, since it dictates the y^+ of the fluid flow in that volume. Adding inflation cells near the wall helps to resolve the boundary layer precisely. The y^+ dictates the turbulence model being used for the fluid flow region.

For the 2K HX as mentioned before, proximity and curvature were used as a method to create finer meshes around the fins and walls interacting with GHe. The meshes should be fine enough that the solution is independent of the mesh resolution. The mesh independency test was carried out using 4 loops of the heat exchanger at 1.55 g/s flow rate. The initial and boundary conditions for GHe are given in Tables 4-2 to 4-4 and the turbulence model employed for the LHe flow domain is $k-\epsilon$ scalable turbulence model with $y^+ > 30$. The results of mesh independency test are shown below:

Table 4-1: Mesh independency test results

No. of Loops	LHe Inlet T(K)	LHe Outlet T(K)	GHe Inlet T(K)	GHe Outlet T(K)	Q (W)	Effectiveness (%)	Criterion Changed	Error (%)
4	4.4	4.01	2	2.341	3.01	22.77	$Y^+=1.1$, 8 million meshes	-
4	4.4	4.013	2	2.338	2.985	22.59	Mesh increased from 8 to 24 million for GHe Domain	<1
4	4.4	4.005	2	2.344	3.035	22.96	$Y^+= 0.36$ reduced from 1.1 for GHe Domain	<1

4.2.4. CFX-Pre setup

CFX-Pre is used to define and specify the simulation settings and physical parameters required to describe the flow problem [22]. The simulation setup depends on the problem under investigation. Setting up the simulation typically requires the following data [23]:

- 1) **Materials**: The fluids and solids must be defined correctly with all the thermo-physical properties required for the model.
- 2) **Domain**: defining the domain properties relevant to the simulation.
- 3) **Boundary Condition**: set of conditions on the surfaces of the domains to fully define the flow problem
- 4) **Simulation Type**: steady state or transient simulation
- 5) **Solver Control**: a set of controls that define the way CFX-Solver solves the problem.

4.2.5. Material properties

The fluid and solid domains have to behave realistically with all the physical properties needed to be defined for the simulated model with respect to pressure and temperature. The detailed behavior of the materials under the influence of flow conditions, such as pressure and temperature can have a critical effect on the accuracy of CFD predictions.

ANSYS CFX has a database of material properties for a wide range of liquids, gases, and solids. Both ideal and real fluid behavior can be modeled using well-established equations of state. If a simulation should involve a material not included in the material database, it is possible to use CFX expression language (CEL) and user functions to form the said new material. In this simulation, the helium's thermo-physical properties had to be created using the data acquired from NIST and HEPAK® software [24], [25]. The material properties were varied with respect to temperature and pressure using the CEL language and user functions. The materials created for the heat exchanger simulation are: Gaseous Helium and Oxygen-free copper (OFC).

4.2.6. Domains

Domains are regions of space for fluids and solids to iteratively solve the fluid flow and heat transfer equations. These are the control volume occupied by the fluids and solids. It is beneficial to provide initial conditions of the flow and solid domains to give a good initial guess for the solver manager. In the specified problem, there are two domains:

- **OFC Domain:** A solid domain through which heat is being transferred from LHe to GHe without any mass transfer. The initial conditions for the domain are shown in table 4-2:

Table 4-2: Initial conditions for the OFC Domain

Domain	Material	Temperature (K)	Heat Transfer
OFC	OFC	4.4 or below	Thermal Energy

- **Gaseous Helium Domain:** The domain through which gaseous helium (cold fluid) flows and gains heat from the OFC domain.

Table 4-3: Initial conditions for the GHe

Domain	Material/Fluid	Temperature (K)	Turbulence Intensity (%)	Heat Transfer	Turbulence Model	Wall Function
Gaseous He	Gaseous He	2	4.2 to 5.1	Thermal Energy	k- ω SST	Automatic

4.2.7. Boundary conditions

A set of conditions are required to be satisfied completely or a part of the boundary of a region in which a set of differential equations are to be solved. The boundary conditions are initial conditions used to initiate the solution for the domains. For the simulations, the mass flow rate of GHe at the inlet will be varied till 5 g/s, hence the turbulence intensity varies too.

The outlet condition will be kept constant with a total pressure set at around 2.8 kPa absolute. It is lower than the operating pressure of the He II bath at 3.13 kPa to compensate for the pressure drop in the 2K HXs. The walls of the 2K HXs are set at a constant temperature to eliminate thermal resistance from the solid body. The wall of the stainless-steel shell for the heat exchanger is set to be adiabatic to eliminate the unknown quantity of heat in-leak from the surroundings. The boundary conditions used for the two domains defined in the previous section are shown in Table 4-4:

Table 4-4: Boundary Conditions for fluid and solid boundaries in the domains.

Boundary	Material	Mass Flow (g/s)	Turbulence Intensity (%)	Static Temperature (K)	Total Pressure (bar)
GHe Inlet	GHe	5	4.3	2	-
GHe Outlet	GHe	-	-	-	0.028
Interface with OFC	OFC Cu	-	-	2	-
Wall	SS316L	-	-	Adiabatic	-

Turbulence Intensity

Turbulence intensity is a factor that is specified at the inlet boundary for the 2.0 K GHe. The turbulence intensity for a compressible flow through a pipe is studied in detail by F. Russo and N.T Basse, and is given by the empirical relation for a pipe flow below [26], [27]:

$$\text{Turbulence Intensity, } I = 0.153 \times \text{Re}^{-0.110}, \quad (4.5)$$

where Re is the Reynolds number of the fully developed flow in a pipe.

When the value of turbulence intensity for an internal pipe flow is provided, the inlet turbulence energy is calculated using:

$$k_{\text{inlet}} = 1.5 \times I^2 U^2, \quad (4.6)$$

where U is the inlet velocity of the fluid and the turbulence dissipation is calculated using:

$$\varepsilon_{\text{inlet}} = \rho C_{\mu} \frac{k^2}{\mu_t}, \quad (4.7)$$

where turbulent viscosity is:

$$\mu_t = 1000 \times I \times \mu. \quad (4.8)$$

The turbulent length scale (l_t) is related to the turbulence kinetic energy and turbulence dissipation by:

$$\varepsilon_{\text{inlet}} = \frac{k^{3/2}}{l_t}. \quad (4.9)$$

4.2.8. Solver Control

It gives the user a control over the units of mass, length, time, temperature, angle and convergence control. The convergence of a simulation is measured by residual mean square value. The residual is a measure of the local imbalance of each equation. The default RMS target is 1E-4, which is a good degree of accuracy, but we might consider using as small a residual as possible up to 1E-6, which is a tightly converged solution for fluid flow problems. The lowest convergence from the heat exchanger simulation have been around 1E-6 for GHe domain. The reason for the residuals not being high enough are,

- The problem is inherently transient due to the periodic nature of GHe and not steady state for the flow regime.
- The gap between the spatial arrangements of the fins cause wake and vortex generation, which is a cause of transient state for the GHe flow.
- The mesh is not fine enough to capture the periodic nature of flow. Due to the problem being 3-Dimensional, the memory requirement is very high.

Monitor Points

Certain monitor points in the flow field through output control measure the solution convergence. If they remained constant and oscillating at a certain mean value, the simulation was considered to be converged with the residual target defined before.

4.3. Modelling Flow near the Wall

An important issue in the accurate prediction of turbulent flows is the formulation and the numerical treatment of the equations in regions close to solid walls. The near-wall formulation determines the accuracy of the wall shear stress and the wall heat transfer predictions. It also has an influence on the development of boundary layers, including the onset of separation. Typically, the two following approaches are used to model the flow in the near-wall region [20]:

The Wall-function Method: In the scalable wall-function approach, the viscosity affected sublayer region is bridged by employing empirical relations to provide near wall boundary conditions for the mean flow and turbulence transport equations. The major advantage of the wall function approach is that it conserves valuable computer resources and it avoids the need to account for viscous effects in the turbulence model. One of the major drawbacks of the wall function approach is that the predictions depend on the location of the point nearest to the wall and is sensitive to the near-wall meshing. Refining the mesh does not necessarily give a solution of increasing accuracy. The wall-function approach in ANSYS CFX is an extension of the method of Launder and Spalding. In the log-law region, the near wall tangential velocity is related to the wall-shear-stress, by means of a logarithmic relation. The logarithmic relation for the near wall velocity is given by [20]:

$$u^+ = \frac{U_t}{u_\tau} = \frac{1}{K} \ln(y^+) + C, \quad (4.10)$$

where

$$y^+ = \frac{\rho \Delta y u_\tau}{\mu} \quad \text{and} \quad u_\tau = \left(\frac{\tau_w}{\rho} \right)^{0.5} . \quad (4.11)$$

Here u^+ is the near wall velocity, u_τ is the friction velocity, U_t is the known velocity tangent to the wall at a distance from the wall, y^+ is the dimensionless distance from the wall, τ_w is the wall shear stress, K is the von Karman constant and C is a log-layer constant depending on the wall roughness.

In case of **Scalable Wall function**, for the log law equation at separation points, the near wall velocity, U_t , approaches zero. In the logarithmic region, an alternative velocity scale, u^* can be used instead of U_t :

$$u^* = C_\mu^{\frac{1}{4}} K^{\frac{1}{2}} . \quad (4.12)$$

This scale has the useful property that it does not go to zero, if U_t is zero. Based on this definition, the following explicit equation for u_τ can be obtained:

$$u_\tau = \frac{U_t}{\frac{1}{K} \ln(y^*) + C} . \quad (4.13)$$

The absolute value of the wall shear stress τ_w ,

$$\tau_w = \rho u^* u_\tau \quad \text{and} \quad y^* = \frac{\rho \Delta y u^*}{\mu} . \quad (4.14)$$

The problem of inconsistencies in the wall-function method for fine meshes can be overcome with the use of the scalable wall function formulation developed by ANSYS CFX. The basic idea behind the scalable wall-function approach is to limit the y^* value used in the logarithmic formulation by a lower value of $\tilde{y}^* = \max[y^*, 11.06]$, where 11.06 is the value of y^* at the intersection between the logarithmic and the linear near wall profile shown in Figure 4-4. The computed \tilde{y}^* is not allowed to fall below this limit, therefore all mesh points are outside the viscous sublayer and all fine mesh inconsistencies are avoided [20].

The Low-Reynolds-number method: An alternative approach to the use of wall functions is to use a fine-grid analysis extending through the viscosity-affected sublayer close to the wall. The low-Reynolds number (Re) approach requires a very fine grid in the near-wall zone. In laminar sub-layer region ($y^+ < 5$) the inertial forces are not dominant and the flow exhibits laminar characteristics. With models like $k-\omega$ and SST, it is possible to resolve the boundary layer for better accuracy. For flows at low Re, it can cause an error in the displacement thickness of up to 25%. It is therefore desirable to offer a formulation, which will automatically switch from wall-functions to a low Re near the wall formulation, as the mesh is refined. The main idea behind the present formulation is to blend the wall value for between the logarithmic and the near wall formulation [20].

The automatic wall treatment allows a consistent y^+ insensitive mesh refinement from coarse grids, which does not resolve the viscous sublayer, to fine grids placing mesh points inside the viscous sublayer. Note that for highly accurate simulations, like heat transfer predictions, a fine grid with y^+ around 1 is recommended. The flux for the k-equation is artificially kept to be zero, and the flux in the momentum equation is computed from the velocity profile. The equations are as follows:

Flux for the momentum equation,

$$F_U = -\rho u_\tau u^* , \quad (4.15)$$

$$u^* = \sqrt[4]{\left(\sqrt{\frac{\mu}{\rho} \left| \frac{\Delta U}{\Delta y} \right|}\right)^4 + (\sqrt{a_1 k})^4} \quad \text{and} \quad u_\tau = \sqrt[4]{(u_\tau^{\text{vis}})^4 + (u_\tau^{\text{log}})^4} , \quad (4.16)$$

where

$$u_\tau^{\text{vis}} = \frac{\mu}{\rho} \left| \frac{\Delta U}{\Delta y} \right| \quad \text{and} \quad u_\tau^{\text{log}} = \frac{U}{\frac{1}{K \log(y^+)} + C} . \quad (4.17)$$

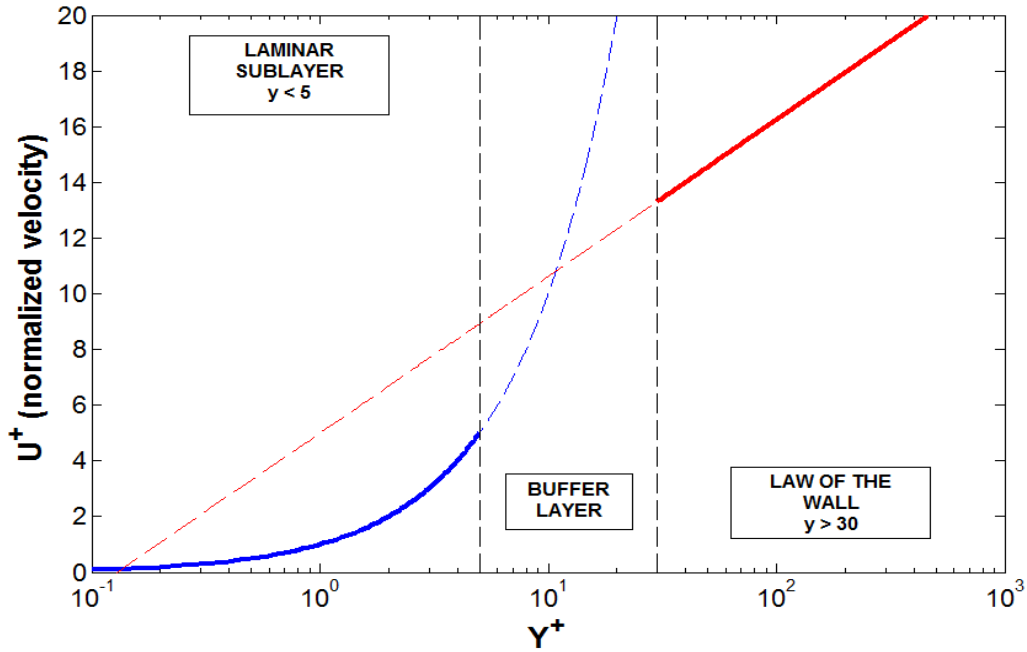


Figure 4-4: Y^+ for different region of turbulent boundary layer [28].

4.3.1. Heat Flux in the Near-Wall Region

Heat flux at the wall can be modeled using the scalable wall function approach or the automatic wall treatment. Using similar assumptions as those above, the non-dimensional near-wall temperature profile follows a universal profile through the viscous sublayer and the logarithmic region. The non-dimensional temperature, T^+ , is defined as [20]:

$$T^+ = \frac{\rho C_p u^* (T_w - T_f)}{q_w}, \quad (4.18)$$

where T_w is the temperature at the wall, T_f the near-wall fluid temperature, C_p the fluid heat capacity and q_w the heat flux at the wall. The above equation can be rearranged to get a simple form for the wall heat flux model:

$$q_w = \frac{\rho C_p u^* (T_w - T_f)}{T^+}. \quad (4.19)$$

In case of **Automatic wall treatment**, the thermal boundary layer is modeled using the thermal law-of-the-wall function of B.A. Kader. Then, the non-dimensional temperature distribution is modeled by blending the viscous sublayer and the logarithmic law of the wall. This can be modeled as [12], [20]:

$$T^+ = Pr \times y^* \times e^{-\Gamma} + [2.12 \ln(y^*) + \beta] e^{-\frac{1}{\Gamma}}, \quad (4.20)$$

$$\beta = \left(3.84 \times Pr^{\left(\frac{1}{3}\right)} - 1.3 \right)^2 + 2.12 \ln(Pr). \quad (4.21)$$

4.4. Turbulence Modelling

Turbulence usually occurs when the inertia forces becomes significantly larger compared to viscous forces, which is characterized by the Reynolds number. The Navier-Stokes equations describes both laminar and turbulent flows, but the turbulent flows can span a large range of length and time scale, and would generally involve length scales smaller than practical finite volume mesh. The direct numerical simulations would require computing power that is not available [20].

4.4.1. Two equation turbulence models

Two-equation turbulence models offer a good compromise between numerical effort and computational accuracy. In these models both velocity and length scale are solved using separate transport equations. The two well-known widely used two-equation models are $k-\varepsilon$ and $k-\omega$ models. The turbulent viscosity is modeled as the product of a turbulent velocity and turbulent length scale. In two-equation models, the turbulent velocity scale is computed from the turbulent kinetic energy, which is provided from the solution of its transport equation. The turbulent length scale is estimated from two properties of the turbulence field, usually the turbulent kinetic energy and its dissipation rate. The dissipation rate of the turbulent kinetic energy is provided from the solution of its transport equation [20].

4.4.2. The k-epsilon model in ANSYS CFX

In this model k is the turbulence kinetic energy, and is defined as the variance of the fluctuations in velocity, ε is the turbulence eddy dissipation. The k - ε model introduces two variable into the system of equations governing fluid flow[20].

The continuity equation is:

$$\frac{\partial \rho}{\partial t} + \frac{\partial}{\partial x_j} (\rho U_j) = 0, \quad (4.22)$$

And the momentum equation becomes:

$$\frac{\partial \rho U_i}{\partial t} + \frac{\partial}{\partial x_j} (\rho U_i U_j) = -\frac{\partial p'}{\partial x_j} + \frac{\partial}{\partial x_j} \left[\mu_{eff} \left(\frac{\partial U_i}{\partial x_j} + \frac{\partial U_j}{\partial x_i} \right) \right] + S_M, \quad (4.23)$$

where U is the velocity, ρ is the density, S_M is the sum of body forces, μ_{eff} is the effective viscosity accounting for turbulence, and p' is the modified pressure. The k - ε model is based on the eddy viscosity concept, so that:

$$\mu_{eff} = \mu + \mu_t, \quad (4.24)$$

where μ_t is the turbulence viscosity. Moreover, the k - ε model assumes that the turbulence viscosity is linked to the turbulence kinetic energy and dissipation via the relation:

$$\mu_t = C_\mu \rho \frac{k^2}{\varepsilon}, \quad (4.25)$$

where $C_\mu = 0.09$ is a constant.

The differential transport equations for the turbulence kinetic energy (k) and turbulence dissipation rate (ε) provide the values of k and ε :

$$\frac{\partial (\rho k)}{\partial t} + \frac{\partial}{\partial x_j} (\rho U_j k) = \frac{\partial}{\partial x_j} \left[\left(\mu + \frac{\mu_t}{\sigma_k} \right) \frac{\partial k}{\partial x_j} \right] + P_k - \rho \varepsilon + P_{kb}, \quad (4.26)$$

$$\frac{\partial (\rho \varepsilon)}{\partial t} + \frac{\partial}{\partial x_j} (\rho U_j \varepsilon) = \frac{\partial}{\partial x_j} \left[\left(\mu + \frac{\mu_t}{\sigma_\varepsilon} \right) \frac{\partial \varepsilon}{\partial x_j} \right] + \frac{\varepsilon}{k} (C_{\varepsilon 1} P_k - C_{\varepsilon 2} \rho \varepsilon + C_{\varepsilon 1} P_{\varepsilon b}), \quad (4.27)$$

where $C_{\varepsilon 1} = 1.45$, $C_{\varepsilon 2} = 1.9$ are the Reynolds stress model constants, $\sigma_k = 1$ is the turbulence model constant for the k equation and $\sigma_\varepsilon = 1.3$ is the k - ε model constant.

P_{kb} and $P_{\varepsilon b}$ represent the influence of the buoyancy forces, P_k is the turbulence production due to viscous forces, which is modeled using:

$$P_k = \mu_t \left(\frac{\partial U_i}{\partial x_j} + \frac{\partial U_j}{\partial x_i} \right) \frac{\partial U_i}{\partial x_j} - \frac{2}{3} \frac{\partial U_k}{\partial x_k} \left(3\mu_t \frac{\partial U_k}{\partial x_k} + \rho k \right). \quad (4.28)$$

For incompressible flow, the second term in Equation 4.28 is negligible in terms of production of turbulence, and only becomes significant enough for regions of high velocity divergence or shocks. The buoyancy terms should be neglected for the GHe flow through 2K HX, as the effect of gravity is neglected for low dense fluid such as GHe, which has the density of $< 1 \text{ kg/m}^3$.

4.4.3. The k-omega model in ANSYS CFX

As mentioned before k - ω formulation is necessary for near wall treatment for low Reynolds number flows. This does not involve complex nonlinear damping functions that are necessary in k - ε models, hence is more accurate and robust. A low Reynolds k - ε model would require $y^+ < 0.2$ for near wall resolution, while for low Reynolds k - ω model would require at least $y^+ < 2$. Also, the k - ω model allows for smooth shift from low Reynolds number form to a wall function formulation, to shift to the k - ε model outside the sub-viscous layer. The k - ω model assumes that the turbulence viscosity is linked to the turbulence kinetic energy and turbulent frequency via the relation [20]:

$$\mu_t = \rho \frac{k}{\omega}. \quad (4.29)$$

4.4.4. The Wilcox k - ω model

This model solves two transport equations, the turbulent kinetic energy (k) and the turbulent frequency (ω), and its stress tensor is computed from the eddy-viscosity concept [20].

k -equation:

$$\frac{\partial(\rho k)}{\partial t} + \frac{\partial}{\partial x_j}(\rho U_j k) = \frac{\partial}{\partial x_j} \left[\left(\mu + \frac{\mu_t}{\sigma_k} \right) \frac{\partial k}{\partial x_j} \right] + P_k - \beta' \rho k \omega + P_{kb}. \quad (4.30)$$

ω -equation:

$$\frac{\partial(\rho \omega)}{\partial t} + \frac{\partial}{\partial x_j}(\rho U_j \omega) = \frac{\partial}{\partial x_j} \left[\left(\mu + \frac{\mu_t}{\sigma_\omega} \right) \frac{\partial \omega}{\partial x_j} \right] + \alpha \frac{\omega}{k} P_k - \beta \rho \omega^2 + P_{\omega b}. \quad (4.31)$$

P_k is the production rate of turbulence, which is calculated as in the k - ε model.

The model constants are given by:

$$\beta' = 0.09, \quad \alpha = \frac{5}{9}, \quad \beta = 0.075, \quad \sigma_k = 2, \quad \sigma_\omega = 2.$$

The unknown Reynolds stress tensor is calculated from:

$$\rho \overline{u_i u_j} = \mu_t \left(\frac{\partial U_i}{\partial x_j} + \frac{\partial U_j}{\partial x_i} \right) - \frac{2}{3} \delta_{ij} \left(\mu_t \frac{\partial U_k}{\partial x_k} + \rho k \right). \quad (4.32)$$

The buoyancy production term is included in the k -equation and can be toggled on to set it to production or production and dissipation. The buoyancy turbulence terms for the ω -equation are derived from P_{kb} and $P_{\varepsilon b}$ according to the transformation P_{kb} .

For the GHe flowing through the 2K HX geometry the buoyancy term is not necessary and is not turned on.

4.4.5. The baseline (BSL) k - ω model

The main issue with the Wilcox model is its strong sensitivity to the freestream conditions. Depending on the freestream ω a significant variation in result can be obtained, which is undesirable. To avoid that a blending function between k - ω near surface and k - ε model in the outer region was developed by Menter. The blending between k - ω near surface and k - ε model is by a blending function F_1 and the transformed k - ε model by a function $1 - F_1$. F_1 is equal to one near the surface and decreases to a value of zero outside the boundary layer. At the boundary layer edge and outside the boundary layer, the standard k - ε model is therefore recovered [20].

Wilcox model:

$$\frac{\partial(\rho k)}{\partial t} + \frac{\partial}{\partial x_j}(\rho U_j k) = \frac{\partial}{\partial x_j} \left[\left(\mu + \frac{\mu_t}{\sigma_{k1}} \right) \frac{\partial k}{\partial x_j} \right] + P_k - \beta' \rho k \omega, \quad (4.33)$$

$$\frac{\partial(\rho \omega)}{\partial t} + \frac{\partial}{\partial x_j}(\rho U_j \omega) = \frac{\partial}{\partial x_j} \left[\left(\mu + \frac{\mu_t}{\sigma_{\omega 1}} \right) \frac{\partial \omega}{\partial x_j} \right] + \alpha_1 \frac{\omega}{k} P_k - \beta_1 \rho \omega^2, \quad (4.34)$$

Transformed k - ε model:

$$\frac{\partial(\rho k)}{\partial t} + \frac{\partial}{\partial x_j}(\rho U_j k) = \frac{\partial}{\partial x_j} \left[\left(\mu + \frac{\mu_t}{\sigma_{k2}} \right) \frac{\partial k}{\partial x_j} \right] + P_k - \beta' \rho k \omega, \quad (4.35)$$

$$\begin{aligned} \frac{\partial(\rho \omega)}{\partial t} + \frac{\partial}{\partial x_j}(\rho U_j \omega) &= \frac{\partial}{\partial x_j} \left[\left(\mu + \frac{\mu_t}{\sigma_{\omega 2}} \right) \frac{\partial \omega}{\partial x_j} \right] + \\ &2\rho \frac{1}{\sigma_{\omega 2} \omega} \frac{\partial k}{\partial x_j} \frac{\partial \omega}{\partial x_j} + \alpha_2 \frac{\omega}{k} P_k - \beta_2 \rho \omega^2. \end{aligned} \quad (4.36)$$

Now multiplying the blending functions to the individual models gives the equations for the BSL model (including buoyancy):

$$\frac{\partial(\rho k)}{\partial t} + \frac{\partial}{\partial x_j}(\rho U_j k) = \frac{\partial}{\partial x_j} \left[\left(\mu + \frac{\mu_t}{\sigma_{k3}} \right) \frac{\partial k}{\partial x_j} \right] + P_k - \beta' \rho k \omega + P_{kb}, \quad (4.37)$$

$$\frac{\partial(\rho\omega)}{\partial t} + \frac{\partial}{\partial x_j}(\rho U_j \omega) = \frac{\partial}{\partial x_j} \left[\left(\mu + \frac{\mu_t}{\sigma_{\omega 3}} \right) \frac{\partial \omega}{\partial x_j} \right] + (1 - F_1) 2\rho \frac{1}{\sigma_{\omega 2} \omega} \frac{\partial k}{\partial x_j} \frac{\partial \omega}{\partial x_j} + \alpha_3 \frac{\omega}{k} P_k - \beta_3 \rho \omega^2 + P_{\omega b}. \quad (4.38)$$

The coefficients of the new model are a linear combination of the corresponding coefficients of the underlying models:

$$\Phi_3 = F_1 \Phi_1 + (1 - F_1) \Phi_2. \quad (4.39)$$

The coefficients are listed below:

$$\beta' = 0.09, \quad \alpha = \frac{5}{9}, \quad \beta = 0.075, \quad \sigma_{k1} = 2, \quad \sigma_{\omega 1} = 2$$

$$\beta_2 = 0.09, \quad \alpha_2 = 0.44, \quad \beta_2 = 0.0828, \quad \sigma_{k2} = 1, \quad \sigma_{\omega 2} = \frac{1}{0.856}.$$

4.4.6. The shear stress transport model (SST)

The k - ω based SST model accounts for the transport of the turbulent shear stress and gives accurate prediction of the onset and the amount of flow separation under adverse pressure gradients. The BSL model fails to properly predict onset and amount of flow separation from surfaces, due to not accounting transport of turbulent shear stress and over-predicting the eddy-viscosity. The proper transport behavior obtained by SST model is obtained by a limiter to the formulation of the eddy viscosity [20]:

$$v_t = \frac{a_1 k}{\max(a_1 \omega, SF_2)}, \quad (4.40)$$

where

$$v_t = \frac{\mu_t}{\rho}. \quad (4.41)$$

F_2 is a blending function similar to F_1 , which restricts the limiter to the wall boundary layer, as the underlying assumptions are not correct for free shear flows. S is an invariant measure of the strain rate.

Blending Functions

The blending functions formulation is based on the distance to the nearest surface and on the flow variables.

$$F_1 = \tanh(\arg_1^4), \quad (4.42)$$

with:

$$\arg_1 = \min \left(\max \left(\frac{\sqrt{k}}{\beta' \omega y}, \frac{500\nu}{y^2 \omega} \right), \frac{4\rho k}{CD_{kw} \sigma_{\omega 2} y^2} \right), \quad (4.43)$$

where y is the distance to the nearest wall, ν is the kinematic viscosity and:

$$CD_{kw} = \max \left(2\rho \frac{1}{\sigma_{\omega 2} \omega} \frac{\partial k}{\partial x_j}, 1 \times 10^{-10} \right), \quad (4.44)$$

$$F_2 = \tanh(\arg_2^2), \quad (4.45)$$

with:

$$\arg_2 = \max \left(\frac{2\sqrt{k}}{\beta' \omega y}, \frac{500\nu}{y^2 \omega} \right). \quad (4.46)$$

4.4.7. Selection of the turbulence model for the 2K HX geometry

As per assumptions for the analysis of the 2K HX in Chapter 3, the fluid flow through the 2K HX is in steady state condition. In the case of steady state flow, many kinds of turbulence models are available for modelling the fluid flow like Spalart-Allmaras, $k-\varepsilon$ based models and $k-\omega$ based models. According to the texts available from ANSYS, Spalart-Allmaras is not good for 3D flows. For the $k-\varepsilon$ model in ANSYS CFX®, only scalable wall function is available for selection, which is not ideal for resolving boundary layer separation and sub-viscous layers. According to Menter et al. [29] and ANSYS, the $k-\omega$ shear stress turbulence model predicts the results most closer to the experimental results for low-Reynolds number flows. For the GHe flow through 2K HX_1 body, where boundary layer separation, complex boundary layers and wake regions exists around the stack of fins and helical tubes, the low

Reynolds number $k-\varepsilon$ model would typically require a near wall resolution of $y^+ < 0.2$, while a low-Reynolds number $k-\omega$ model would require at least $y^+ < 2$, hence lower number of discrete elements during meshing. The advantage $k-\omega$ based models (SST) over $k-\varepsilon$ based models is its smooth transfer from low Reynolds number near-wall function to wall-functions outside the sub-viscous layer and would be the best for modelling the GHe flow through the 2K HX_1 body.

Although, large eddy simulation (LES) Model is the most accurate to develop flow through complicated geometry where eddy formation, vortex generation and vortex shredding occurs, which also happens in the case of 2K HX_1 geometry. Though, the LES models have some requirements:

- LES models are usually employed for transient flows and have to be solved by taking minuscule time steps, to solve the problem.
- The computational power required to solve the problem is high due to the smaller time steps and higher mesh count.
- The higher mesh count becomes necessary to resolve the boundary layer around the fins.
- The smaller time step increases the computational load and time to complete a simulation.

Furthermore, the area of research is the interaction between the flow and the walls rather than resolving the eddy formation accurately between the fins. Due to the limitation in computing power, the author decided to go with the steady state modeling as a compromise using the $k-\omega$ SST Automatic model to solve the flow problem for GHe.

Chapter 5. METHODOLOGY FOR EFFECTIVENESS DETERMINATION OF 2K HX

5.1. Logarithmic Mean Temperature Difference (LMTD)

Method

LMTD is a method that relates the total heat transfer rate to quantities such as inlet and outlet fluid temperatures, total surface area and overall heat transfer coefficient, to design and predict the performance of the heat exchanger. The relations can be obtained by applying energy balance equations to the hot and cold fluids with negligible heat transferred to the surroundings. The heat transfer rate between fluids (\dot{Q}) is determined by ignoring the potential and kinetic energy changes, and applying steady flow energy equation as [11], [30],

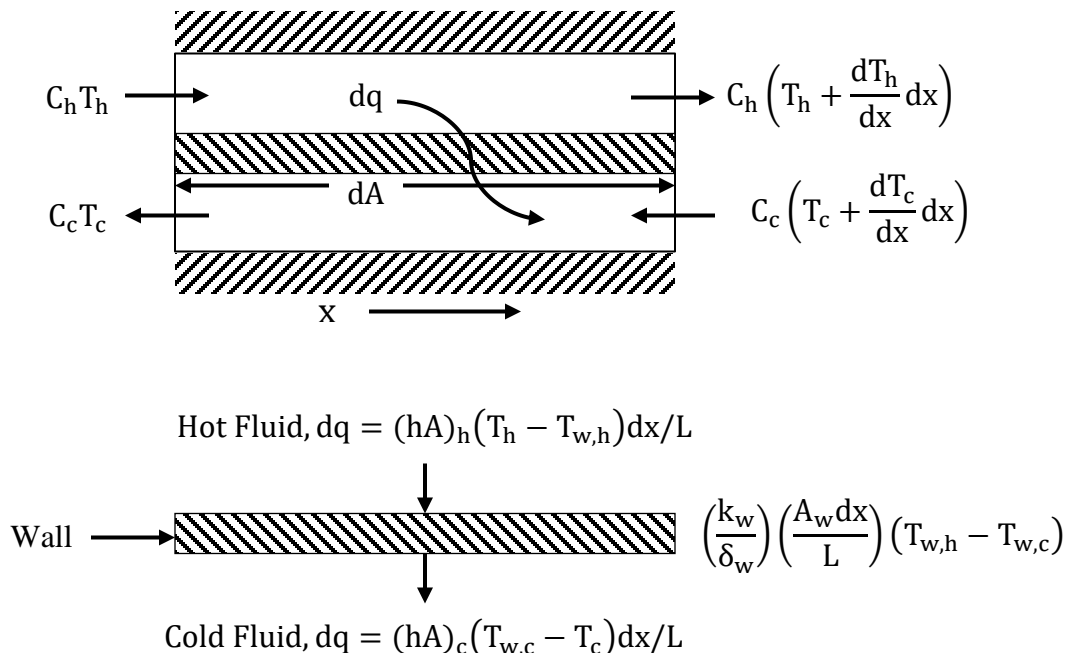


Figure 5-1: Heat transfer through a differential element of a heat exchanger between hot and cold fluid.

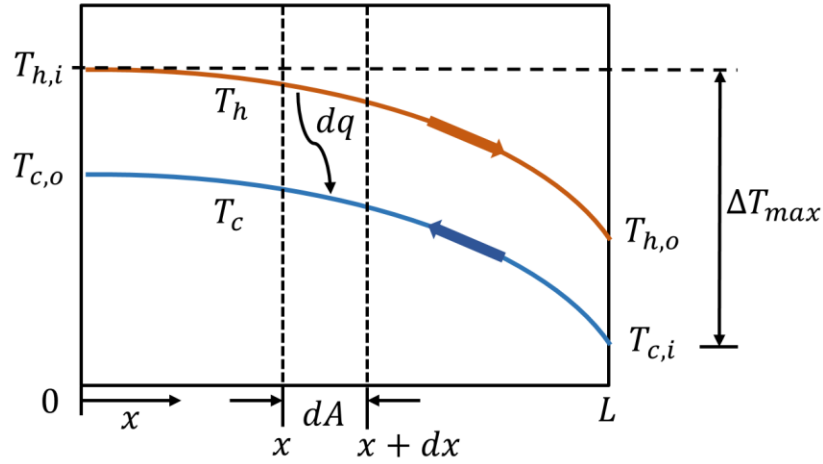


Figure 5-2: Temperature profile for a counterflow heat exchanger.

$$\dot{Q} = \dot{m}_h c_h (T_{hi} - T_{ho}) = \dot{m}_c c_c (T_{co} - T_{ci}), \text{ for counterflow heat exchanger} \quad (5.1)$$

where \dot{m}_h and \dot{m}_c are the mass flow rate of the incoming hot and cold fluid, c_h and c_c are specific heat capacities of the hot and cold fluid respectively, T_{hi} and T_{ho} are inlet and outlet temperatures of the hot fluid, T_{ci} and T_{co} are inlet and outlet temperatures of the cold fluid in a counter flow heat exchanger, as shown in Figure 5-1. Another important useful expression may be obtained by comparing the heat transfer rate to the temperature difference between the hot and cold fluids:

$$\Delta T = T_h - T_c. \quad (5.2)$$

This expression can be related to Newton's law of cooling for convection heat transfer over a solid body. The overall heat transfer coefficient is used instead of the individual heat transfer coefficient, since the value of ΔT varies at different point on the heat exchanger, a mean value being required for effective heat transfer to and from the heat exchanger.

$$\dot{Q} = UA\Delta T_m, \quad (5.3)$$

where ΔT_m is the mean temperature difference between hot and cold fluids.

Methodology for Effectiveness Determination of 2K HX

The term UA is influenced by the heat transfer coefficient of fluids transferring heat with each other and the thermal conductivity of a solid mass through which heat is being transferred. For a heat exchanger with two fluids transferring heat through a solid body, UA is:

$$\frac{1}{UA} = \frac{1}{(\eta_o h A)_h} + (R_f)_h + R_w + (R_f)_c + \frac{1}{(\eta_o h A)_c}, \quad (5.4)$$

where h_h and h_c is the heat transfer coefficient for hot fluid and cold fluid respectively, A is the surface area, R_{f_h} and R_{f_c} are the fouling resistances given by the impurities deposited on the surface of the heat exchanger, on the hot fluid and the cold fluid side, respectively, R_w is the wall resistance and η_o is the overall surface efficiency.

The logarithmic mean temperature difference for the counter-flow heat exchanger is derived by taking a differential element, dx, a differential surface area of dA, a temperature difference of d(ΔT) and integrating from inlet to outlet as seen in Figure 5-2, we get a well-known Equation 5.5 [11], [30].

$$\Delta T_m = \frac{[(T_{h,i} - T_{c,o}) - (T_{h,o} - T_{c,i})]}{\ln \left[\frac{(T_{h,i} - T_{c,o})}{(T_{h,o} - T_{c,i})} \right]}. \quad (5.5)$$

5.2. Effectiveness of a Heat Exchanger

Effectiveness is a type of measurement for thermal performance of a heat exchanger. It is defined as the ratio of actual heat transfer, to the maximum possible heat transfer from the heat exchanger [11].

$$\varepsilon = \frac{\dot{Q}}{\dot{Q}_{\max}}, \quad (5.6)$$

The maximum heat transfer rate from hot fluid to cold fluid for heat exchangers of constant specific heat capacity can be expressed as:

Methodology for Effectiveness Determination of 2K HX

$$\dot{Q}_{\max} = (\dot{m}c_p)_{\min}(T_{hi} - T_{ci}) = C_{\min}\Delta T_{\max}, \quad (5.7)$$

where ‘ ε ’ is the heat exchanger effectiveness to be determined. c_p is the specific heat capacity of the working fluid and C_{\min} is the minimum heat capacity out of both fluids. It is also idealized that there is no fluid leakage from one flow stream to other.

The amount of heat transferred through a counterflow heat exchanger, such as the 2K heat exchanger from the energy balance equation, can be determined from Equation 5.8:

$$\dot{Q} = C_h(T_{hi} - T_{ho}) = C_c(T_{co} - T_{ci}), \quad (5.8)$$

To achieve the maximum possible heat transfer (\dot{Q}_{\max}) for the condition $C_h < C_c$ for an infinite heat transfer area, the temperature of hot fluid will reach to the inlet temperature of the cold fluid i.e. $T_{ho} = T_{ci}$. Therefore, \dot{Q}_{\max} will be:

$$\dot{Q}_{\max} = C_h(T_{hi} - T_{ci}) = C_h\Delta T_{\max}, \quad (5.9)$$

The heat exchanger effectiveness from Equation 5.6 can be rewritten as for $C_h < C_c$,

$$\varepsilon = \frac{\dot{Q}}{\dot{Q}_{\max}} = \frac{C_h(T_{hi} - T_{ho})}{C_{\min}(T_{hi} - T_{ci})}, \quad (5.10)$$

These relations are valid when the specific heat capacity doesn't vary with respect to temperature or the change in the specific heat capacity with respect to temperature is minimalistic. To determine the accurate heat transfer between fluids when the variation in heat capacity is significantly high, as in the case for LHe from 4.4 K to 2.2 K, it is necessary to consider variation of the specific heat capacity with respect to temperature. The methodology employed to consider this property variation is shown in the next section.

5.2.1. Effectiveness with variable thermo-physical properties

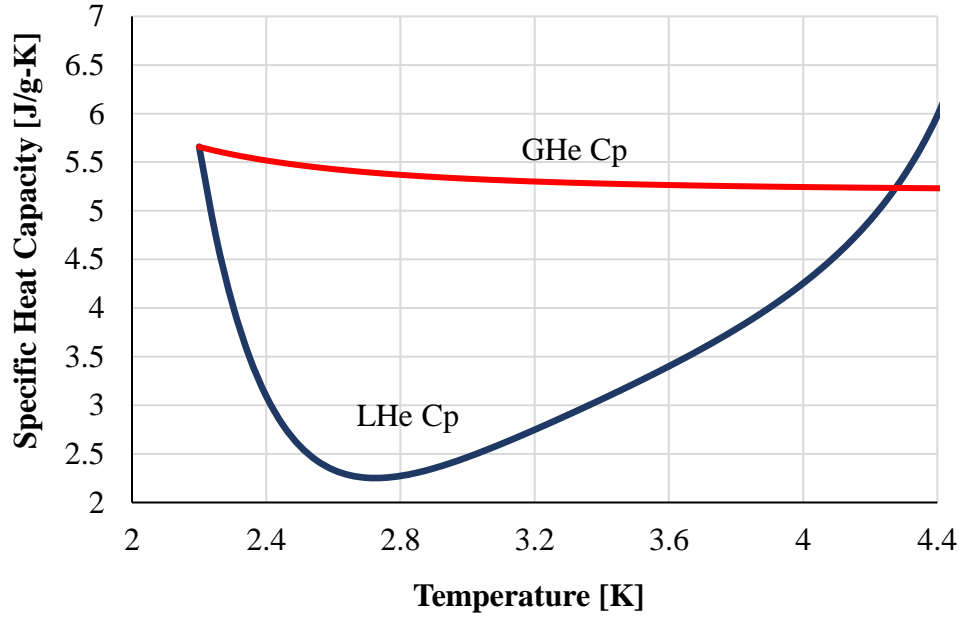


Figure 5-3: Specific heat capacity variation with respect to temperature for LHe and GHe.

If the specific heat capacity of the fluid varies drastically with respect to temperature, as in Figure 5-3, then it becomes necessary to use numerical methods to take the property variation into consideration. So, based on the energy balance consideration on the differential fluid element with length dx in Figure 5-1, the amount of heat transferred between fluids is:

$$dq = C_h dT_h = -C_c dT_c . \quad (5.11)$$

In this case, T_h and T_c represent the bulk temperature of hot and cold fluids.

The heat transfer rate applied individually to fluid and solid element is:

$$dq = \begin{cases} (\eta_o hA)_h (T_h - T_{w,h}) dx/L \\ \frac{(kA)_w (T_{w,h} - T_{w,c}) dx}{\delta_w} \\ \frac{L}{(\eta_o hA)_c (T_{w,c} - T_c) dx/L} \end{cases} . \quad (5.12)$$

After deriving the relations for individual temperature differences for the fluid and solid elements, adding them up and rearranging them, we get:

Methodology for Effectiveness Determination of 2K HX

$$dq = \frac{U_1 A (T_h - T_c) dx}{L}, \quad (5.13)$$

where U_1 represents the local overall heat transfer coefficient for element dx , but for the heat exchanger we treat local U_1 as similar to the overall heat transfer coefficient U for the entire heat exchanger. In addition, L is the total heat exchanger length, and δ_w is the wall thickness.

If the heat transfer coefficient of fluids is known, then it is possible to determine the overall heat transfer coefficient. From Equation 5.13, ordinary differential equations for both fluids can be formed, as shown below:

$$\text{For hot fluid: } \dot{m} C_{ph} \frac{dT_h}{dx_h} + \frac{UA_h}{l_h} (T_h - T_c) = 0, \quad (5.14)$$

$$\text{For cold fluid: } \dot{m} C_{pc} \frac{dT_c}{dx_c} + \frac{UA_c}{L} (T_h - T_c) = 0. \quad (5.15)$$

Here the mass flow rates of both fluids are equal, as in the case of 2K HX, the specific heat capacity of respective fluids are being varied with respect to temperature (6th order polynomial) and also $dx_h = l_h dx_c / L$. Usually, in a heat exchanger $UA_h \approx UA_c \approx UA$. The length that the fluid flows is different for both hot and cold fluids. In the case of 2K HX_1, the length of helical tube where the hot fluid (LHe) has to flow through is $l_h = 7 \text{ m}$ for 30 loops, but the axial length through which the cold fluid (GHe) has to travel is only 0.28 m. With these parameters and the coupled Equations 5.14 and 5.15, the temperature profile of the fluids through the 2K heat exchanger will be determined. The coupled equation is solved numerically with the help of Mathematica® [14]. With the known temperature profile, the specific enthalpy of individual fluids (H) can be determined at the heat exchanger's boundaries. The effectiveness for the heat exchanger can be determined from the relation given below, if the minimum heat capacity fluid is hot fluid:

$$\text{Effectiveness, } \varepsilon = \frac{\dot{m}(H_{h,i} - H_{h,o})}{\dot{m}(H_{h,i} - H_{h@c,i})}. \quad (5.16)$$

Here $H_{h@c,i}$ is the hot fluid enthalpy at cold fluid inlet temperature.

5.3. Fin Efficiency

There are situations where just increasing the heat transfer coefficient is insufficient to obtain desired heat transfer rate. The best way to improve the heat transfer rate is to increasing the surface area across where the convection occurs, and is usually employed with the aid of fins that extend from the wall to the surroundings. In heat exchangers, extended surfaces are used to enhance the heat transfer between solid and an adjoining fluid [11], [30].

For an annular fin, as shown in Figure 5-4, the inner diameter at the wall is ' r_1 ', the outer diameter is ' r_2 ', and a uniform thickness ' δ '. The cross-sectional area, $A_c = 2\pi r\delta$, varies with radius r and the surface area is expressed as $A_s = 2\pi(r^2 - r_1^2)$, the general form of temperature profile through an annular fin becomes:

$$\frac{d^2T}{dr^2} + \frac{1}{r} \frac{dT}{dr} - \frac{2h}{k\delta}(T - T_\infty) = 0. \quad (5.17)$$

with $m^2 \equiv 2h/k\delta$ and $\theta \equiv T - T_\infty$,

$$\frac{d^2\theta}{dr^2} + \frac{1}{r} \frac{d\theta}{dr} - m^2\theta = 0. \quad (5.18)$$

The equation above is a modified Bessel equation of zero order, and its solution is of the form:

$$\theta(r) = C_1 I_0(mr) + C_2 K_0(mr). \quad (5.19)$$

If the temperature at the base of the fin is prescribed, $\theta(r_1) = \theta_b$, and an adiabatic tip is presumed, $d\theta/dr|_{r_2} = 0$, the temperature distribution through an annular fin may be given in the form:

$$\frac{\theta}{\theta_b} = \frac{I_0(mr)K_1(mr_2) + K_0(mr)I_1(mr_2)}{I_0(mr_1)K_1(mr_2) + K_0(mr_1)I_1(mr_2)}. \quad (5.20)$$

For a fin with non-uniform cross-section, the fin efficiency (η_f) is determined from the correlations shown below:

$$\eta_f = \frac{q_f}{h2\pi(r_2^2 - r_1^2)\theta_b} = \frac{2r_1}{m(r_2^2 - r_1^2)} \frac{K_1(mr_1)I_1(mr_2) - I_1(mr_1)K_1(mr_2)}{K_0(mr_1)I_1(mr_2) - I_0(mr_1)K_1(mr_2)} \quad (5.21)$$

Here, h is the heat transfer coefficient of the fluid flowing over a fin, k is the thermal conductivity of the fin material and δ is the thickness of the fin.

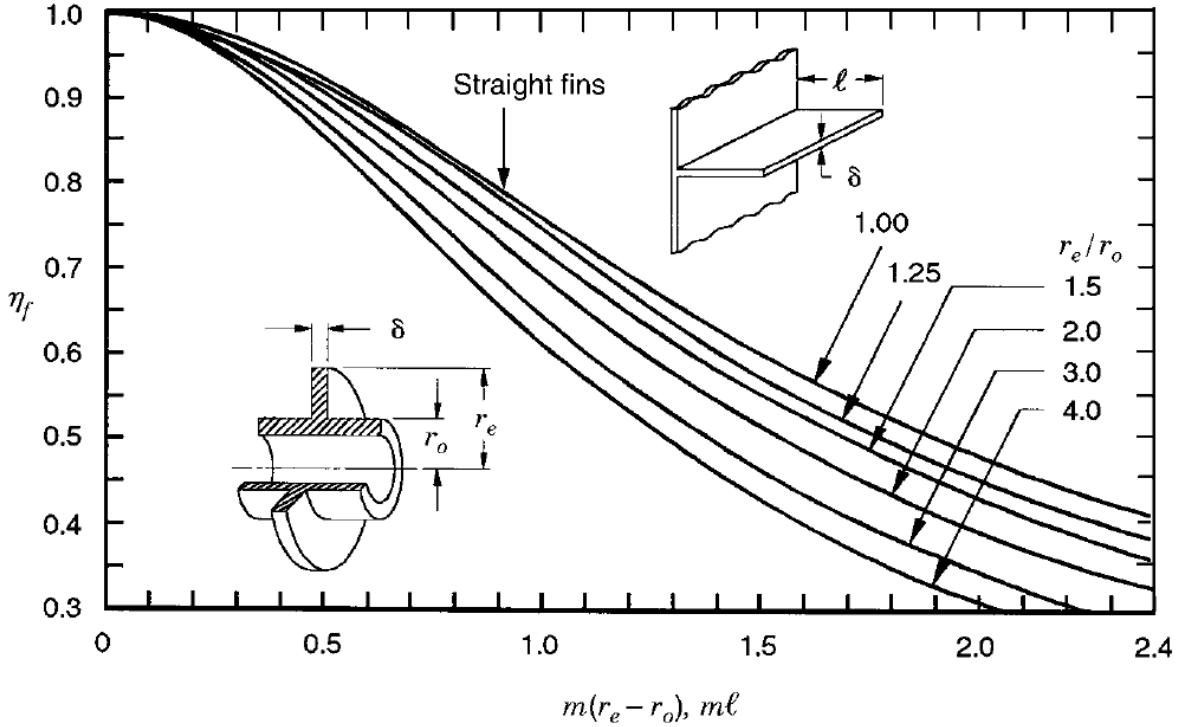


Figure 5-4: Fin efficiencies for annular and straight fins [11].

5.3.1. Fin efficiency for the 2K HX_1 fin

The fins in the 2K HX_1 are shaped as a sector of a circle whose outer diameter is 35 mm and has a constant thickness of 0.5 mm. The cross-sectional area of the fin through which the heat flows, is always varying with radius similar to the annular fin shown in Figure 5-4. The fin is laminated to the helical tube and its maximum cross-sectional area is near the helical tube and keeps on reducing with increasing radius. The Figure 5-5 shows the fin used for the 2K HX_1.

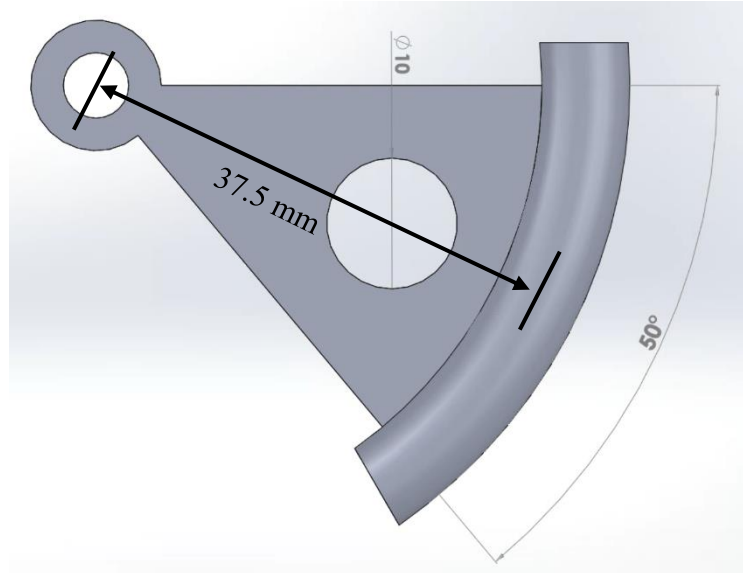


Figure 5-5: Fin structure employed for the 2K HX_1.

For this fin, the radius is $r_1 = 3.5 \text{ mm}$ and $r_2 = 34.5 \text{ mm}$, and its thickness being $\delta = 0.5 \text{ mm}$. To simplify the fin efficiency calculation, the fin geometry will be simplified by foregoing the hole in the fin. The heat flow through the fin is similar to the heat flow through an annular fin on a tube, with variable radius and constant thickness. The factor, m , for this kind of fin structure can be determined by:

$$m^2 = \frac{2h}{k\delta} . \quad (5.22)$$

where the heat transfer coefficient of GHe, h , flowing through fins will be dependent on its flow rate. The fin efficiency will then be determined from Equation 5.21.

5.3.2. Overall surface efficiency

The fin efficiency characterizes the performance of a single fin, the overall surface efficiency is for an array of fins and the base surface to which they are attached. The overall fin efficiency (η_o) is defined as the total heat transfer rate through the base and fins, with respect to the maximum heat transfer rate when the fins are maintained at the same temperature as the base [11], [30].

$$\eta_o = \frac{q_t}{q_{\max}} = 1 - \frac{NA_f}{A_t} (1 - \eta_f). \quad (5.23)$$

Here, A_f is area of a single fin, N is the number of fins and A_t is the total surface area consisting of base and fin area.

In the 2K heat exchanger, the number of fins (N) for 30 loops of helical tube is approximately 180 and the ratio of the area of fins plus the total area of the base (helical tube + fins) is approximately 0.43. With the fin efficiency obtained from Section 5.3.1, the overall surface efficiency can be determined.

5.4. Effect of Longitudinal Conduction on Effectiveness

In a heat exchanger, temperature gradients exist in both fluids and in the separating wall, in the fluid flow direction. This cause heat conduction in the wall and in the fluid from hotter to colder temperature region, and it may affect the heat transfer rate from the hot fluid to the cold fluid. Usually the conduction through fluids is negligible through most of the heat exchangers except the liquid metal heat exchangers [11]. The heat transfer through the separating walls can cause heat transfer by conduction from the hotter to the colder parts of the region, flattening the wall temperature distribution and reducing the performance of the heat exchanger. The influence of heat conduction in the wall is prevalent in compact heat exchangers designed for high effectiveness (approximately > 80%) and with short flow length. If a linear conduction profile is considered through the wall, the longitudinal conduction rate is:

$$q_k = k_w A_k \frac{T_{w,1} - T_{w,2}}{L}, \quad (5.24)$$

Here k_w is the thermal conductivity of the wall, A_k is the wall cross-sectional area, $T_{w,1}$ and $T_{w,2}$ is the end temperatures of the heat exchanger body, and L is the length of the heat flow path.

Methodology for Effectiveness Determination of 2K HX

With no loss to the surroundings, the heat transferred by hot fluid to the wall is equal to the heat transferred by the wall to the cold fluid. The ratio of longitudinal conduction to the convection rate in the fluids is:

$$\frac{q_k}{q} = \frac{k_w A_k}{LC_h} \frac{T_{w,1} - T_{w,2}}{T_{h,1} - T_{h,2}} = \frac{k_w A_k}{LC_c} \frac{T_{w,1} - T_{w,2}}{T_{c,1} - T_{c,2}} . \quad (5.25)$$

The equation above gives the dimensionless parameters:

$$\lambda_h = \left(\frac{k_w A_k}{LC} \right)_h , \quad \lambda_c = \left(\frac{k_w A_k}{LC} \right)_c . \quad (5.26)$$

For a counterflow heat exchanger, the length parameters are interchangeable and if assumed that $L_h = L_c = L$ and the cross-sectional area remains the same, then:

$$\frac{\lambda_h}{\lambda_c} = \frac{C_c}{C_h} = \begin{cases} C^* & \text{for } C_c = C_{\min} \\ \frac{1}{C^*} & \text{for } C_h = C_{\max} \end{cases} . \quad (5.27)$$

The term λ is the longitudinal conduction parameter. The higher the value of λ , the higher is the conduction losses and the lower is the heat exchanger effectiveness. For a counter flow heat exchanger, the larger temperature gradient is obtained with the minimum heat capacity fluid, hence the longitudinal conduction parameter for the counterflow heat exchanger can be chosen as:

$$\lambda = \frac{k_w A_k}{LC_{\min}} . \quad (5.28)$$

If the factor $\Delta T_{max} = T_{h,i} - T_{c,i}$ is multiplied to the numerator and denominator, the factor λ can be interpreted as the ratio of longitudinal heat conduction rate for a heat exchanger, with $NTU = \infty$ and $C^* = 1$ to the thermodynamically maximum flow rate.

The effect of longitudinal heat conduction on the effectiveness of heat exchangers has been extensively studied by Kroeger in 1967 [31]. He found out that the deterioration of the effectiveness of a heat exchanger increases with increasing values of NTU , C^* and λ , and is

Methodology for Effectiveness Determination of 2K HX

the largest for $C^*=1$. A simpler expression for reduction in heat exchanger effectiveness due to the longitudinal wall conduction is:

$$\frac{\Delta\varepsilon}{\varepsilon} = \frac{\varepsilon_{\lambda=0} - \varepsilon_{\lambda \neq 0}}{\varepsilon_{\lambda=0}} = \frac{(NTU - \Phi)\lambda}{1 + NTU(1 + \lambda + \lambda\Phi)} \approx \lambda. \quad (5.29)$$

And the heat exchanger ineffectiveness for $C^* < 1$ is:

$$1 - \varepsilon = \frac{1 - C^*}{\psi \exp(r_1) - C^*}, \quad (5.30)$$

where

$$r_1 = \frac{(1 - C^*)NTU}{1 + \lambda \cdot NTU \cdot C^*}, \quad \psi = \frac{1 + \Upsilon\Psi^*}{1 - \Upsilon\Psi^*}, \quad \Psi^* = \left(\frac{\alpha}{1 + \alpha}\right)^{\frac{1}{2}} \frac{1 + \gamma}{\frac{1}{\alpha} - \gamma - \gamma^2},$$
$$\Upsilon = \frac{1 - C^*}{1 + C^*} \frac{1}{1 + \alpha}, \quad \alpha = \lambda \cdot NTU \cdot C^*. \quad (5.31)$$

From the studies conducted by Kroeger, it was summarized when $NTU > 10$ and $\lambda > 0.005$, the longitudinal conduction has significant effect on the effectiveness deterioration [11].

5.4.1. Longitudinal conduction effect on 2K HX_1

In the case of 2K HX_1, the LHe flows through the helical tube with the inner diameter being 4 mm, the outer diameter 6.5 mm and the flow length the same as the length of the tube which is 7 m. The thermo-physical properties of the fluids and material are as follows: average thermal conductivity of the OFC tube is 1050 W/mK, the average specific heat capacity of the LHe (minimum capacity fluid) is 3202 J/kg-K in the 4.4 K to 2.0 K range and the mass flow rate is taken as 3 g/s. The longitudinal conduction parameter is calculated as:

$$\lambda = \frac{k_w A_k}{LC_{\min}} = 0.000314 \quad (5.32)$$

As the longitudinal conduction parameter is less than 0.005 and the NTU is always < 10 for the 2K HX_1 (maximum obtained is 6), the effect of longitudinal wall conduction is ignored

in the helical tube. Also, since there is no connection between fins, the axial conduction in GHe flow stream is non-existent.

5.5. Thermal Conductivity of OFC

Thermal conductivity of copper varies with temperature in the range of 300 to 2 K. Until the liquid nitrogen temperature (77 K), the thermal conductivity variation is independent of residual resistivity ratio (RRR), but below this temperature thermal conductivity variation can be analyzed for different kinds of high purity copper, dependent on RRR.

RRR is defined as electrical resistivity at 293 K to electrical resistivity at 4 K. The 4 K resistivity of a copper sample is approximately equal to the temperature independent residual resistivity that results from the chemical and physical imperfections of the material. The resistivity at 293 K is intrinsic temperature dependent conductivity, resulting from thermal vibration of lattice. The material used to manufacture the helical tube and fins is OFC. RRR is an important factor for accurate prediction of thermal conductivity of OFC used in the heat exchanger for operating range of 2 - 4.4 K.

5.5.1. Experimental determination of RRR for a copper fin

An experimental setup used to measure RRR of superconducting materials, such as niobium (Nb) and NbTi, is used to measure RRR of OFC fins. The experimental setup mainly consists of a helium dewar, a copper block, a sourcemeter and a nanovoltmeter, as seen in Figure 5-6. The resistivity of the copper fin was measured using 4-wire method. Two wires to supply current and the other two to measure the voltage, as shown in Figure 5-6. The current was supplied via a Keithley 6221 current source, and the voltage was measured with Keithley 2182A nanovoltmeter. To measure the resistivity of the OFC copper fin at room temperature, ± 100 mA of current is provided through the fins and the voltage across the fin was measured. The obtained resistivity of OFC fin at room temperature was $1.7 \times 10^{-8} \Omega\text{m}$, and its resistance value is given in Table 5-1. Afterwards, the fin is placed inside a helium dewar and filled with LHe to measure the resistance at 4.2 K. Experimental results showed that

Methodology for Effectiveness Determination of 2K HX

RRR for the fin was approximately 210 and it will be similar for all other fins since they are all made from the same roll of OFC plate.

Table 5-1: Experimental results for RRR measurement of the 2K HX_1 fins

Current (A)	Temperature (K)	Resistance (Ohms)
0.1	293	2.3×10^{-5}
0.1	4.2	1.07×10^{-7}
RRR	210	

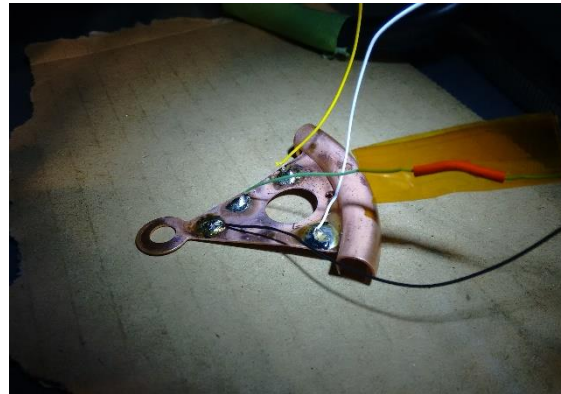


Figure 5-6: Experimental setup for RRR measurement at KEK (left) ; 4 wire RRR measurement on the OFC fin (right).

Methodology for Effectiveness Determination of 2K HX

To determine the thermal conductivity of OFC fins in the range of 2 - 4.4 K with RRR of 210, the thermal conductivity of RRR 100 and 300 for OFC is tabulated and the results are interpolated to get the thermal conductivity of OFC fins at RRR 210 [25], [32], as shown in Figure 5-7. Average thermal conductivity in the range 2 - 4.4 K is approximately 1050 W/mk. The thermal conductivity can vary drastically with heat treatment of the fins, it will rise with annealing. The realistic thermal conductivity might be higher than the current one, since the fins go through another round of heat treatment to be brazed on the helical tube of the 2K HX.

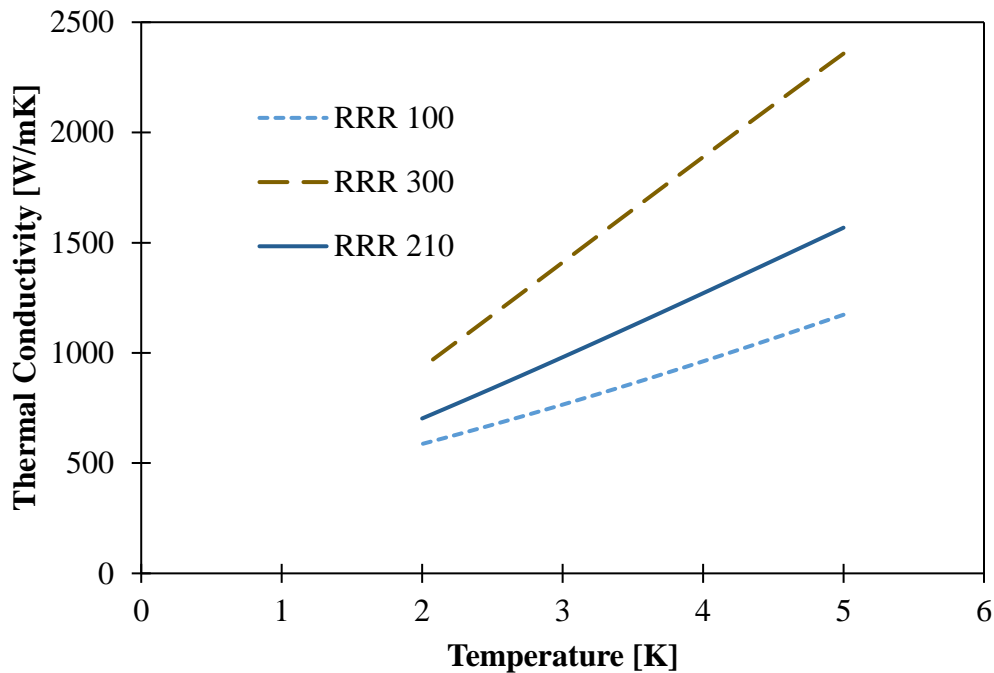


Figure 5-7: Thermal conductivity versus temperature for OFC.

5.6. Thermo-Physical Properties for Helium

The heat transfer rate between the fluids through the 2K HX is difficult to determine with conventional numerical methods, since the heat transfer coefficient of GHe (h_{GHe}) flowing

through the complicated geometry of stacked rows of fins is unknown. ANSYS CFX® will be employed to simulate and determine the heat transfer coefficient of the GHe flowing through 2K HX geometry. The details about the CAD model, domains, initial conditions, boundary conditions and the turbulence model employed for simulations are given in Tables 5-2 and 5-3 and Figure 5-9. For meshing, proximity and curvature criteria with tetrahedral meshes were applied to the 2K HX geometry. For the heat transfer coefficient of LHe (h_{LHe}) flowing in the helical tube, empirical relations are available from the texts.

5.6.1. Heat transfer coefficient for GHe

The GHe flow stream through the 2K HX_1 is complicated due to the presence of helical tube and fins arranged perpendicular to the flow stream. This arrangement causes incoming helium molecules to strike perpendicularly to the fins.

It is possible to determine the flow nature for the first helical loop with 6 fins, but as the helium flow past the 1st loop it develops a wake region behind the fins due to a sharp angle of attack (90 degrees). In the wake region after the 1st loop, the angle of attack would not be perpendicular to the next array of fins, since the helical pitch is not large enough to let the helium flow stream develop, and spatial repetition of fin arrangement causes the flow to take periodic structure. The periodic nature of the flow is determined and shown using computational flow dynamics (ANSYS CFX) in Section 6.5.3.

These kinds of geometries make it doubtful that the flow will be steady, since instabilities developed in the wake region cause unsteadiness, vortex generation and vortex shredding. The advantage of this arrangement is that it causes turbulence in the wake region at very low Reynolds number, which helps to enhance the heat transfer coefficient of the fluid. To study these kinds of flows, experimental and numerical studies have to be conducted. The disadvantage of this arrangement is its high pressure drop. Due to the periodic nature of the GHe flow stream, a theoretical calculation of the heat transfer coefficient for the flow regime may not be possible. The search for research journals regarding these kind flows bore no positive results.

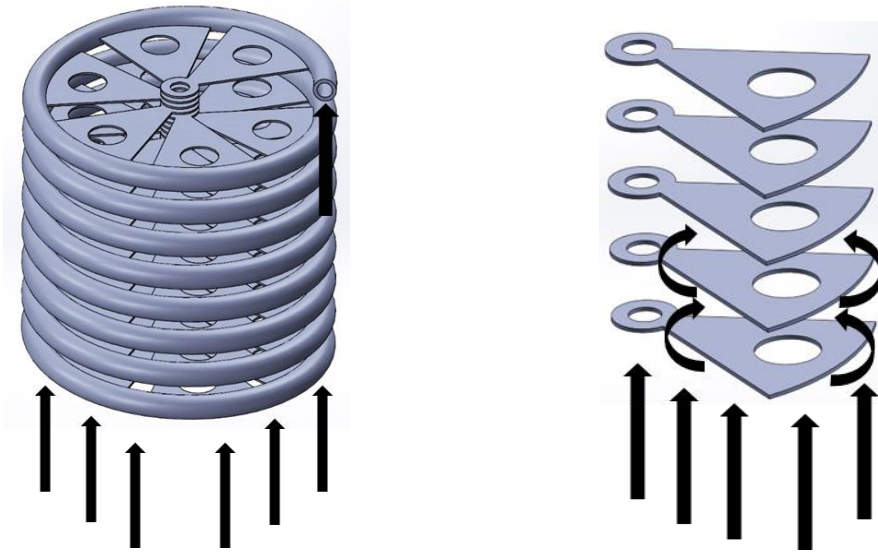


Figure 5-8: Gaseous helium flow through the stacked fins along helical tube.

The heat transfer coefficient of GHe in this study is determined by simulating 2.0 K GHe flowing through the 2K HX geometry, transferring heat to 2K HX's fins and the helical tube maintained at a constant temperature (4.4 K). The amount of heat transferred to the 2.0 K GHe provides its heat transfer coefficient with the aid of Newton's law of cooling and logarithmic mean temperature difference technique, as shown below through Equations 5.33 and 5.34:

$$\dot{Q}_{\text{GHe}} = \dot{m} [H_{c,o} - H_{c,i}] = (h_{\text{GHe}} \times A) [\Delta T_m] , \quad (5.33)$$

$$\Delta T_m = \frac{[(T_w - T_{c,o}) - (T_w - T_{c,i})]}{\ln \left[\frac{(T_w - T_{c,o})}{(T_w - T_{c,i})} \right]} . \quad (5.34)$$

where \dot{Q}_{GHe} is the amount of heat removed by the 2.0 K GHe, H is the enthalpy, subscripts c,o and c,i are for cold fluid (GHe) at outlet and inlet, respectively, A is the surface area of the 2K HX and h_{GHe} is the heat transfer coefficient for the GHe. Also, ΔT_m is the logarithmic mean temperature obtained from the outlet and inlet temperature of the cold fluid (GHe). No hot fluid (LHe) is flowed in the helical tube and the temperature of the wall is kept constant.

Methodology for Effectiveness Determination of 2K HX

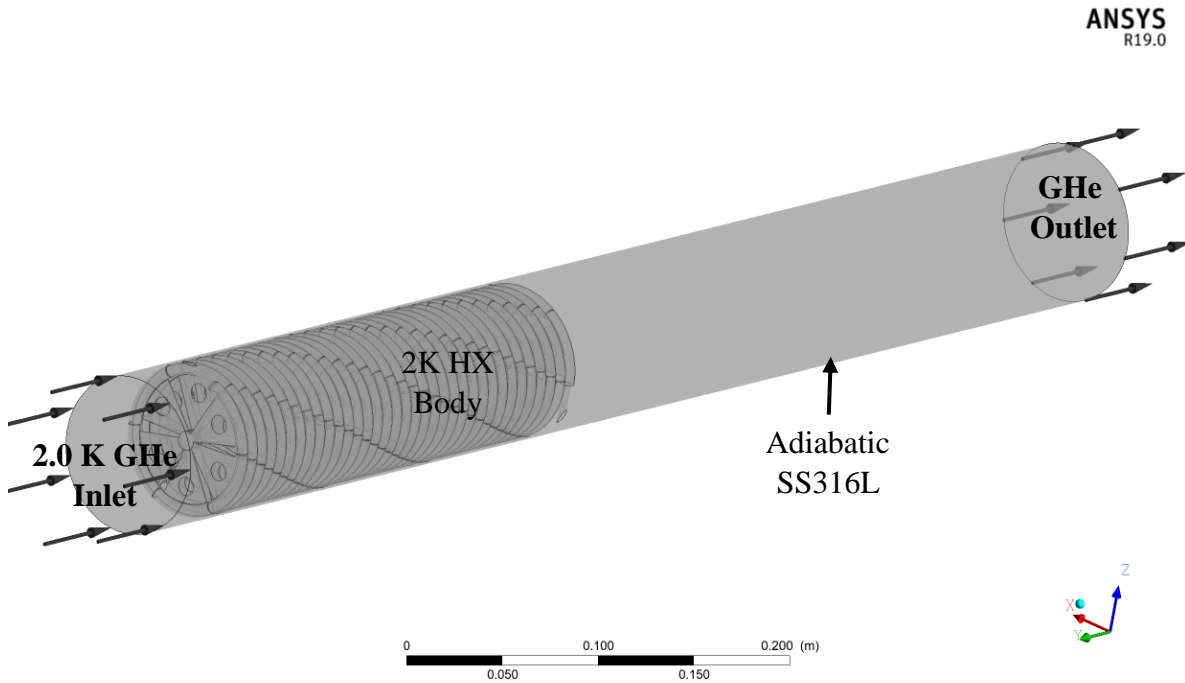


Figure 5-9: Example of the CFD model for the 2K HX.

Table 5-2: 2K HX domains and the initializing conditions

Domain	Fluid/ Solid	Temperature (K)	Turbulence Intensity (%)	Turbulence Model	Wall Function
GHe	GHe	2	4.4	k- ω SST	Automatic
OFC	OFC	4.4 K constant temperature with no fouling resistance			

Table 5-3: Boundary conditions for the 2K HX in ANSYS CFX®.

Boundary	Fluid/ Solid	Mass flow rate [gs ⁻¹]	Turbulence Intensity [%]	Static Temperature [K]	Total Pressure [kPa]
GHe Inlet	GHe	Up to 5	4.4	2	-
GHe Outlet	-	-	-	-	2.8
OFC	OFC	Interface between OFC copper and GHe			
Wall	SS316L	-	-	Adiabatic	-

5.6.2. Colburn and friction factor for the GHe flowing through 2K HX

Compact heat exchangers like the 2K HX_1 come in different types, configurations, etc. The heat transfer properties and the pressure drop through coiled finned tube and plate fin type heat exchangers have been studied extensively by Kays and London [33]. The dimensionless numbers that governs the correlations devised by Kays and London are the Stanton number (St), the Reynolds number (Re) and the Prandtl number (Pr):

$$\text{St} = \frac{h}{GC_p}, \quad \text{Re} = \frac{GD_h}{\mu}, \quad \text{Pr} = \frac{\mu C_p}{k}, \quad (5.35)$$

where ρ is the volume averaged density, μ is volume averaged dynamic viscosity, k is the volume averaged thermal conductivity, and G is the mass flux flowing through the 2K heat exchanger body, as shown in Figure 5-10:

$$\text{Mass Flux, } G = \frac{\dot{m}}{A_{fr}}, \quad \text{Hydraulic Diameter, } D_h = 4 \frac{L \times A_{fr}}{A_t}. \quad (5.36)$$

Here, L is the flow length of the heat exchanger measured from leading edge of the first helix to the leading edge of helix that would follow the last helix, A_{fr} is the minimum free flow area for the fluid, A_t is the total surface area with which fluid interacts. The free flow area (A_{fr}) in this case is determined by considering one helical loop projecting its area on a plane perpendicular to the fluid flow. The hydraulic diameter is determined by the swept volume of the GHe through the finned geometry, $L \times A_{fr}$, and the wetted area, A_t , same as the total surface area with which the fluid interacts. The hydraulic diameter for this kind of heat exchanger geometry came out to be approximately 0.003 m.

Methodology for Effectiveness Determination of 2K HX

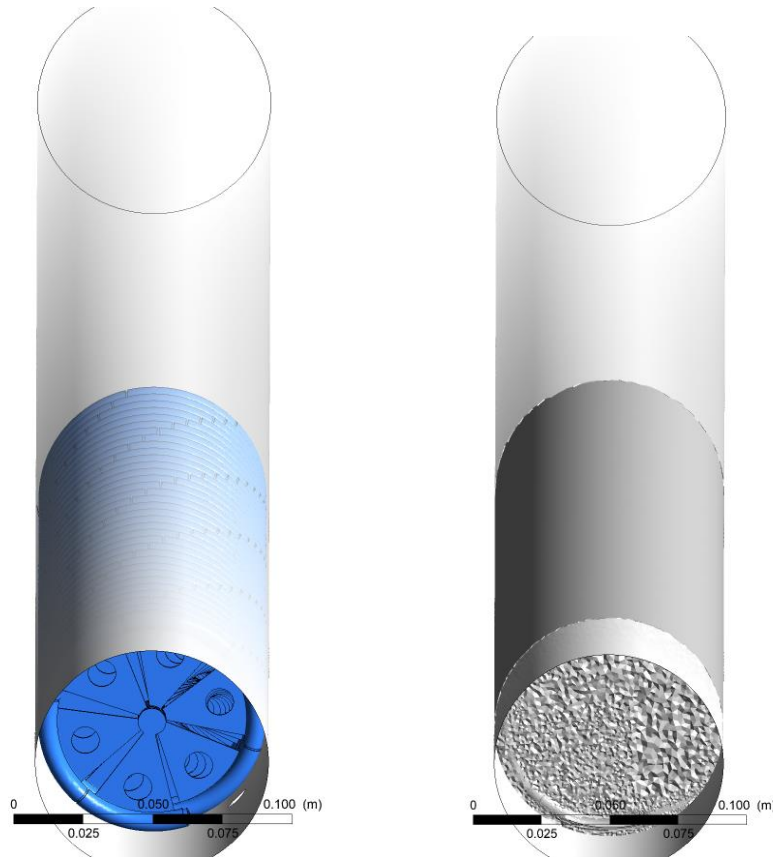


Figure 5-10: a) 2K heat exchanger geometry in a SS316L shell (left), b) Volume surrounding the 2K Heat exchanger body (right).

The Colburn factor is a normalizing methodology for heat transfer coefficient of any fluid flowing through a compact heat exchanger. It was used extensively by Kays and London to characterize many types of compact heat exchangers, such as plate fin, finned tube heat exchangers etc. The approximation of the Prandtl number to the power $2/3$ has a good approximation over a moderate range for all gases. From the experience gained by Kays and London, the power $2/3$ is a reasonable compromise and allows the presentation of the complete characteristics of a surface on a single graph [33]. The Colburn factor for a compact heat exchanger geometry is:

$$\text{Colburn Factor, } j = \text{St} \times \text{Pr}^{\left(\frac{2}{3}\right)}. \quad (5.37)$$

Friction factor for a fluid flowing over compact geometry

The friction factor is defined on the basis of an equivalent shear force in the flow direction per unit heat transfer (or friction) area. The pressure drop for external flows can be expressed in the form presented by Kays and London. In the expression given below, the first term shows the effect of flow acceleration, and the second term is for the core friction through the heat exchanger geometry [30], [33]:

$$\text{Pressure Drop, } \Delta p = \frac{G^2}{2\rho_i} \left[(1 + \sigma^2) \left(\frac{\rho_i}{\rho_o} - 1 \right) + f \frac{A_t}{A_{fr}} \frac{\rho_i}{\rho} \right]. \quad (5.38)$$

Here ρ_i is the density of the fluids at the inlet, ρ_o is the density at the outlet, ρ is the average density, f is the friction coefficient and $\sigma = A_{fr}/A_{ff}$ is the ratio of free flow area to frontal area of the fluids' entry to the heat exchanger.

5.6.3. Heat transfer coefficient and pressure drop for LHe

Helical tubes in heat exchangers reduce the volume of space occupied by a long tube and increases the flow length. In contrast with fluid flow over the stack of perpendicular fins, fluid flow through a helical tube had been researched comprehensively.

Nusselt number for a fully developed fluid flow in a helical tube has been researched thoroughly by researchers worldwide. From the Schmidt relation, it has the largest application range for the Reynolds number $2 \times 10^4 < Re < 1.5 \times 10^5$ and for $84 > R/a > 5$. This was developed using water and air in coils under constant wall temperature conditions [30], [34]:

$$\text{Nu}_{\text{LHe}} = \frac{h_{\text{LHe}} D_h}{k} = \left\{ 1 + 3.6 \left[1 - \frac{a}{R} \right] \left[\frac{a}{R} \right]^{0.8} \right\} \text{Nu}_s, \\ \text{and } \text{Nu}_s = 0.023 \times \text{Re}^{0.8} \times \text{Pr}^{0.3}, \quad (5.39)$$

where Nu_s is the Nusselt number for LHe flowing in a straight tube, D_h is the hydraulic diameter, Re the Reynolds number, Pr the Prandtl number and k the thermal conductivity of

Methodology for Effectiveness Determination of 2K HX

the fluid. The subscript, s, is for straight tube, a, is the radius of the tube and R is the curvature radius of the helical tube.

Pressure drop in a helical tube

To determine the pressure drop through a helical tube, many theoretical and empirical relations are available. C.M. White experimentally determined the friction factor for fluids flowing through helical tube. Srinivasan et. al and H. Ito refined available experimental data to form empirical relations for laminar, mixed and turbulent regions. The friction factor for turbulent flow in helical tube from Srinivasan et al is given by [34], [35]:

$$\text{Friction factor } f_c = 1.084 \left[\text{Re} \sqrt{\left(\frac{R}{a}\right)} \right]^{-0.2} . \quad (5.40)$$

Once the friction factor is known, then frictional pressure drop in a helical tube can be generally expressed as:

$$\text{Pressure drop } \Delta P = 4f_c \frac{L}{D_h} \frac{\rho v^2}{2} . \quad (5.41)$$

Here L is the length of the helical tube when it is straightened.

Chapter 6. EXPERIMENTAL AND NUMERICAL INVESTIGATION OF THE 2K HX_1

6.1. Heat Exchanger Test Stand

Test stands to measure the performance of a 2K heat exchanger for flow rates up to 4 g/s are rare. At CERN in early 2000's, a test stand was designed to measure the performance of the 2K heat exchangers at 4.5 g/s for the LHC cryogenic system [36]. At KEK, a 2K heat exchanger test stand was designed and manufactured to test 2K heat exchangers (2K HX) for their efficiency on reducing the LHe temperature from 4.4 K to sub cooled > 2.2 K via incoming 2 K GHe stream, from a tank storing superfluid helium at 2.0 K.

The test stand's 2K refrigerator cold box encloses a He I storage tank, the 2K HX, a He II storage tank and a JT valve for superfluid helium production. The He I storage tank stores the LHe at 4.21 K or above, and the He II tank stores superfluid helium at < 2.1 K. A 2K HX between both storage tanks subcool He I to > 2.2 K, using the sensible heat capacity of the outgoing 2.0 K GHe from the He II tank. The JT valve after the 2K HX reduces the subcooled He I pressure from 125 kPa to approximately 3.13 kPa. The JT valve maintains continuous production and the level of superfluid helium in the He II tank, hence producing similar mass flow rates through the 2K HX. This eliminates the need to measure the He I mass flow rate at low temperatures. The sub atmospheric pressure in the He II tank is maintained by 8 rotary vacuum pumps (with boosters) with a capacity of 95 W at 3.13 kPa inlet pressure (for STF). The components listed above are protected from excess heat from the surroundings by two stages of thermal shields. The thermal shields eliminate the heat from the surroundings by absorbing and dissipating the excess heat to the cryogenics that are cooling them. The first stage of the thermal shield operates at 90 K with the help of liquid nitrogen, and the second stage is operated at 10 K cooled with LHe. High thermal conductive materials like aluminum (Al6000) are used to construct the thermal shields, and the material for the construction of the test setup was stainless steel SS316L.

All the components are wrapped with an appropriate number of multi-layer insulations (MLI) to reduce the radiation heat load from the surroundings, as it is a dominating source of thermal load on the components at high vacuum conditions. The number of MLI layers are 30-35 for 90 K thermal shield and 10-15 for the 10 K thermal shield, storage tanks and the 2K heat exchanger. High vacuum conditions of the order of 10^{-4} Pa inside the test stand are maintained via turbo-molecular vacuum pumps initially, and then the cryo-pumping effect of LHe in storage tanks reduces the pressure further.

6.1.1. Flow control

The flow of cryogenics through the thermal shields, 2K heat exchangers and bypass lines is maintained by control valves placed at specific positions in the heat exchanger test stand, as shown in Figure 6-2. The control valve (CV105) controls the flow of liquid nitrogen through the 90 K thermal shield. It is operated manually to cool down the thermal shield in approximately 4 hours. The control valve (CV101) is a bypass valve to transfer LHe from He I tank to the He II tank for the initial cooldown and for the filling of He II tank. The control valve (CV102) controls the flow of LHe through the 10 K thermal shield to the He I tank. When the shield is cooled down to approximately 15 K, the level in the He I tank starts rising. The two stages of thermal shielding allow almost nonexistent thermal loads to the LHe stored in the tanks. The control valve (CV103) is a JT valve placed to produce superfluid helium by reducing the pressure of incoming subcooled LHe from the 2K heat exchanger, at approximately 101 kPa to 3.13 kPa. It also maintains the superfluid helium level by controlling the flow rate of incoming sub cooled LHe. The Figure 6-1 shows the tip of the JT valve. The CV20 valve throttles the flow to the rotary vane pumps to maintain 3.13 kPa vapor pressure on the superfluid helium in the He II tank, since the pumping capacity of a rotary vane pump always remain constant at a certain pressure and temperature condition.

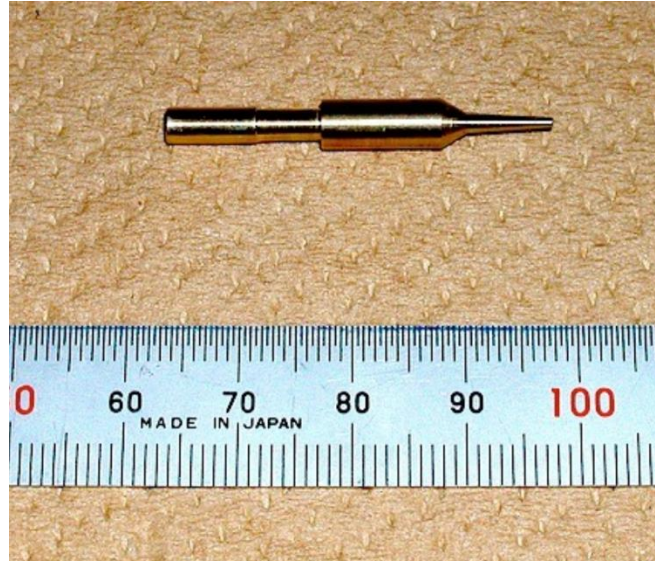


Figure 6-1: Joule-Thomson valve tip for level and pressure control.

6.1.2. Temperature and pressure sensors

The heat exchanger test stand is equipped with temperature and pressure sensors to monitor the thermo-physical properties of cryogenics flowing through the 2K HX, thermal shields, storage tanks and cryogenic transferlines, as shown in Figure 6-2. Cernox® temperature sensors (Lakeshore™) are employed for accurate measurement of temperature above 1.3 K and the PtCo temperature sensor (Chino®) to monitor the He I tank and 10 K thermal shield temperature. T-type thermocouple is used to monitor the 90 K thermal shield temperature. The temperature sensors, TI101 and TI106, measure the 2K HX's inlet and outlet temperatures of LHe flowing from the He I tank to the He II tank, respectively. The sensors X51202 and TI205 measure the 2K HX's inlet and outlet temperatures of outgoing GHe from the He II tank, respectively. Cernox® sensors TI103 and TI104 will be used to monitor the inlet and outlet temperature of subcooled LHe before and after the JT expansion. The calibration curves for the Cernox® sensors are given in Appendices. The sensors for the GHe are installed in a $\Phi 4$ mm SS316L thermowell pipe going through the GHe return piping. A Cernox® DT670 silicon diode sensor at the bottom of He II tank monitors the temperature of superfluid helium. The pressure sensors are: PT108, PT102, PT105 and PT106, and they

monitor the fluid pressure conditions in the pipeline. PT108 is a full range Baratron® pressure sensor to monitor the He I tank pressure and PT102 is a full range Kyowa® pressure sensor to monitor the subcooled He I pressure between the 2K HX and the JT valve. Baratron® fine range pressure sensors PT105 and PT106 monitors the inlet and outlet pressure of sub atmospheric GHe flowing through the 2K HX, hence providing the amount GHe ΔP through the 2K HX.

The AMI® liquid helium level sensors (LM101 and LM102) monitor the level of He I and He II tanks, respectively. A heater (100W) is placed at the bottom of the He II tank to vary the flow rate of the GHe through the 2K HX, hence to measure the performance of the 2K HX at different flow rates. The helium gas pumping system at the STF facility has the capability to handle 95 W of thermal load at 2.0 K or 3.13 kPa inlet pressure. A kW range heater warms the outgoing GHe from the He I tank to room temperatures during the initial cool down period and the steady state operation.

6.1.3. Instrumentation

The voltage readings from the temperature, pressure and level sensors are recorded with Keithley DMM6500 and Keithley DMM2000. Each multimeter has 10 isolated channels to monitor the sensor voltages. A channel delay of 100 ms between each channel is introduced to eliminate noisy operation of relays effecting the sensors voltages. Cernox® sensors are connected in series with ADCMT 6243 DC current sourcemeter to provide excitation current of 1 μA with limiting voltage of 110 V. A battery powered Lakeshore Current source (10 μA) powers the Cernox® DT670 silicone diode temperature sensor in the He II tank. Lakeshore's 120 DC sourcemeter provides 1 mA excitation current to the PtCo sensors connected in series. Yokogawa sourcemeter is used to provide excitation voltage of 1 V for the Kyowa sensor. AMI LHe level sensors monitor the level of LHe in the He I and the He II tank. Kikusui 750W power supply is used to provide controlled thermal loads to the superfluid helium in the He II tank during experiments. Yokogawa PID controllers are used to control the actuators for the valves' opening and closing. These PID controllers have a fast response time and can control the actuators instantaneously, producing a very fine control.

Experimental and Numerical Investigation of the 2K HX 1

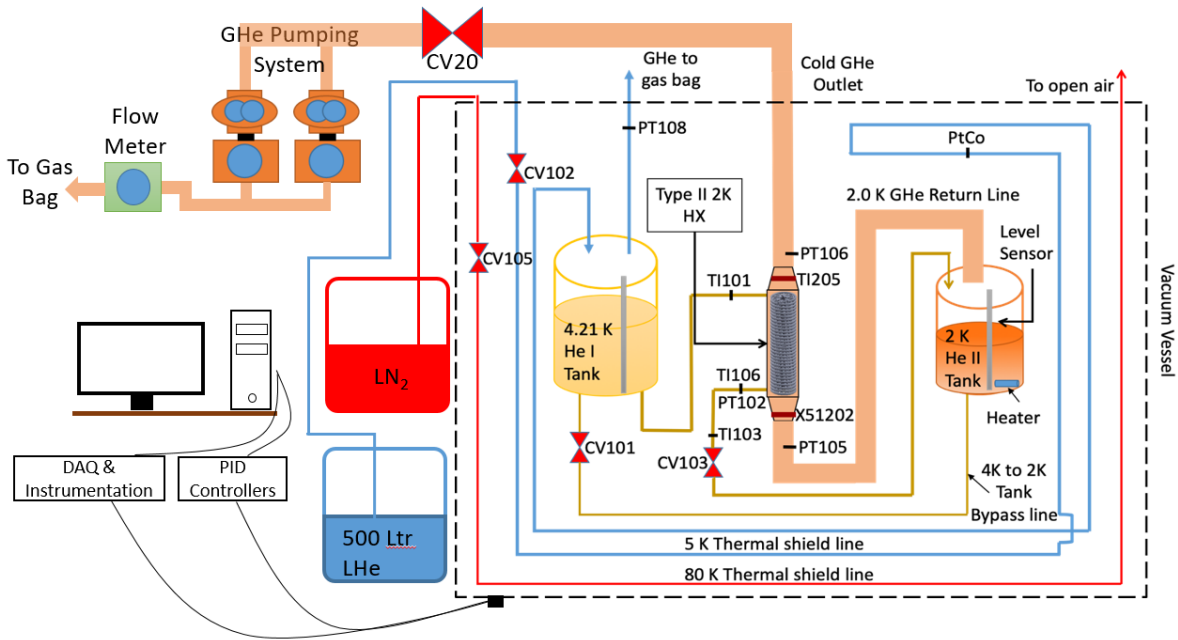


Figure 6-2: Schematic diagram of the 2K heat exchanger test stand.

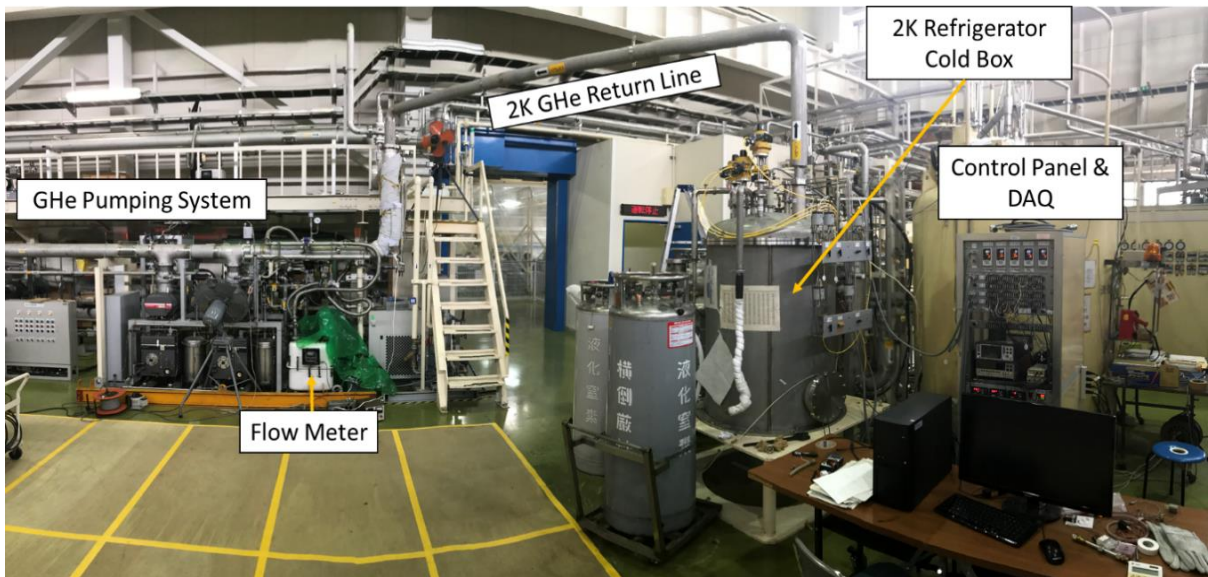


Figure 6-3: Complete layout for the 2K heat exchanger test stand.



Figure 6-4: 2K Cold box for the heat exchanger test stand.

6.2. Studies Conducted to Improve the Heat Exchanger Test Stand

Initially, the heat exchanger test stand was designed and manufactured in late 2000's to test the 2K HXs at KEK, but due to budgetary and time constraints it was never operated. The heat exchanger test stand as seen in Figure 6-4 was initially made up of two cold boxes connected with a multi-transfer cryogenic lines. One cold box would house the He I tank and the 2K HX and the other one housing the He II tank and a JT valve. Later on, the test stand was combined into one cold box by halving the size of the He II tank and placing it with the JT valve in the same cold box as the one housing the He I tank and a 2K HX. This helped to reduce the cooldown time from 300 K to 100 K from 7 hours to 4 hours. Also, the liquid nitrogen and LHe consumption for the cooldown was halved. When the heat exchanger test stand was operated initially, some issues were encountered as listed below,

1. Thermometry for cold GHe
2. Thermal acoustic oscillations in pressure sensor
3. Data acquisition system

6.2.1. Thermometry

The methodology that was utilized to install the temperature sensors on the heat exchanger test stand, introduced errors in the temperature sensing element (Cernox® sensor) for the GHe. The sensor would never show temperatures below 15 K while measuring the temperature of the GHe, but will show accurate temperature when surrounded with LHe. Initially, it was thought that the thermal anchoring methodology might be an issue but after properly anchoring the sensors, still no improvement was observed. Hence, finally it was concluded that the ICF 34 flange which were used to insert the temperature sensors in the fluid stream acted as a thermal mass, and would take hours to cool down with GHe before showing accurate temperatures. The same sensors were accurately showing LHe temperatures as the latent heat of LHe cooled the mass at a much faster rate than the GHe. To improve the installation methodology, thermowell technique described in various literatures were tested to reduce the cooldown time of the temperature sensors and to improve their response time [37], [38]. A small test stand was manufactured which could hold approximately 3 litres of LHe. Above the liquid level, ports for various sensing methodology were created, as shown in Figure 6-5:

- *Thermowell*: A Cernox® sensor placed in a $\Phi 4$ mm SS304 tube which goes through the flow stream.
- *ICF flange with thermowell (original method)*: Sensor in a 4 mm SS304 tube welded to an ICF flange and its tip inserted into the stream.
- *Saddle method*: Sensor inserted inside a copper block which is brazed to the SS304 tube carrying cold GHe.

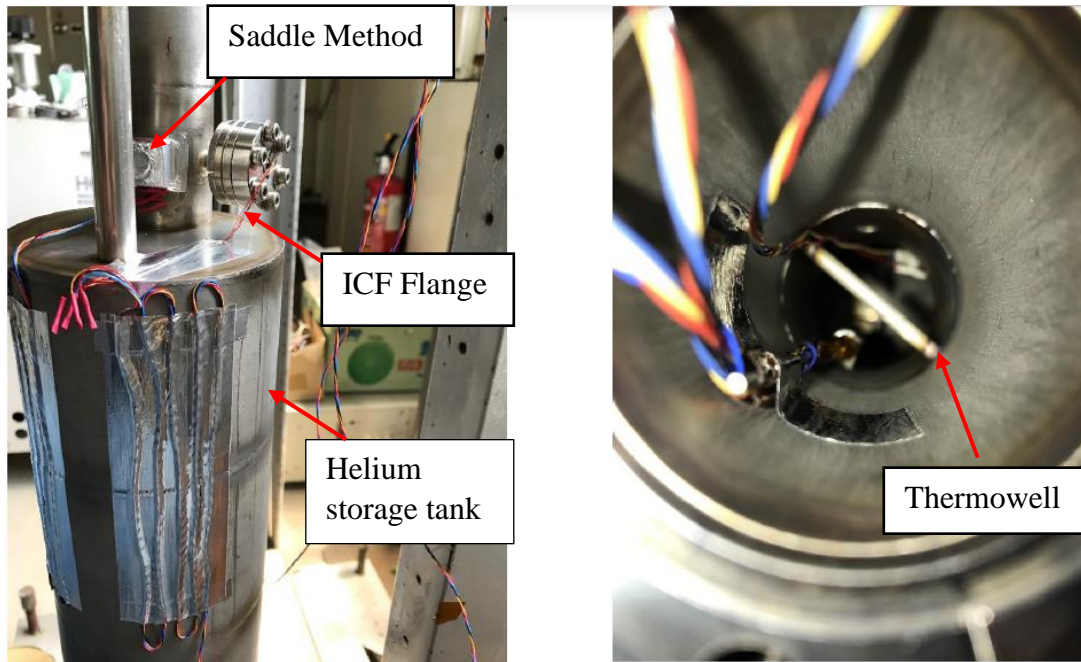


Figure 6-5: Various sensor attaching methodology outside the pipe (left), and view from inside pipe showing the thermowell technique (right).

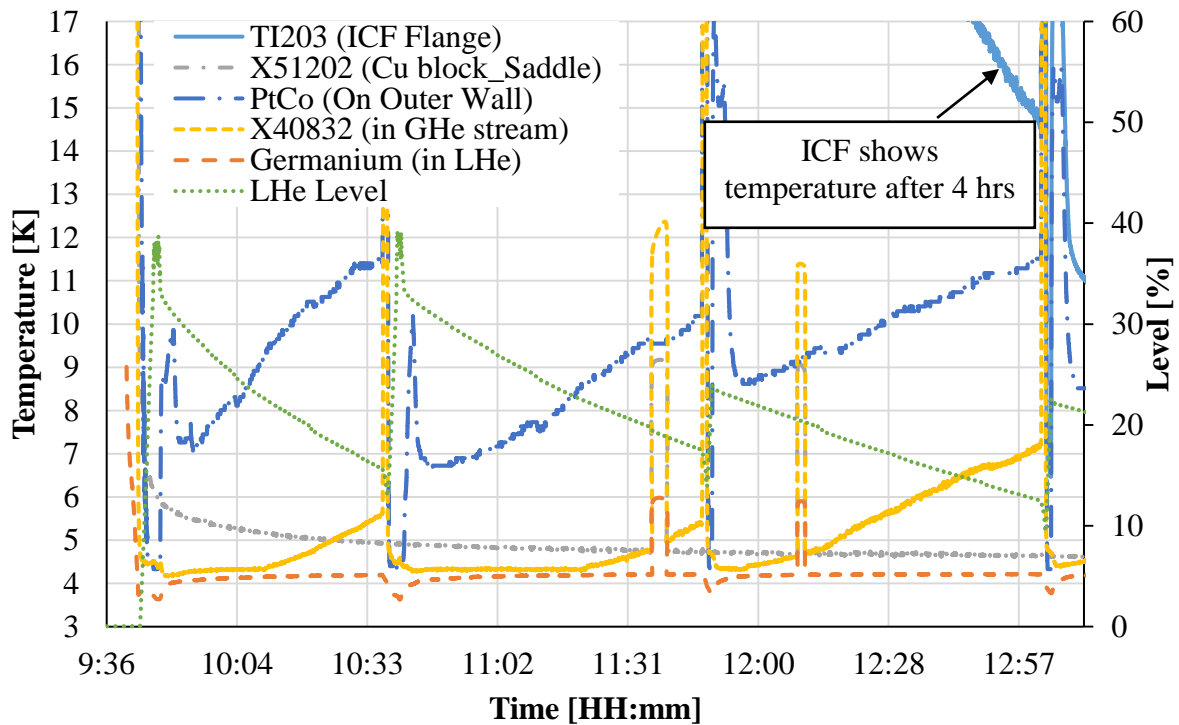


Figure 6-6: The behavior of various attached sensors during refilling of LHe.

Experimental and Numerical Investigation of the 2K HX 1

From the experiments shown in Figure 6-6, it was observed that it took 4-5 hours to cool the ICF flange mass with cold GHe vapors to under 15 K. In this experiment, helium was maintained at 10 Pa absolute pressure outside the tank to cool the flange via natural convection, from the coldness gained from LHe stored inside the tank, hence many refills were required to keep cooling the flange from inside and outside. The saddle method also took some time to cooldown as the heat capacity of copper is quite high, and to cool it with helium vapor it took some time but that was only a few minutes, compared to hours for the ICF flange method.

Many experiments were also performed to study the behavior of the sensors attached via different methodologies, an example of it is given in Figure 6-7. The main takeaway from the results were: the thermowell methodology showed the closest temperature to the barechip sensor in the GHe stream, while the small mass of thermowell compared to both saddle and ICF flange methodology, attributed to its faster response time.

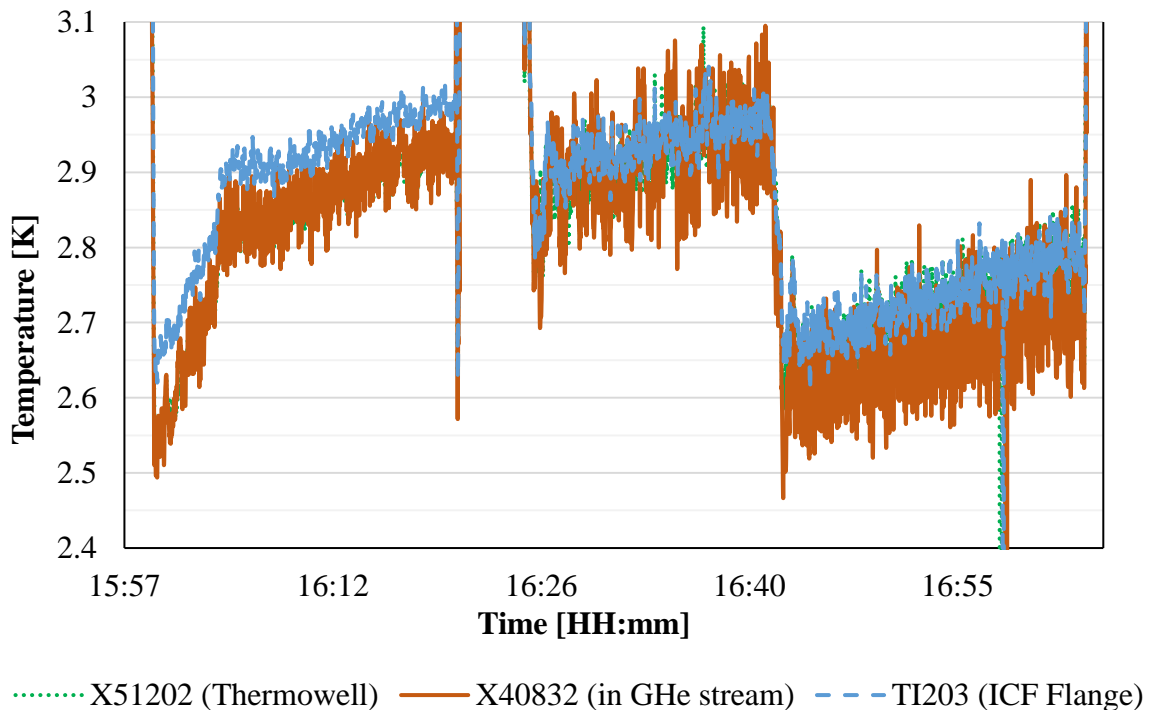


Figure 6-7: Comparison of different sensor attaching methodologies at low temperatures.

6.2.2. Thermo-acoustic oscillations in pressure sensing tubes

After improving the sensor measuring methodology during 1st successful experiment, it was observed that the two sensors measuring the LHe pressure showed thermo-acoustic oscillations, at the inlet and outlet of the 2K HX. This introduced an excess heat load and flow instability in the LHe flowing through the 2K HX. There were no oscillations observed in the pressure sensing tubes measuring the sub-atmospheric GHe pressure. The temperature gradient was in the order of 80 - 100 in a 1/8th inch tube, with its one end connected to the vacuum vessel at 300 K and the other end to the LHe at < 4.2 K. The high temperature gradient and density variation created ideal conditions for the thermo-acoustic oscillation to occur, as described by N. Rott [39], [40]. To avoid thermo-acoustic oscillations, H. Luck [41] described methodologies such as passive dampeners (capillaries, orifices and reservoir volume) and active dampeners (valve with a dynamic oscillator or dampener).

Another method is to use a pressure sensor that can work at low temperatures to reduce the thermal gradient. A Kyowa® PHS-B pressure sensor that could operate until liquid nitrogen temperatures (80 K) was bought and tested for its performance in LHe temperatures, which can be seen in Figure 6-8. This sensor doesn't require any calibration in the temperature range of 80 K – 300 K, but to test its behavior until LHe temperatures, it was dipped in LHe and the pressure was varied. The tests showed that this sensor gives erratic pressure readings below 6 K, but was fairly accurate above it. This sensor was calibrated from 30 kPa to 125 kPa, with its temperature varied from 4 K to 300 K, as shown in Figure 6-9. Its calibration curves were formed and the sensor was attached to the 10 K thermal shield with an aluminum block and a PtCo temperature sensor to monitor its body temperature, as seen in Figure 6-8. As the thermal shield operating temperature is higher than 10 K, the data obtained from the sensor is reliable, and the thermal gradient is less than 5 for the pressure sensing tube. The pressure sensor line from the 2K HX's LHe outlet was connected to the Kyowa® sensor to measure the He I pressure at the outlet of 2K HX.

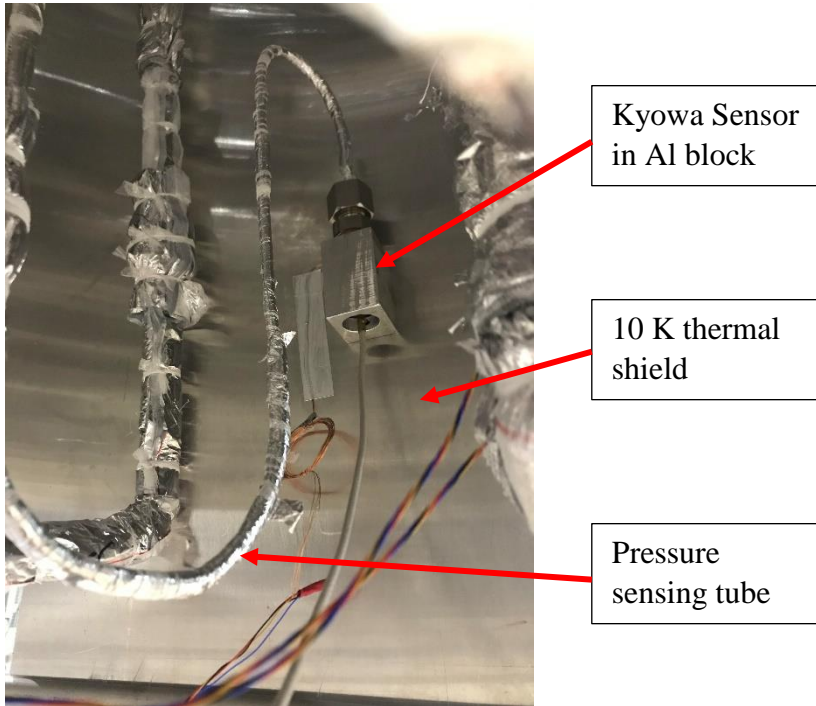


Figure 6-8: Kyowa sensor in an Al block attached on the 10 K thermal shield.

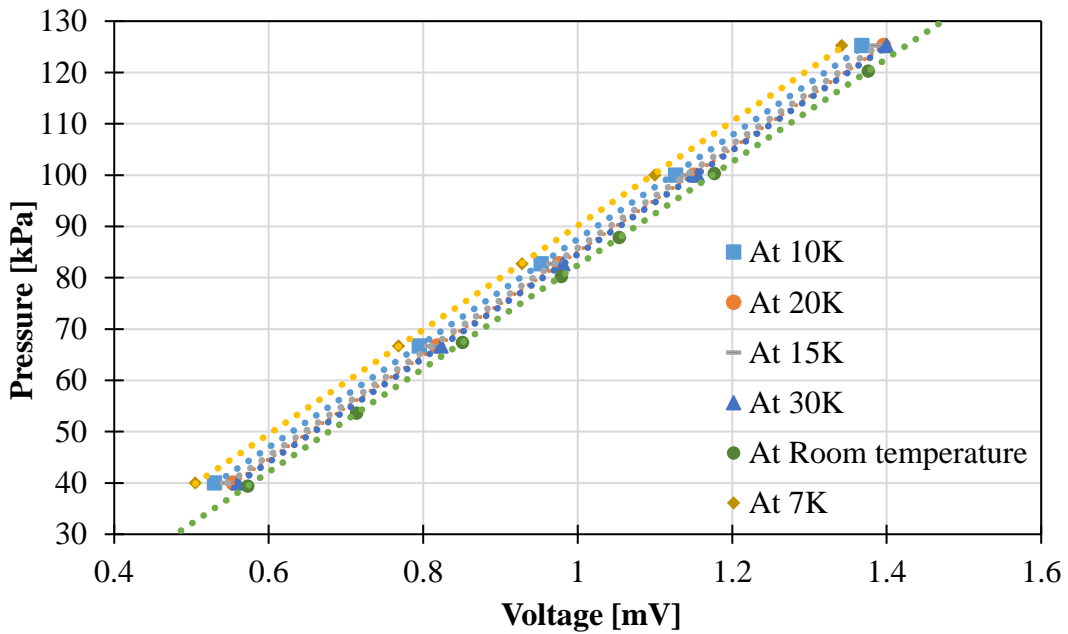


Figure 6-9: Calibration curve for the Kyowa® PHS-B sensor from 7 to 300 K.

6.3. Experimental Procedure

The experimental procedure to run the test setup is:

1. Preparation of the test stand, data acquisition system and control system.
2. Preparation of adequate amount of LHe in two 500 Ltr Dewars and liquid nitrogen.
3. Checking for leaks in the tubes and storage tanks using helium leak detector.
4. Purging the air inside the tanks, 2K HX and cryolines with helium and making sure the vacuum level in the test stand is ideal ($< 10^{-2}$ Pa).
5. Supplying liquid nitrogen to the 90 K thermal shield for the initial cool down of the test setup to achieve steady state condition (CV105 – Manual).
6. It takes approximately 4-5 hours to cool down the 90 K thermal shield from 300 K to 100 K.
7. The 10 K thermal shield is cooled down using the LHe from the 500 L Dewar. Manually operated CV102 controls the supply of LHe to the thermal shield during cooldown. The bypass valve is opened to allow the LHe to pass through the He II tank and the 2K HX for cooling the whole system.
8. After the cooldown, CV102 is opened more to fill the storage tanks and the system is kept overnight to stabilize and achieve steady state conditions.
9. Overnight, the 10 K thermal shield warms up to approximately 78 K and the 90 K thermal shield to approximately 150 K.
10. The next day these shields are cooled again, taking approximately 2 hours to complete cooldown and both tanks are filled to prepare for the experiment.
11. The rotary vacuum pumps are turned on to reduce the vapor pressure on the LHe at 4.2 K @ 100 kPa in the He II tank, in order to get the required 2.0 K temperature @ 3.13 kPa vapor pressure.

12. As the steady state is achieved in both tanks, the control valve CV103 is opened with the PID controller to allow the 4.21 K LHe to flow through the 2K HX via the JT valve to the He II tank to maintain the level of superfluid helium.
13. After the initial reading at 6 W of thermal load to achieve steady state operation, the heater power in the He II tank is increased in steps to a maximum power of 80 W.
14. Keithley DMMs record the voltage readings from all the sensors continuously.
15. Data is sorted in post processing for analysis.

6.4. Results and Discussion

The heat exchanger test stand provides the temperatures and pressures of both LHe and GHe flowing through the 2K HX. With the known inlet and outlet conditions, it is possible to determine the enthalpy of the fluids. Theoretically, the amount of enthalpy given by the hot LHe to the 2K HX should be equal to the amount of enthalpy extracted by the cold GHe, but due to heat inleak from the surrounding thermal shields, there is bound to be some error. The enthalpy balance error between fluids was confirmed to be around 2% at 3 g/s, with the GHe removing excess heat from the surroundings. The amount of heat transferred by fluids can be determined from the relation given below:

$$\dot{Q}_{\text{LHe}} = \dot{m} [H_{h,i} - h_{h,o}] \text{ and } \dot{Q}_{\text{GHe}} = \dot{m} [H_{c,o} - H_{c,i}] . \quad (6.1)$$

Here, \dot{Q}_{LHe} is the heat transferred by LHe to the 2K HX, \dot{Q}_{GHe} is the heat removed by the GHe from the 2K HX body and from the surroundings, $H_{h,i}$ and $H_{h,o}$ are the enthalpies of LHe at the inlet and outlet of the 2K HX, respectively, $H_{c,i}$ and $H_{c,o}$ are the enthalpies of GHe at the inlet and outlet of the 2K HX, respectively. The maximum possible heat transfer, \dot{Q}_{max} , between fluids is expressed as:

$$\dot{Q}_{\text{max}} = \dot{m} [H_{h,i} - H_{h@c,i}] , \quad (6.2)$$

Experimental and Numerical Investigation of the 2K HX 1

where $H_{h@c,i}$, is the enthalpy of the hot fluid at the cold fluid inlet temperature, under the hot fluid pressure condition. Then, the effectiveness of a heat exchanger, ε , is determined as:

$$\varepsilon = \frac{\dot{Q}_{LHe \text{ or } GHe}}{\dot{Q}_{\max}} . \quad (6.3)$$

The flash loss (dryness) during the JT expansion can be obtained by:

$$\frac{\dot{m}_v}{\dot{m}} = \frac{[H_{h,o} - H_{h@ \text{sat.}}]}{H_{fg}} . \quad (6.4)$$

where $H_{h@ \text{sat.}}$ and H_{fg} are the enthalpy and the latent heat of the He II at saturation pressure and temperature, respectively. The flash loss, \dot{m}_v/\dot{m} , indicates the fraction of vapour produced during the JT expansion.

6.4.1. 2K HX_1 experimental result

The 2K HX_1 was assembled in the heat exchanger test stand to measure its performance until 3 g/s flow rate. During the experiment, the 90 K thermal shield was steadily operated at 110 K, and the 10 K thermal shield remained at 11 K. The maximum mass flow instability generated by the level control on the 2.0 K superfluid helium through the 2K HX was approximately 0.013 g/s. The pressure control on the superfluid helium in the He II tank was performed with the precision of ± 7 Pa at maximum possible flow rate. The heater inside the He II tank was operated up to 60 W of power, as the known GHe pumping system capacity at that time was 70 W (3 g/s) of thermal load at 3.13 kPa. Multiple experiments were conducted to check the reproducibility of the results and to obtain the right combination of PID parameters for the JT valve and CV20 valve, to control the level and pressure of the superfluid helium in the He II tank.

Experimental and Numerical Investigation of the 2K HX 1

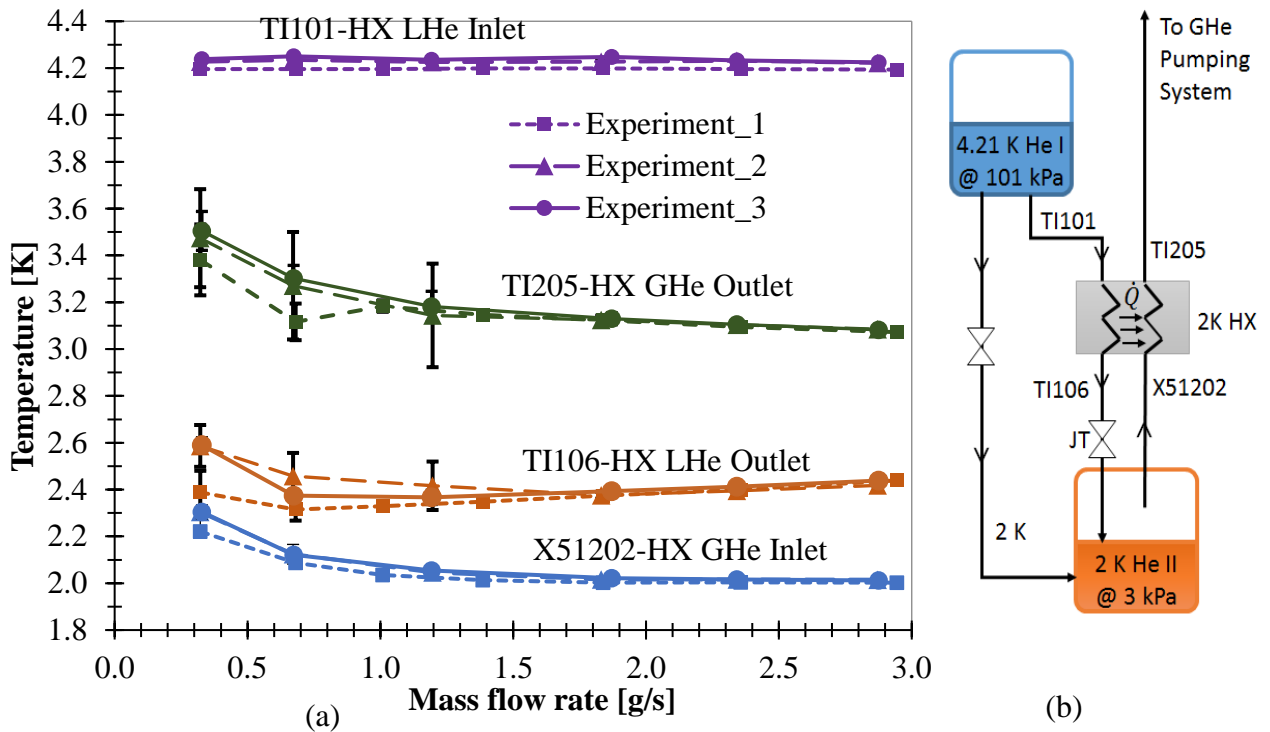


Figure 6-10: (a) Temperature data with respect to mass flow rate for the 2K HX_1, (b) Schematic view of the fluid flow through the heat exchanger test stand.

The positions of the temperature sensors are shown in Figure 6-10(b). The temperature data obtained from the experiments plotted in Figure 6-10(a) is from the operational mode of the 2K HX_1 (level control in the He II tank), with the mass flow rate varied from 0 to 3 g/s (70 W). From Figure 6-10(a), it is observed that the inlet temperature of LHe (TI101) to the 2K HX remains constant throughout the experiment, at around 4.2 K. The inlet temperature of the GHe (X51202) is initially > 2.0 K (below 1 g/s), due to the excess heat from the level sensor wire (above He II level) in the He II tank, heating the outgoing 2.0 K gas (see Figure 6-2), before it reaches the 2K HX_1. In the case of mass flow rate > 1 g/s, the GHe inlet temperature reduces and remains constant at 2.0 K, and the LHe outlet temperature (TI106) starts to rise with consequent increments in flow rates (1 to 3 g/s). The GHe outlet temperature (TI205) of the 2K HX keeps on reducing, as its mass flow rate keeps on increasing [18].

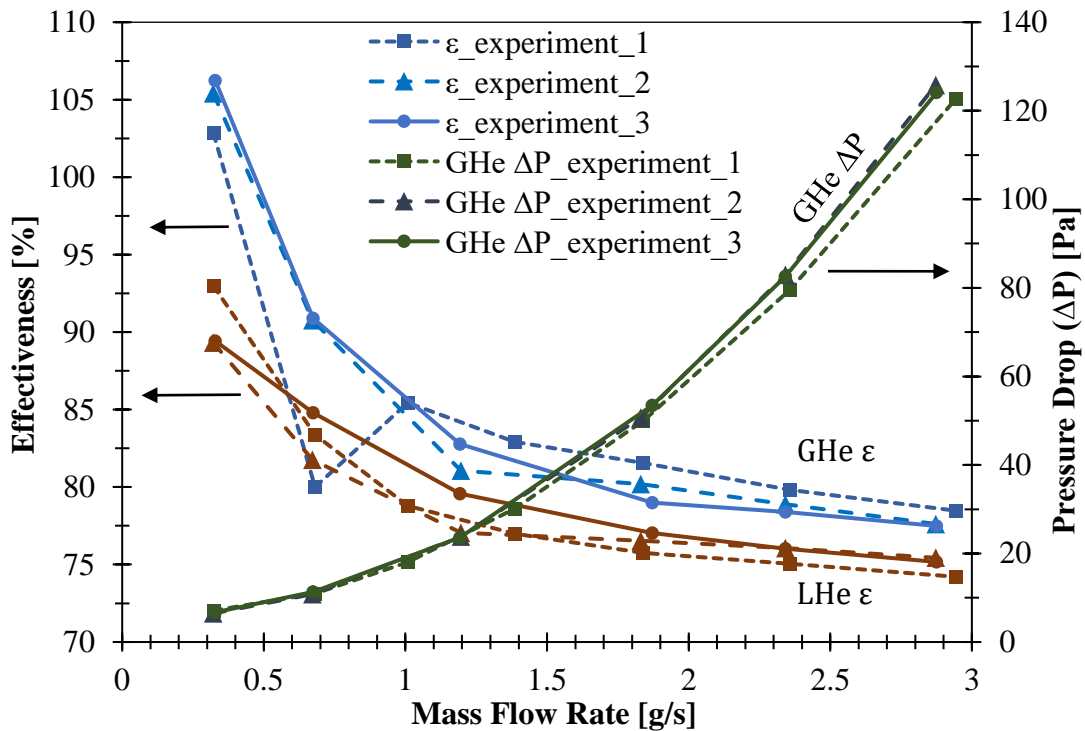


Figure 6-11: Experimental effectiveness and GHe ΔP of the 2K HX_1.

The effectiveness of the 2K HX_1 can be determined from the known temperature and pressure conditions, as shown in Figure 6-10(a) and Equations 6.1-6.3, and the results are summarized in Figure 6-11. The actual heat transferred by fluids to each other through the 2K HX_1 has an error of approximately 2% at 3 g/s flow rate, showing that the amount of heat removed by GHe is always higher than that given by the LHe. This is in part due to the heat load from surroundings coming to the SS316L wall, enclosing the 2K HX_1. The effectiveness (LHe effectiveness) obtained at 3 g/s of flow rate to the 2K HX_1 was 75% (from Figure 6-11), which provided 2.41 K of subcooled LHe at the outlet of the 2K HX, for GHe inlet temperature of 2.0 K, as seen in Figure 6-10(a). More so, the obtained effectiveness was higher at lower flow rates (80% at 0.8 g/s) and kept on reducing with increments in flow rates. The reason for such reduction in effectiveness from lower to higher flow rate is due to the GHe and LHe heat transfer coefficients, h_{GHe} and h_{LHe} , being directly proportional to Re^n , where $n < 1$. This causes the heat transfer coefficients not to rise with the same rate as the mass flow rate of the fluids, hence reduced heat transfer capability at higher flow rates

[18]. The flash loss at 3 g/s of flow rate to the 2K HX was 12%. The target value for the operational mode of the superfluid helium cryogenic system is 9.4%, corresponding to the 2K HX's LHe outlet temperature of 2.2 K. The GHe ΔP through the 2K HX at 3 g/s of flow rate was determined to be 135 Pa. In Chapter 7, the design of the 2K HX_1 will be improved to increase its effectiveness and reduce the GHe ΔP .

In Figure 6-11, it is also noticeable that the GHe effectiveness is $> 100\%$ at < 0.5 g/s flow rate, and according to the definition of effectiveness it is not possible to be $> 100\%$. The reasoning behind this unusual phenomenon is the heat in-leak to the cold GHe flowing through the 2K HX_1 SS316L shell, from the surrounding thermal shields (\dot{Q}_s) and the ICF inlet connection for the hot LHe (4.2 K) (\dot{Q}_L) acting as a constant temperature heat source, as seen in Figure 6-12. This effect is much higher at lower flow rates (< 0.5 g/s), since the heat in-leak ($\dot{Q}_s + \dot{Q}_L$) is comparable to the heat transferred between the fluids, showing the amount of heat removed by the GHe (\dot{Q}_{GHe}) higher than the maximum possible heat transfer (\dot{Q}_{max}). However, this does not affect the amount of heat given by LHe (\dot{Q}_{LHe}) flowing through the helical tube, since it is surrounded by the cold GHe. From the experimental results the heat in-leak for the 2K HX_1 remained at an average of 0.43 W, as there was no bypass flow.

$$\dot{Q}_{GHe} = \dot{Q}_{LHe} + (\dot{Q}_s + \dot{Q}_L). \quad (6.5)$$

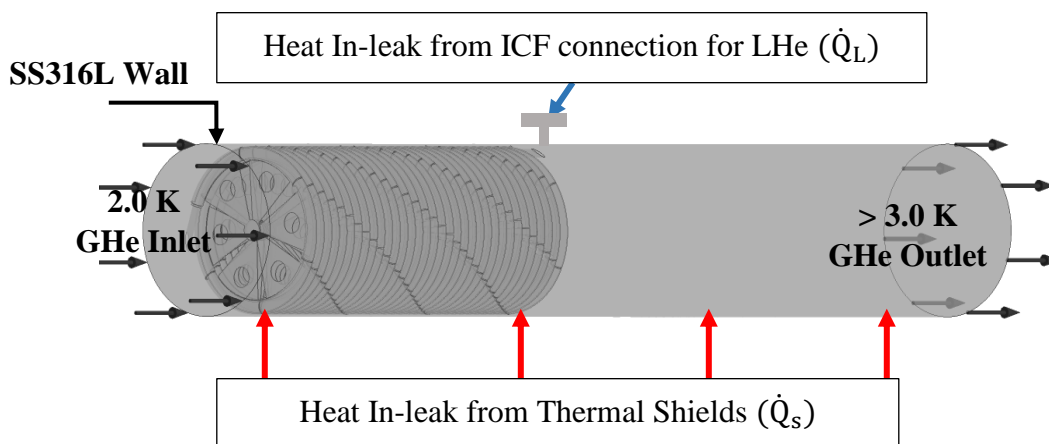


Figure 6-12: Thermal load from surroundings to the GHe flowing through 2K HX_1 shell.

6.4.2. Flow meter accuracy measurement

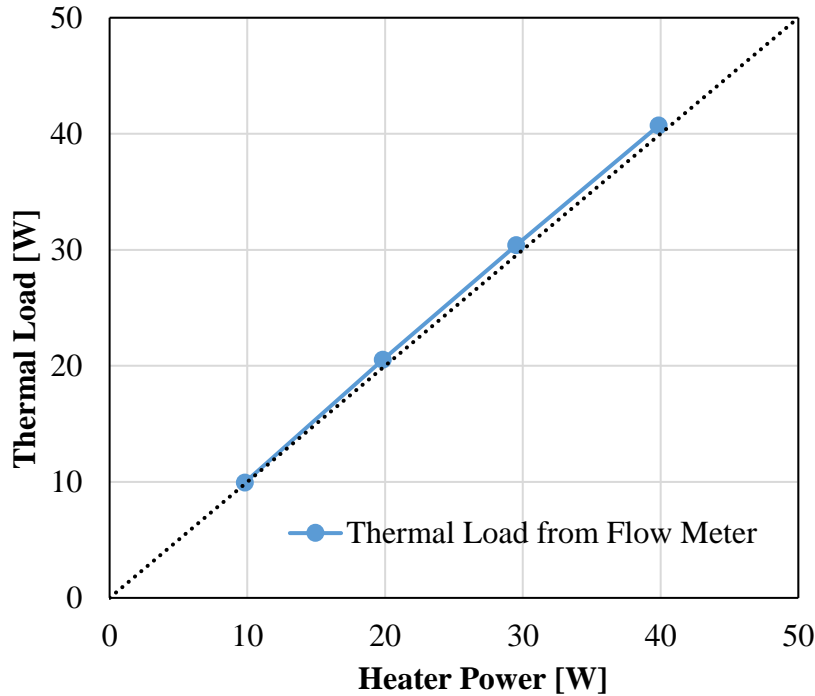


Figure 6-13: Thermal load obtained from the flow meter with respect to heat load to He II.

In Figure 6-13, the flow meter's performance is shown. The static loss from the He II tank is difficult to measure, since the flow meter doesn't show flow rates below 0.2 g/s or 5 W heater power. Moreover, it is noticeable from the obtained data that the static loss is negligible from the He II tank, as the amount of thermal load obtained from the flow meter measurement is almost similar to the input heater power to the superfluid helium in the He II tank maintained at 2.02 K. From the obtained data, it can be said that the accuracy of the flow meter is ± 0.05 g/s, and it is of utmost importance that no pump oil leaks into them with the outgoing GHe, as it effects the accuracy of the data obtained from the flow meters.

6.5. Performance of the 2K HX_1

The methodology that is employed to determine the effectiveness of a 2K HX_1 is shown below:

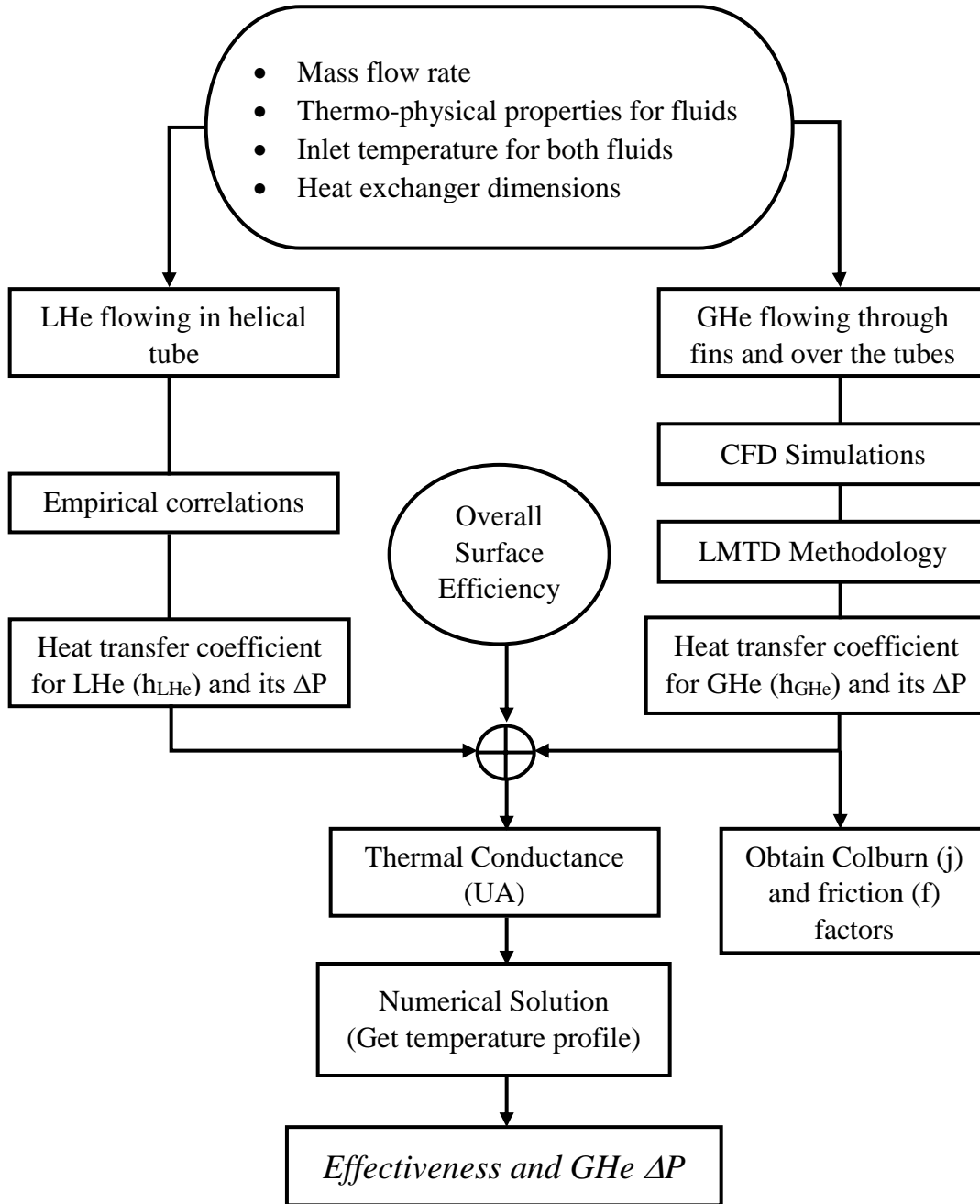


Figure 6-14: Algorithm for determining 2K HX effectiveness.

6.5.1. 2K HX_1 numerical model

In the last section, the 2K HX_1 performance was measured at different flow rates using a heat exchanger test stand. The 2K HX_1's experimental effectiveness was determined to be 75% with GHe ΔP of 135 Pa at 3 g/s. In Figure 6-15, the CFD model for the 2K HX_1 is shown, consisting of the GHe domain and 2K HX_1 body.

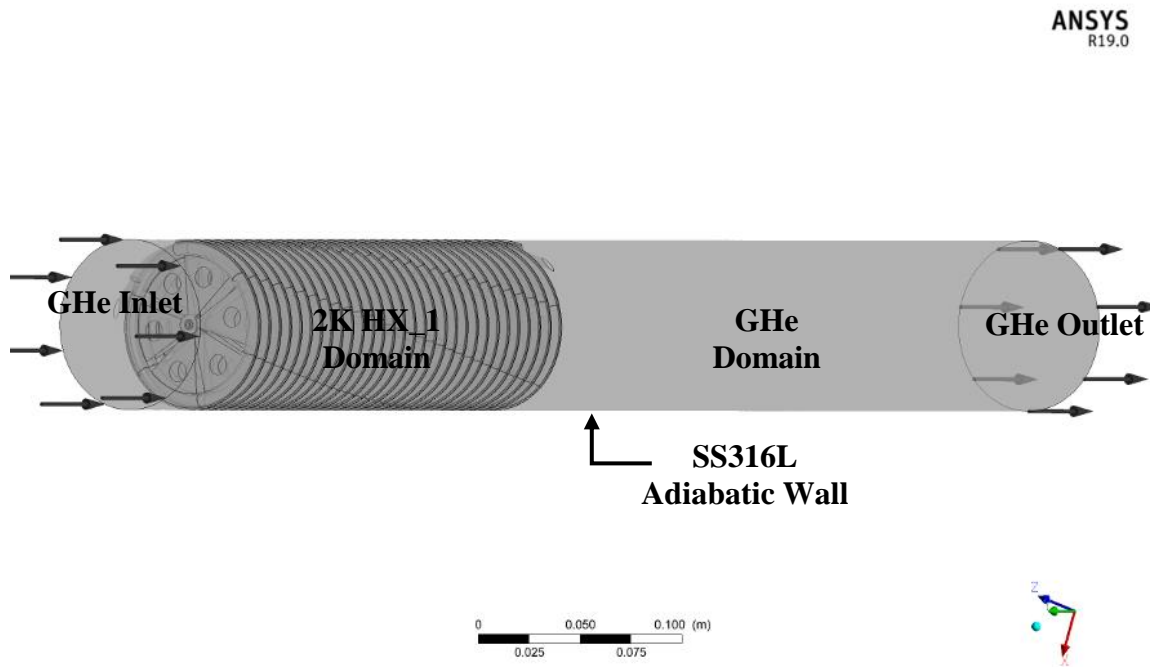


Figure 6-15: CAD model for the 2K HX_1 performance analysis at various flow rates.

In Table 6-1, the parameters that are necessary to determine the effectiveness numerically for the 2K HX_1 are shown. The heat transfer coefficient and pressure drop for the LHe at different flow rates were determined with the aid of empirical relations shown in Section 5.6.3. The heat transfer parameters for GHe are determined by the CFD simulations of the 2K HX_1 CAD model, as shown in Figure 6-15, at different flow rates. Tables 6-2 and 6-3 show the thermal models, boundary conditions and initial conditions necessary to perform the CFD simulation for the 2K HX_1.

Table 6-1: Process parameters of the 2K HX_1.

Fluid / Solid	Inlet Temperature (T _i) [K]	Outlet Temperature (T _o) [K]	Pressure (P) [kPa]	Density (ρ) [kg m ⁻³]	Specific Heat Capacity (C _p) [Jkg ⁻¹ K ⁻¹]	Dynamic Viscosity (μ) [μPa.s]	Thermal Conductivity (k) [Wm ⁻¹ K ⁻¹]
GHe	2.0	-	2.8	0.522	Variable	0.70	0.005
LHe	4.4	>2.2	125	138.7	Variable	3.68	0.017
OFC	-	-	-	-	-	-	1050

Table 6-2: 2K HX_1 domain and the initializing conditions.

Domain	Fluid/ Solid	Temperature (K)	Turbulence Intensity (%)	Turbulence Model	Wall Function
GHe	GHe	2	4.4	k-ω SST	Automatic
OFC	OFC	4.4 K constant temperature with no fouling resistance			

Table 6-3: Boundary conditions for the 2K HX_1 in ANSYS CFX®.

Boundary	Fluid/ Solid	Mass flow rate [gs ⁻¹]	Turbulence Intensity [%]	Static Temperature [K]	Total Pressure [kPa]
GHe Inlet	GHe	Up to 3	4.4	2	-
GHe Outlet		-	-	-	2.8
OFC	OFC	Interface between OFC and GHe			
Wall	SS316L	-	-	Adiabatic	-

6.5.2. Results and discussion

From the obtained heat transfer coefficients of individual fluids, the overall thermal conductance (UA) at different flow rates for the 2K HX_1 was determined. Then, from the numerical model described in Section 5.2 and the algorithm given in Figure 6-14, the temperature profile for the fluids was determined with FDM. The obtained temperature profile for the fluids is shown in Figure 6-16, from which the outlet temperature of the fluids could be obtained. Now, from the known outlet and inlet temperatures of the fluids the effectiveness

Experimental and Numerical Investigation of the 2K HX_1

of the 2K HX_1 is calculated. The calculated performance parameters for the 2K HX_1 is summarized in Table 6-4, and their comparison with respect to the experimental results is shown in Figure 6-17.

Table 6-4: Summarized performance parameters for the 2K HX_1.

Mass Flow Rate [gs ⁻¹]	Inlet Temperature [K]		Outlet Temperature [K]		h_{LHe} [Wm ⁻² K ⁻¹]	h_{GHe} [Wm ⁻² K ⁻¹]	UA [WK ⁻¹]	ϵ [%]	GHe ΔP [Pa]
	$T_{h,i}$	$T_{c,i}$	$T_{h,o}$	$T_{c,o}$					
	1	4.4	2	2.42					
2	4.4	2	2.54	3.15	1823	40.9	12.6	75.8	53.4
3	4.4	2	2.63	3.11	2516	55.9	17.0	73.1	118

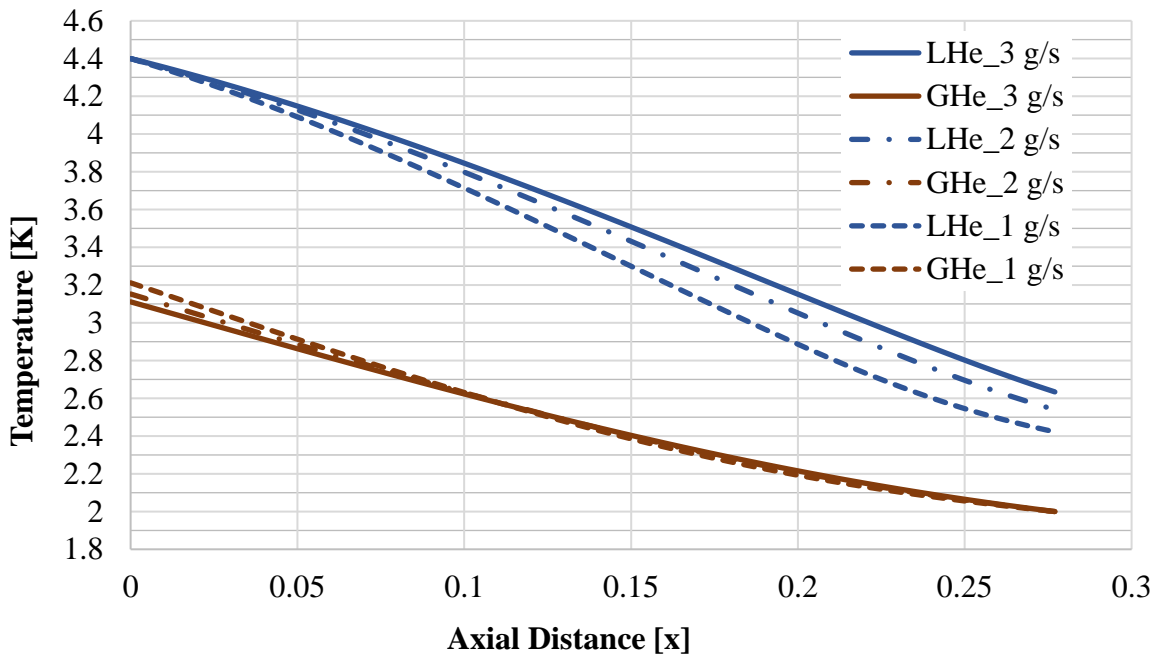


Figure 6-16: Temperature profile of the fluids flowing through the 2K HX_1 at various flow rates.

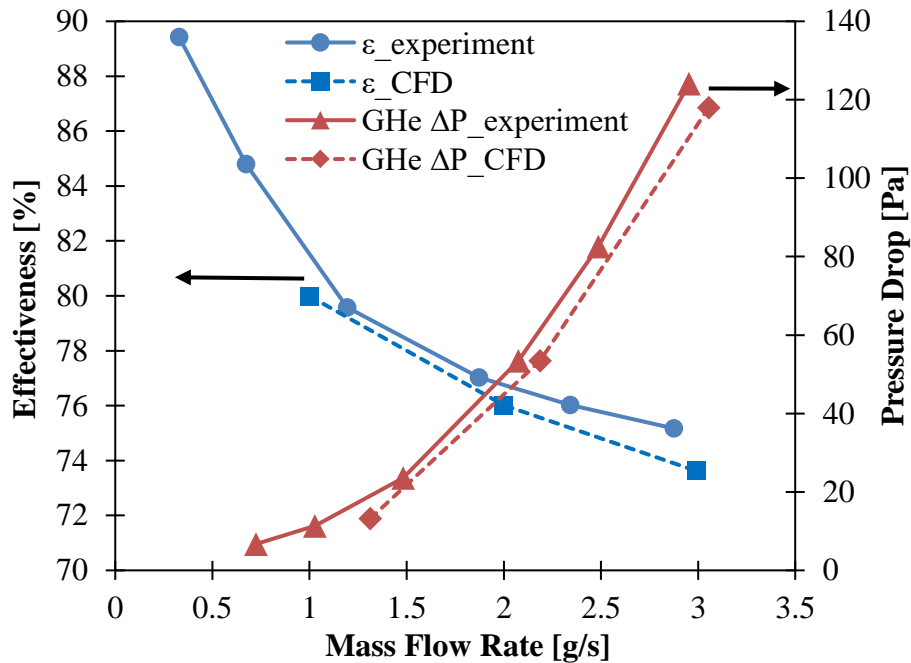


Figure 6-17: Comparison experimental and numerical results for the 2K HX_1 performance.

The effectiveness (LHe effectiveness) of the 2K HX_1 from its numerical model is determined to be 73.2 % at 3 g/s, as shown in Figure 6-17. The LHe effectiveness is true representation of effectiveness of the 2K HX_1, as it is void of any parasitical heat load from the surroundings. The GHe ΔP is determined to be 118 Pa at 3 g/s, which is 10% lower than the one determined from experiments. The general wisdom dictates that the effectiveness and pressure drop from CFD is supposed to be higher than the experimental results, since the simulation does not consider fouling resistance and thermal resistance from the brazed fins. The observed lower effectiveness from the CFD simulations is due to the lack of uniformity in the manufacturing process. The CAD model was developed from the visual inspection of the 2K HX_1 (top and bottom view) and that introduced unnecessary errors in the accurate portrayal of the 2K HX_1 through its CAD model. In the later chapters, another 2K HX was manufactured with a controlled manufacturing process, and the results were verified with the heat exchanger test stand.

6.5.3. GHe flow behavior through 2K HX_1

In Figure 6-18, the Colburn and friction factors are shown for the 2K HX_1 geometry, determined from the heat transfer coefficient and the pressure drop of GHe, respectively. These are useful for comparing different designs of the heat exchangers. These factors also help the designers to determine hydraulic diameter, pressure drop, etc. In the next chapter, a parametric study will be conducted to improve the current 2K HX_1 design. The experiences gained from analyzing the current 2K HX_1 design will be helpful in improving its design to better its performance.

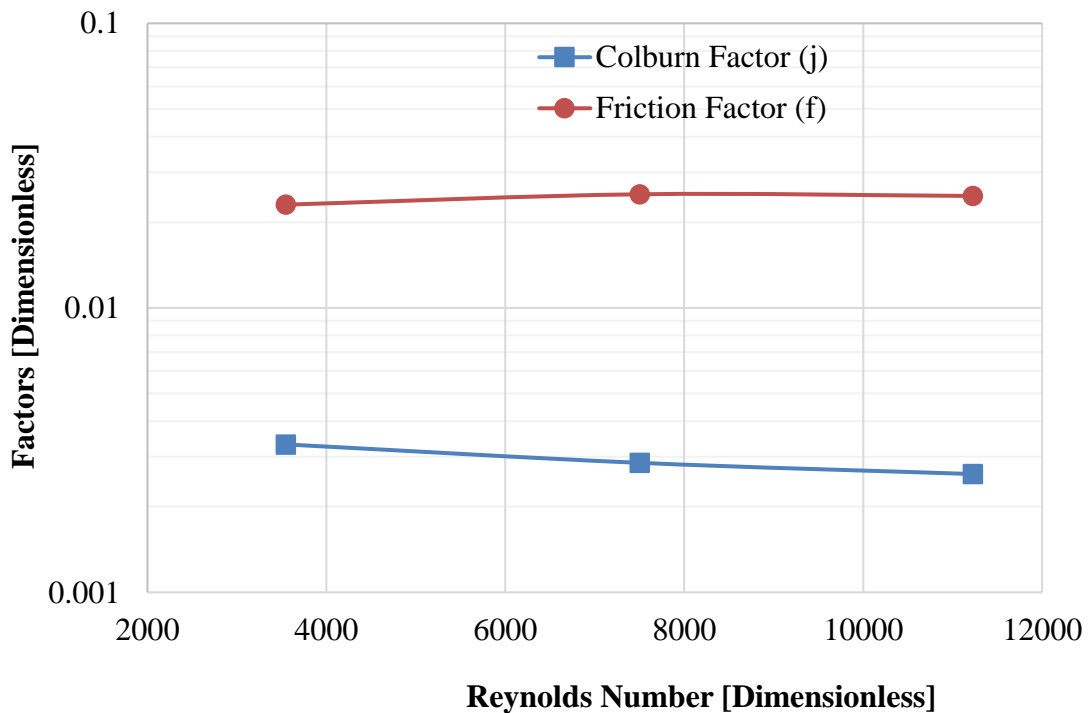


Figure 6-18: Colburn and friction factors for the GHe flowing through the 2K HX_1 geometry.

Experimental and Numerical Investigation of the 2K HX_1

From the CFD simulations, the behavior of the GHe flow through the 2K HX_1 can be visualized. In Figure 6-19, it is possible to see the streamlines of the GHe velocity on a cross-sectional plane parallel to the GHe flow direction. The streamlines show eddy formation between the fins of the 2K HX_1, due to the boundary layer separation and wake generation behind a blunt body like this heat exchanger's fins. It also shows the bypass flow through the holes of the fins accelerating the fluid to higher velocities. This kind of flows improves the heat transfer coefficient of the fluid at lower Reynolds numbers by increasing its turbulence kinetic energy, as also seen in Figure 6-20, but this also affects the pressure drop as eddy formation occurring between the fins will increase the GHe ΔP through the geometry. As seen in Figure 6-18, the ratio of friction to Colburn factors for the 2K HX_1 is approximately 9 or above, usually this ratio is much lower for other kind of well-known heat exchanger geometries such as staggered tube bundles (~ 4), plate-fin surface (~ 3) and finned-tube bundle (~ 4). Hence, it would be ideal to have the friction to Colburn factor ratio near to the geometries mentioned above to better the performance of the 2K HX_1.

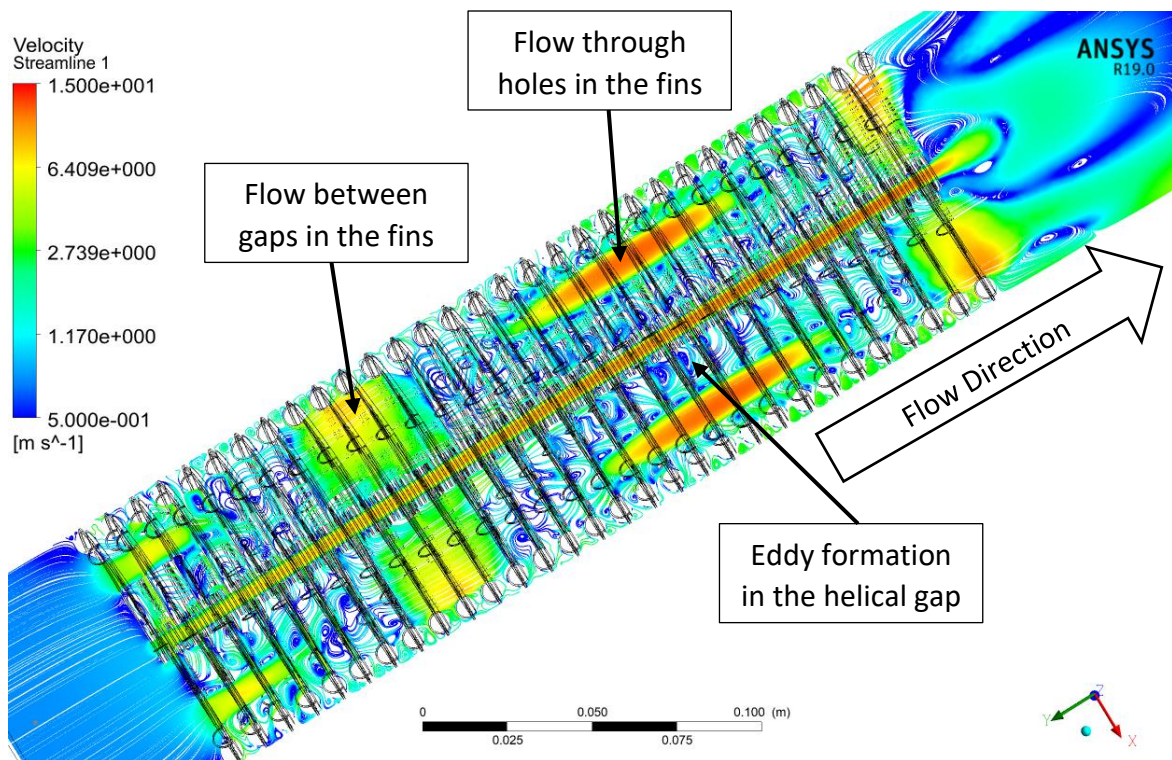


Figure 6-19: Velocity streamline for the GHe flowing through the 2K HX_1.

Experimental and Numerical Investigation of the 2K HX_1

In Figure 6-20, the turbulence kinetic energy of the GHe flowing through the 2K HX_1 geometry is shown on a cross-sectional plane, parallel to the GHe fluid flow. The turbulence kinetic energy is lower at the inlet of the 2K HX_1 due to absence of fins to create turbulence, after the fluid passes through the first array fins the turbulent kinetic energy starts rising. It keeps on rising due to increasing velocity (density reduces with rise in temperature) through the 2K HX_1, but becomes somewhat stable after approximately 8 loops.

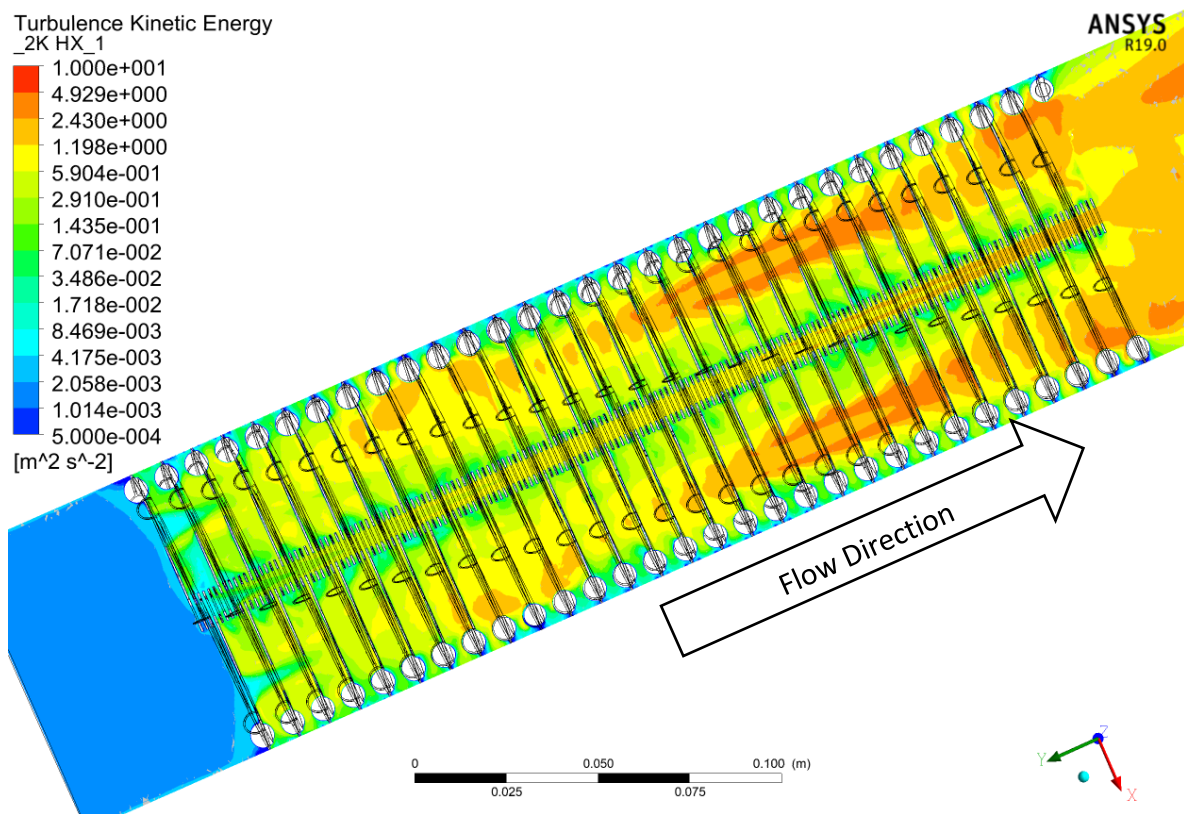


Figure 6-20: Turbulence kinetic energy for the GHe flowing through the 2K HX_1.

Chapter 7. PARAMETRIC STUDY OF THE 2K HX_1

7.1. Objective

In the last chapter, the performance of the 2K HX_1 was determined using the heat exchanger test stand, and its performance was validated by its numerical model. In this chapter, a parametric study will be conducted to improve the performance of the 2K HX_1. It will be a component based study to improve the effectiveness of the 2K HX_1, while keeping the GHe ΔP similar to or lower than the 2K HX_1s' GHe ΔP at 3 g/s. A set of design features will be studied in the already established numerical model of the 2K HX_1 to improve its design. The studied design parameters are categorized in Section 7.2.

The following assumptions will be employed for the parametric study:

- All simulations will be performed at 3 g/s constant mass flow rate (\dot{m}).
- 2K HX_1 operates in steady state conditions with no heat inleak from surroundings.
- The fouling effect and the thermal resistance between silver brazed fins on the helical tube are neglected (unknown).
- The longitudinal conduction effect in this 2K HX is neglected, as the longitudinal conduction parameter is low $\lambda = 3.1 \times 10^{-4}$ at 3 g/s flow rate, and its effect on effectiveness below 90% is negligible.
- The Kapitza resistance which becomes considerable below lambda point is also neglected.
- The GHe ΔP is directly proportional to \dot{m}^2/ρ , hence it increases with mass flow rate raised to square and decreases with increase in density.

Parametric Study of the 2K HX 1

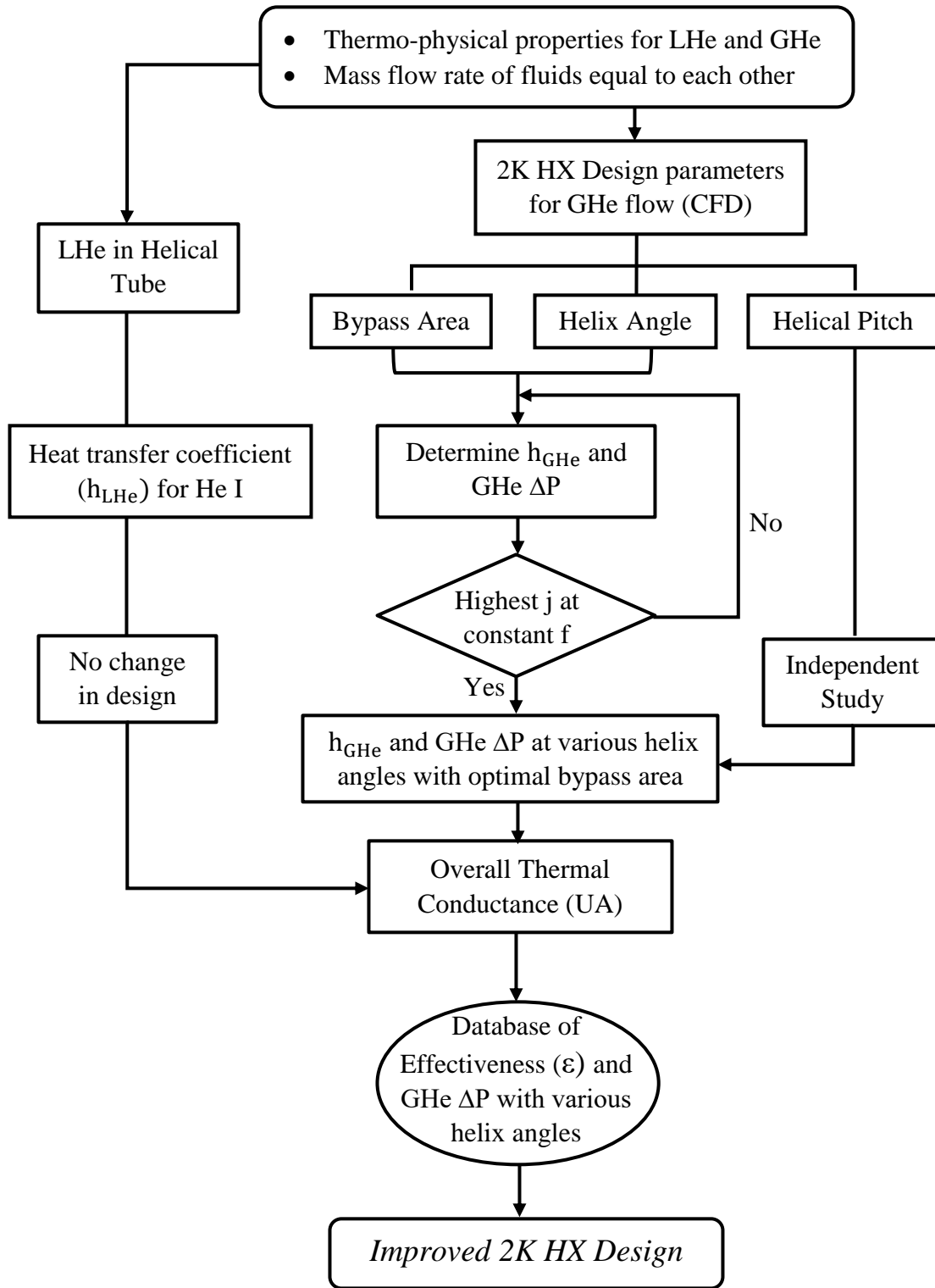


Figure 7-1: Algorithm for the parametric study of the 2K HX_1.

7.2. Parameters for the Design Study

For the parametric study, the overall size of the 2K HX is kept unchanged, especially total axial length, tube dimensions, helix diameter and fin design. The design factors that are considered to study and improve the design of the 2K HX are:

- 1) **Bypass Area:** It is the area between the outer SS316L shell and the 2K HX body, through which the flow bypasses without interacting with the helical tube and fins. In this study, it is defined as the ratio of frontal bypass area to the frontal free flow area. As the 2K HX_1 is made of OFC, it is quite soft and malleable, so it is possible to change the helix diameter to vary the shell gap or reduce the shell size to reduce the bypass area. It was varied from the maximum allowable 7.2% to zero by reducing the shell diameter from 84.9 mm to 82 mm.

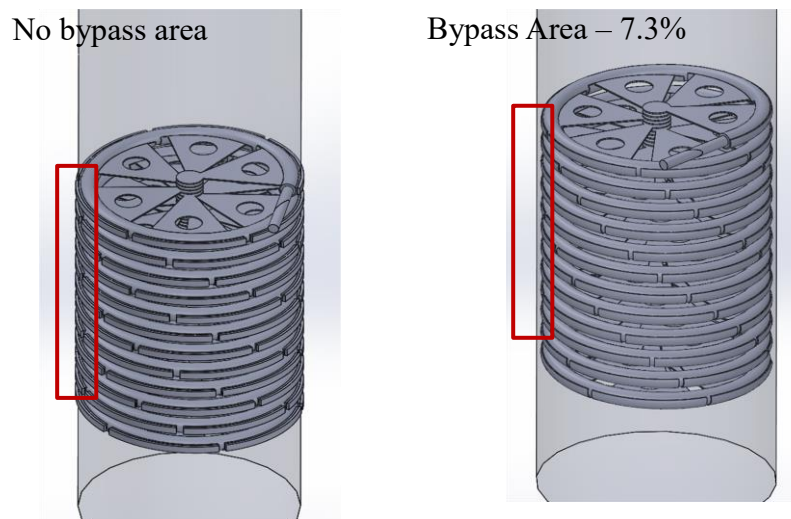


Figure 7-2: Bypass area for the 2K HX.

- 2) **Helix angle (θ):** It is the angle that the laminated fins make with respect to the helical coils' axis to vary the 2K HX's fins alignment. If the space between the fins is zero, all the fins are aligned and the helix angle is 0° , hence axially aligning the holes in the fins, as seen in

Parametric Study of the 2K HX 1

Figure 7-3. Increasing the fin spacing introduces staggered arrangement for the fins, producing helix angles $> 0^\circ$. At the helix angle of 48° , the arrangement becomes as staggered (misaligned holes) as it can be and increasing the fin spacing after that just repeats the pattern, hence repeating the parameters like heat transfer coefficient and GHe ΔP . This parameter was varied from 0° to 70° to create two cycles of pattern repetition. The inspiration for this study is taken from the extensive studies performed on heat exchangers with tubes in aligned and staggered arrangements [30].

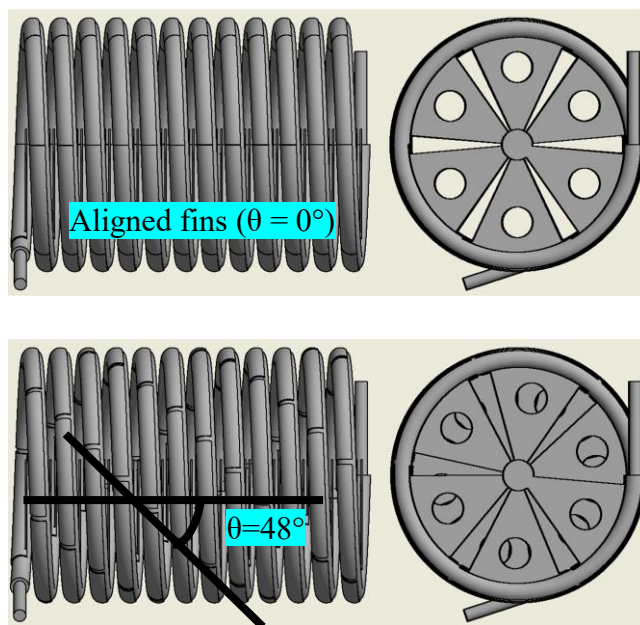


Figure 7-3: Helix angle for the CFD analysis of the 2K HX.

- 3) **Helical pitch:** It is the height of one complete helix turn of OFC tube. The original helical pitch is 9 mm, and it was reduced till 7 mm to study its effect on the heat transfer coefficient and pressure drop for the GHe flowing through 2K HX, as seen in Figure 7-4. As the diameter of the tube is 6 mm, the minimum possible helical pitch that can be achieved is 6.5 mm, due to the presence of fins on the helical tube. At this point, the individual helix will touch each other and will incrementally increase the longitudinal heat conduction through the helical tube by shortening the path of heat flow from 7 m to just 0.28 m. This study is conducted to improve the compactness of the 2K HX_1.

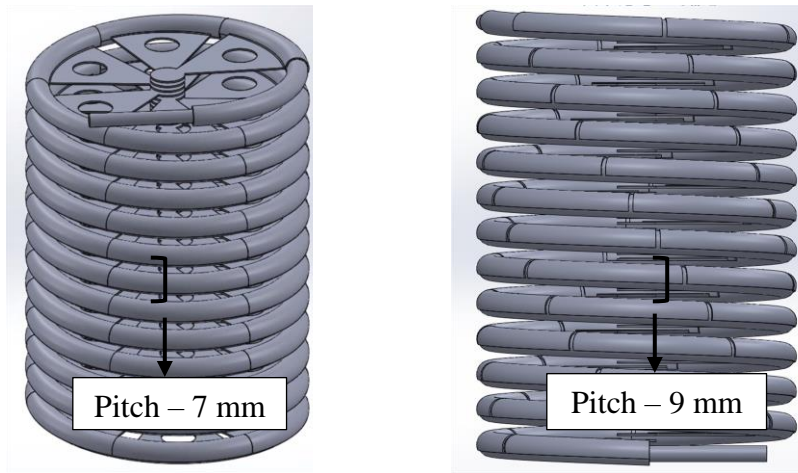


Figure 7-4: Helical pitch for the 2K HX.

7.3. Results and Discussion

The changes in parameters described in the previous section provided a database of heat transfer coefficient and pressure drop for the GHe. Furthermore, the database of heat transfer coefficients was normalized using the Colburn analogy and from the GHe ΔP the friction factor for the database was determined. As the heat transfer coefficient of LHe is a known quantity and remains constant for the given dimensions of a helical tube at a certain flow rate, the effectiveness of a 2K HX can be determined through FDM, as described in Chapter 5. Error in the amount of heat transferred between fluids from averaging the fluid properties is avoided by FDM to include the property variation of specific heat capacity of fluids, which governs the temperature profile of fluids in the heat exchanger. The results obtained from the studies are discussed in the following section.

7.3.1. Effect of the bypass area and helical angle

At first, the parameters' bypass area and the helix angle effect on the effectiveness and GHe ΔP of the 2K HX_1 was analyzed. A section of the heat exchanger 1/3rd (12 loops) of the 2K HX geometry was simulated for this study, as the flow properties almost become stable after

Parametric Study of the 2K HX 1

4 loops of the 2K HX [19]. This way many simulations could be performed in a short period of time. It provided the performance data as shown in Figures 7-5 and 7-6.

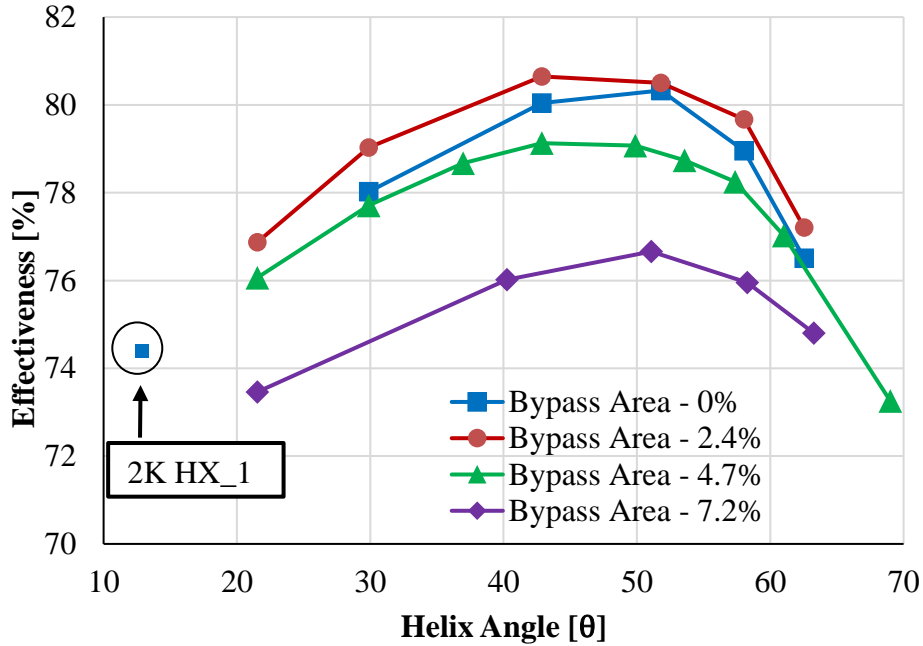


Figure 7-5: Effectiveness for the 2K HX with variation in helix angle and bypass area.

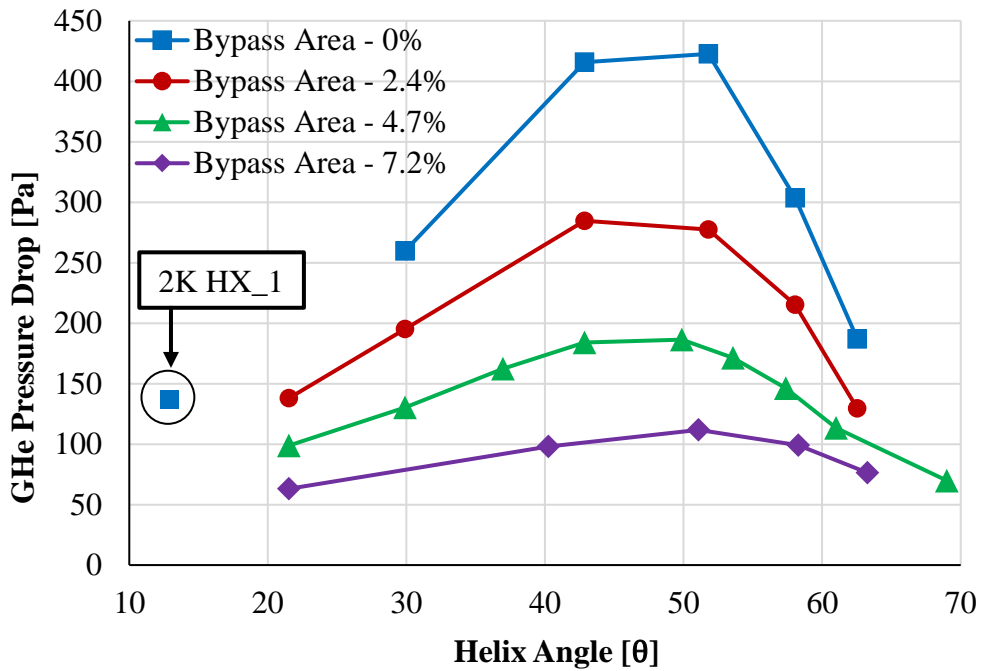


Figure 7-6: GHe ΔP for the 2K HX with variation in helix angle and bypass area.

Parametric Study of the 2K HX 1

The heat transfer coefficient obtained from the CFD simulation, as seen in Figure F.2 in appendices, for a section of the 2K HX is applied for its whole geometry. Also, the GHe ΔP is extrapolated from 12 loops to 30 loops. Figures 7-5 and 7-6 show the effectiveness obtained from the heat transfer coefficients and the GHe ΔP , at various combinations of bypass areas and helix angles. From Figure 7-5, it is noticeable that a highly effective 2K HX ($> 84\%$ at 3 g/s) is not possible. It is due to the steep rise in specific heat capacity for the LHe below 2.5 K, generating the requirement of either higher surface area or the higher heat transfer coefficient for GHe than currently available.

For the varied helix angles at different bypass areas, the maxima for effectiveness was at $\sim 50^\circ$. The 2K HX_1 helix angle is approximately 13° , and its effectiveness and GHe ΔP are plotted in Figures 7-5 and 7-6, respectively, showing lower GHe ΔP but at the expense of its effectiveness. At the helix angle 0° , the holes in the fins align over each other, causing a part of the GHe to flow through the 2K HX without extracting any heat from it. At the higher helix angle $>30^\circ$, the effectiveness is closer to 80% due to the misaligned holes creating more turbulence and interaction with fins, hence a higher heat transfer coefficient but at the expense of higher GHe ΔP . Increasing the helix angle above 48° , repeats the 2K HX's fin pattern periodically, hence repeating the effectiveness and GHe ΔP for the 2K HX.

As changes in the bypass areas and helix angles produce similar behavior with the performance parameters, the datasets of the obtained effectiveness and GHe ΔP will be observed to eliminate certain settings of the bypass areas. From Figure 7-6, it is noticeable that with a bypass area of $< 2.4\%$, the GHe ΔP is quite high and not in acceptable ranges (< 150 Pa at 3 g/s), as high GHe ΔP can hinder the pumping capacity of the cryogenic systems, hence limiting the He II production rate. The bypass area of 7.2% has lower GHe ΔP , but the effectiveness is too low to be considered for the improved design for the 2K HX. With the bypass area of 4.7%, a good balance is achieved between the effectiveness and GHe ΔP for the 2K HX. Furthermore, the bypass area of 4.7% gives higher effectiveness with lower GHe ΔP with respect to the other settings, as shown in Table 7-1.

Parametric Study of the 2K HX 1

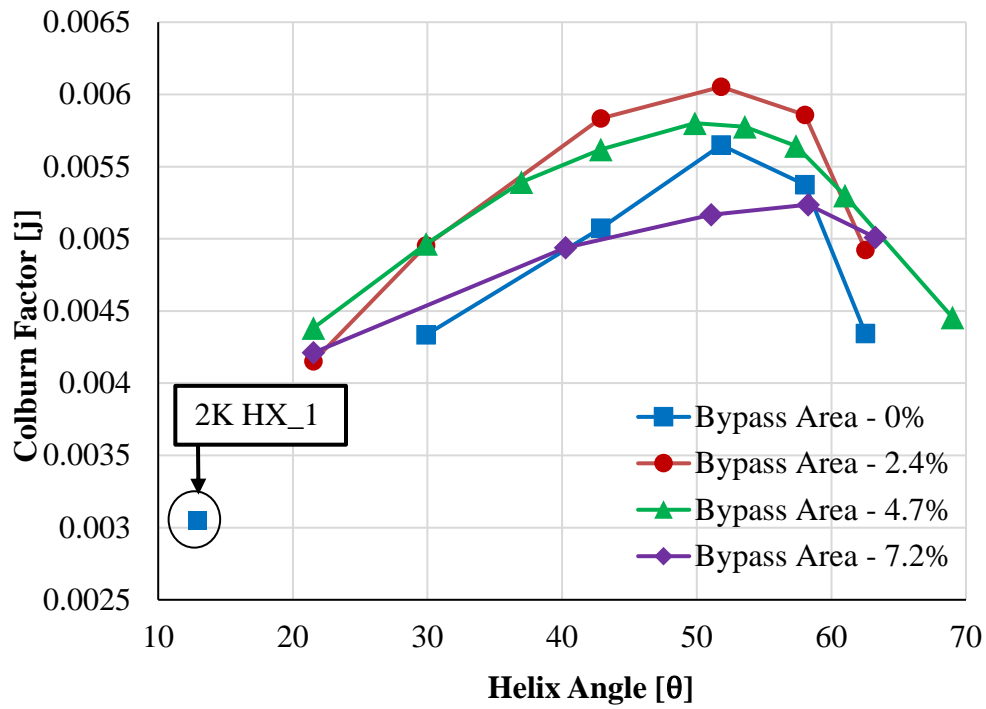


Figure 7-7: Colburn factor for the GHe at different helix angle with varied bypass area.

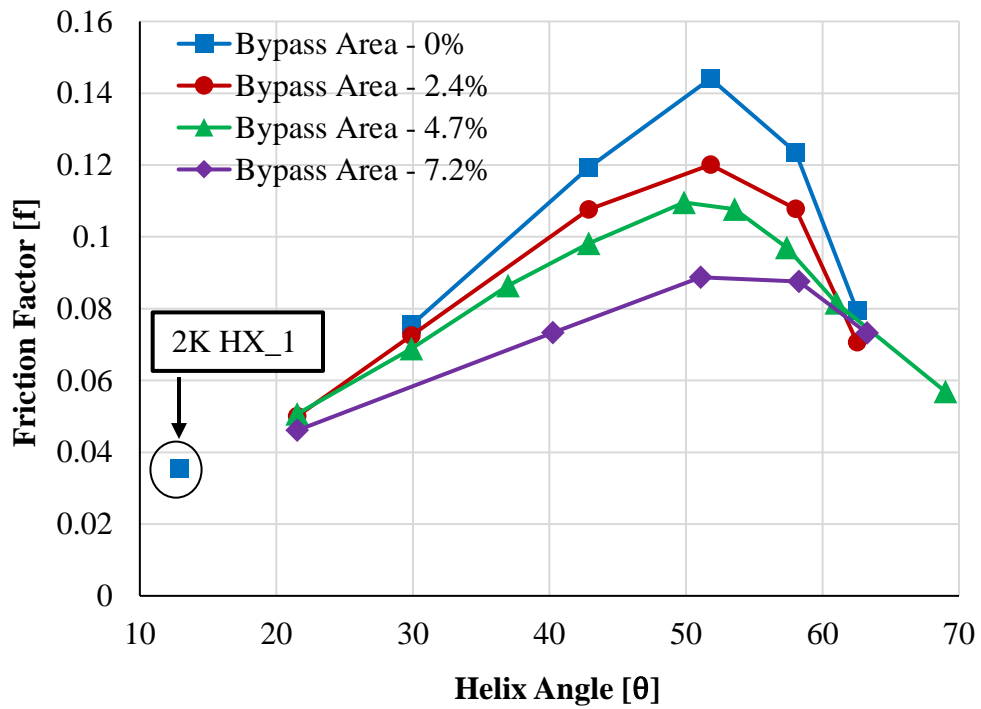


Figure 7-8: Friction factor for the GHe at different helix angle with varied bypass area.

Parametric Study of the 2K HX 1

The obtained heat transfer properties of GHe are the heat transfer coefficient and the GHe ΔP , which were normalized using the Colburn factor and the friction factor for the 2K HX geometry. In Figure 7-7, it is noticeable that the peak of the Colburn factor is highest with the bypass area of 2.4% and the lowest with the bypass area of 7.2%. This trend is different from one showed in Figure 7-5, where the peak of the heat transfer coefficient (proportional to effectiveness) is highest for a bypass area of 0% and lowest for a bypass area of 7.2%. So, the heat transfer coefficient normalized with respect to mass flux flowing through it shows that at bypass area of 2.4% the Colburn factor is the highest.

In Figure 7-8, the friction factor with respect to helix angles at various bypass areas is plotted and has the same behavior as the plot in Figure 7-6. The peak of the friction factor is highest for the 0% bypass area and lowest for the 7.2% bypass area. The friction factor increases along with an increase in helix angle, with its maxima at around 50° and after that it starts to drop again.

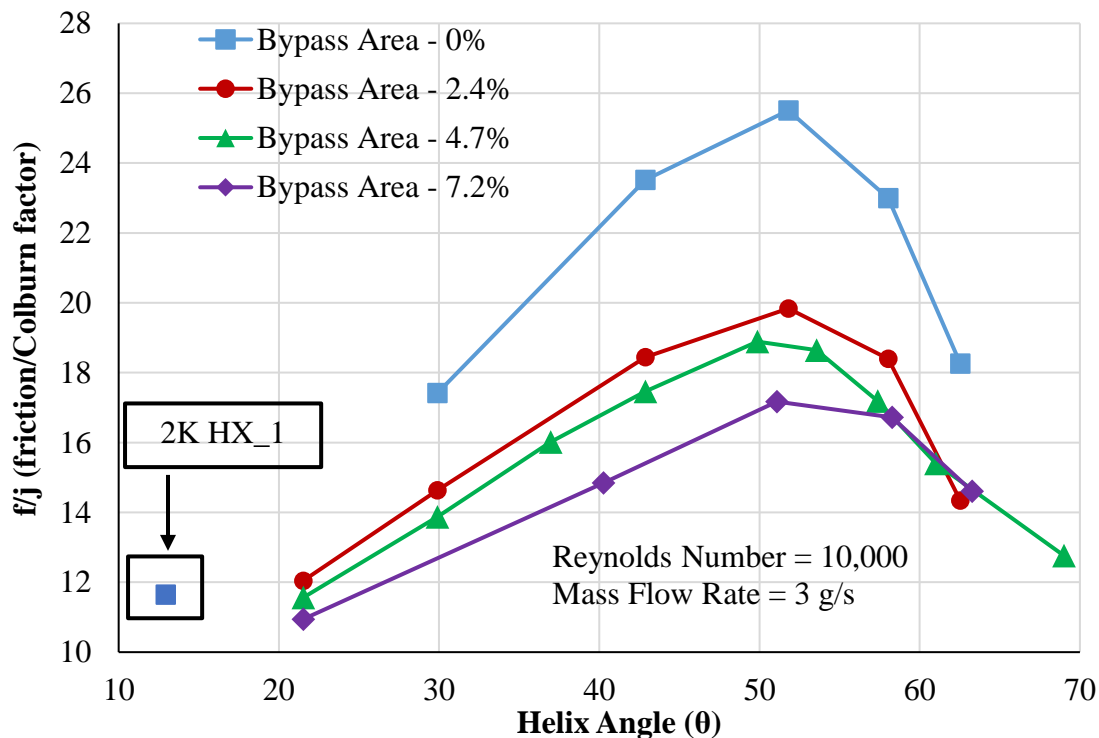


Figure 7-9: friction to Colburn factor ratio for the GHe at different helix angle with varied bypass area.

Parametric Study of the 2K HX 1

Another noticeable fact is the behavior of the ratio of the friction to the Colburn factor with respect to helix angle, as seen in Figures 7-9 and 7-13. It remains stable below 10° helix angle with a value of ~ 8 to 9 and a steep rise is observed from 10° to 51° helix angle, then it drops again due to fin pattern repetition. The steep rise can be attributed to change in the flow behaviour when the helix angle is increased. With higher helix angle $> 10^\circ$, the interaction between fins and GHe flow is improved due to lesser bypass flow through the fins, but the frequency of separating flow due to the fin geometry is also increased, hence higher turbulent kinetic energy and eddy formation. According to the available data for the tubes in aligned and staggered conditions, which is analogous to the fin geometry for the 2K HXs, the ratio for friction to Colburn factor is 13% higher for staggered tubes than the aligned tubes, at Reynolds number of 10000 with hydraulic diameter of 0.05 m [33]. Although there is no appreciable change in the rise of friction to Colburn factor ratio for the aligned to staggered tubes, it was very much different in the case of fin arrangement for this 2K HX, as it increased by 70% from $\theta = 0^\circ$ to $\theta = 51^\circ$. This behaviour could not be confirmed with the visuals from the simulations, since it was not possible to extract exact flow behaviour of GHe through the 2K HXs.

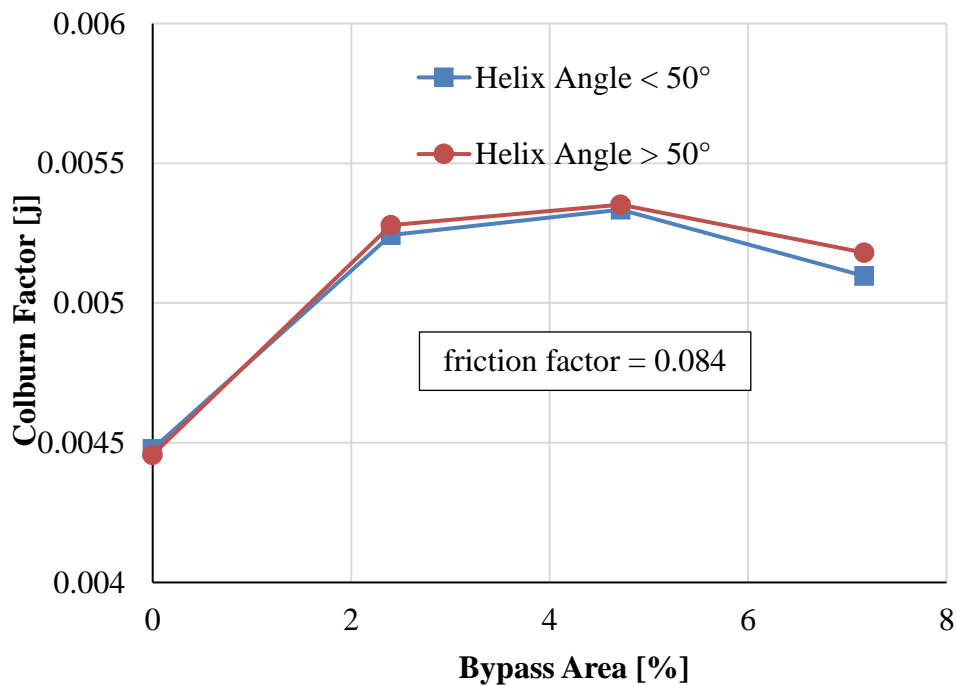


Figure 7-10: Colburn factor for the GHe with varied bypass area at a constant friction factor.

Parametric Study of the 2K HX 1

The Colburn and friction factors for the GHe flowing through the 2K HX's geometry also provided us with the optimal bypass area. From Figure 7-10, it can be seen that for a constant friction factor of 0.084, the Colburn factor is highest for the 4.7% bypass area. Moreover, if the Colburn factor is correlated with a certain value of the friction factor for helix angles above and below 50 degrees, the Colburn factor remains the same in both regions, as it can be seen in Figure 7-10. This observed behavior made us choose the bypass area of 4.7% as an ideal and manufactural setting for the 2K HX.

7.3.2. Effect of helical pitch

This study was conducted by considering a 2K HX design with a fixed bypass area and changing the helix angle according to the helical pitch variation, to keep the pattern of the fins similar.

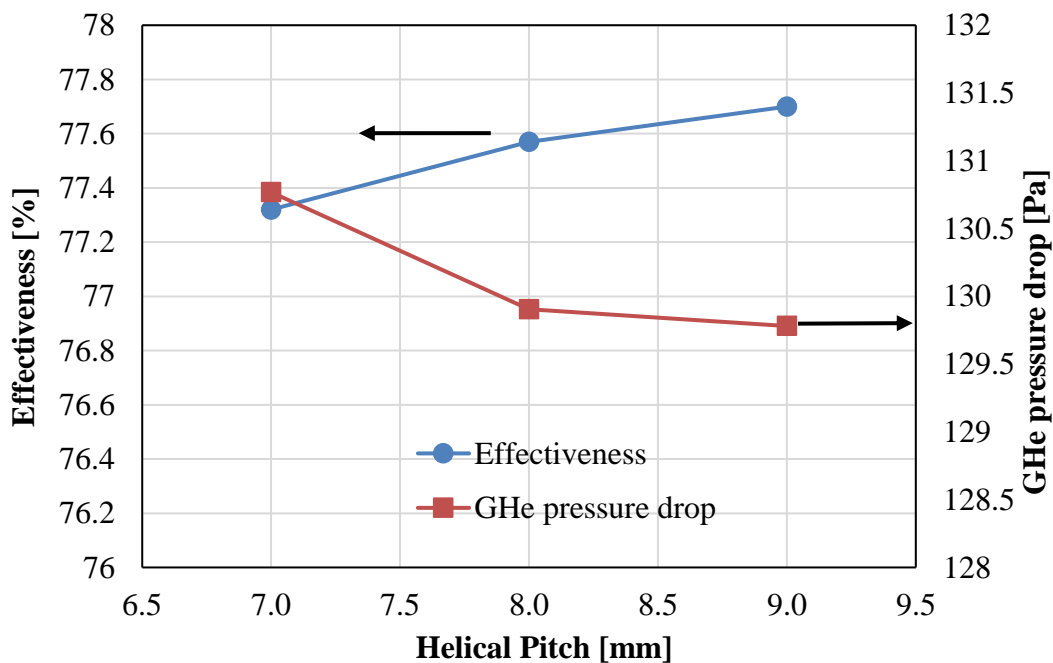


Figure 7-11: Effect of the varied helical pitch on the effectiveness and GHe ΔP of the 2K HX.

Parametric Study of the 2K HX 1

As seen in Figure 7-11, the effect of a reduced helical pitch on the effectiveness and GHe ΔP of the 2K HX is minimal at best. The reduction of the helical pitch by 2 mm causes effectiveness to drop by 0.6% and an increase in GHe ΔP by $< 1\%$. The original helical pitch of the 2K HX was 9 mm, which provided 2.5 mm of gap before the loops touch each other. That gap is necessary for inserting and placing the fins on the helical tube for brazing. Due to these constraints, the helical pitch was just reduced by 1 mm to 8 mm and not 2 mm, which provides unused axial length to add 4 more loops to the 2K HX, while keeping the total axial length of the 2K HX unchanged. In Table 7-1, it is evident that to achieve an effectiveness of 79%, the GHe ΔP and the friction factor of 9 mm helical pitch are higher than the 8 mm one. Adding 4 more loops to the 2K HX provides 13% more surface area for GHe to remove heat from the LHe flowing through the helical tube. It is true that it increased the GHe ΔP too, but it was observed that it is better to increase the number of loops rather than to change the helix angle of the fins to achieve higher effectiveness, this way making it possible to keep the GHe ΔP as minimal as possible.

Table 7-1: Effect of varied helical pitch on the effectiveness of 2K HXs.

Helical Pitch (mm)	Bypass Area (%)	Effectiveness (%)	GHe ΔP (Pa)	Friction Factor
9	4.7	79	178	0.0948
8	4.7	79	112	0.0513
7	4.7	79	100	0.0378

7.3.3. Improved designs for the 2K HX

As discussed in Sections 7.3.1 and 7.3.2, the bypass area of 4.7% is an optimal setting that should be applied for the new design. Also, the helical pitch was reduced to 8 mm to provide 13% more surface area for GHe. The data obtained for the effectiveness and GHe ΔP at 3 g/s

Parametric Study of the 2K HX 1

for various helix angles at 4.7% bypass area and 8 mm helical pitch is shown in Figure 7-12, and their respective normalized parameters for GHe are shown in Figure 7-13. The effectiveness should be accurate enough as the heat transfer coefficient is mostly independent of temperature variation, while the error in the GHe ΔP is kept at minimum by performing simulations at a constant wall temperature of 3.6 K. The constant wall temperature of 3.6 K produces the expected operational temperature gradient for the GHe flowing through the 2K HX. The following observations were made from the obtained results:

- a) From Figure 7-12 and Table 7-2, the effectiveness was improved from 75% to 79.8% at 3 g/s, with similar GHe ΔP as 2K HX_1. It was achieved at the helix angle of 33°. With this heat exchanger design the flash loss will be reduced from 12.5% to 10.5%.
- b) If the effectiveness of 2K HX_1 is considered as a reference, at an effectiveness of 75% the GHe ΔP can be reduced by 50%, from 135 Pa to 69 Pa, as seen in Table 7-2.
- c) If the 2K HX has to produce 2.2 K LHe at the outlet of 2K HX, i.e. effectiveness > 84% throughout the operation, it is not possible with the current parameters and restrictions even if the bypass area is reduced.
- d) The optimized design cannot be specifically described in this study, since 84% effectiveness was not achieved, hence the obtained results in Figure 7-12 will be employed in the superfluid helium cryogenic systems to determine the optimized design for the 2K HX.
- e) To produce an effectiveness > 84% at 3 g/s, it is necessary to increase the surface area interacting with the GHe. It is achievable by increasing the axial length of the 2K HXs in Figure 7-12, which will be shown in the next section.
- f) In section 7.3.1 a possible theory behind the behaviour of friction to Colburn factor ratio as also seen in Figure 7-13 was presented, which is also valid for the improved 2K HXs shown in Figure 7-12. The variation of turbulence kinetic energy through the improved 2K HXs geometry is shown in Appendices Figure F.1.

Parametric Study of the 2K HX 1

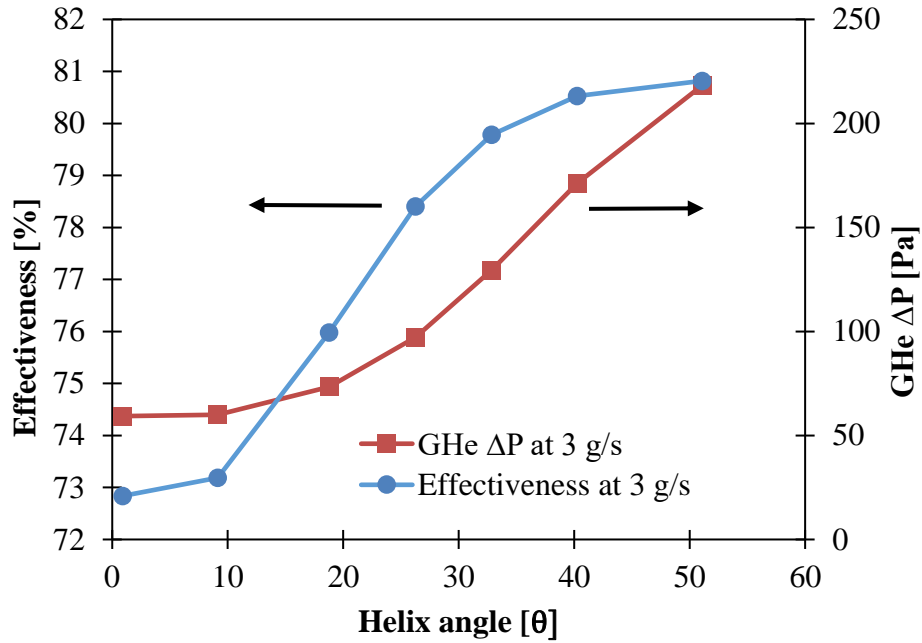


Figure 7-12: Effectiveness and GHe ΔP for various helix angles with 4.7% bypass area and 8 mm helical pitch. This data is for 3 g/s flow rate and at a constant wall temperature of 3.6 K.

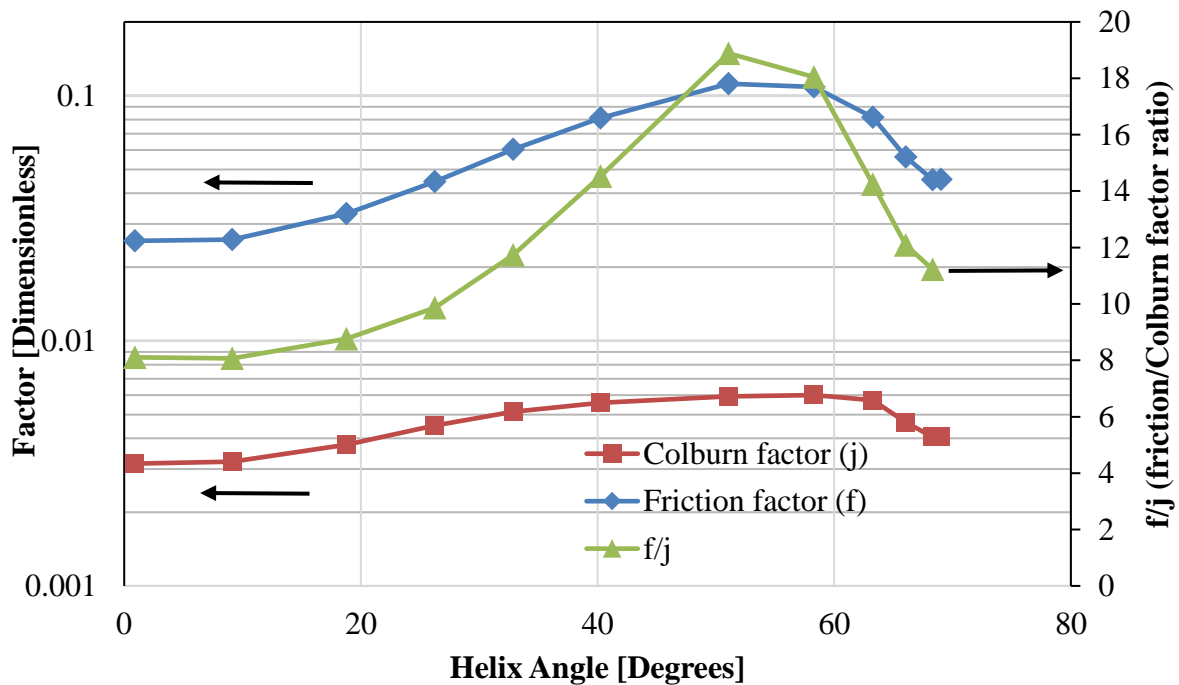


Figure 7-13: Colburn and friction factors and their ratio for the GHe at various helix angles with 4.7% bypass area and 8 mm helical pitch.

Parametric Study of the 2K HX 1

Table 7-2: Comparison of improved 2K HXs with axial length restriction with respect to the 2K HX_1.

Geometric Parameters	2K HX_1	2K HX (GHe ΔP as reference)	2K HX (Effectiveness as reference)
Helical tube parameters			
Tube OD (thickness)	$\Phi 6$ (t1) mm	$\Phi 6$ (t1) mm	$\Phi 6$ (t1) mm
Helix diameter (pitch)	75 (9) mm	$\Phi 75$ (8) mm	$\Phi 75$ (8) mm
Number of loops	30	34	34
Helix angle	13°	33°	15°
Total dimensions			
2K HX axial length	277 mm	279 mm	279 mm
2K HX diameter	$\Phi 82$ mm	$\Phi 82$ mm	$\Phi 82$ mm
Bypass Area	Nil	4.7%	4.7%
Performance Parameters			
Effectiveness @ 3 g/s	75%	79.8%	75%
GHe ΔP @ 3 g/s	136 Pa	135 Pa	69 Pa
LHe outlet temperature @ 3g/s	2.5 K	2.36 K	2.5 K
Vapor flash loss @ 3 g/s	12.5%	10.5%	12.5%

7.3.4. Improved 2K HX without axial length restriction

In the last section, it was not possible to achieve 84% effectiveness at 3 g/s with the current fin design and the dimensions restriction. The cryogenic systems at KEK use two 2K HX_1 (unknown helix angle) in series for each 2K cold box, hence the axial length of the heat exchanger can be increased to twice the current value, if necessary. The helix diameter cannot be increased due to the space limitation inside the 2K cold box for both cryogenic systems. In this section, the length of the heat exchanger will be varied with the known heat transfer coefficients for the optimal parameters with a bypass area (4.7%), helical pitch (8 mm) and variable helix angle, to achieve 84% effectiveness at the lowest possible GHe ΔP at 3 g/s flow rate. The maximum allowable axial length (L) is two times the axial length of the 2K HX_1 (here taken as L_0). The results from the study are shown in Figure 7-14 and summarized in Table 7-3:

Parametric Study of the 2K HX 1

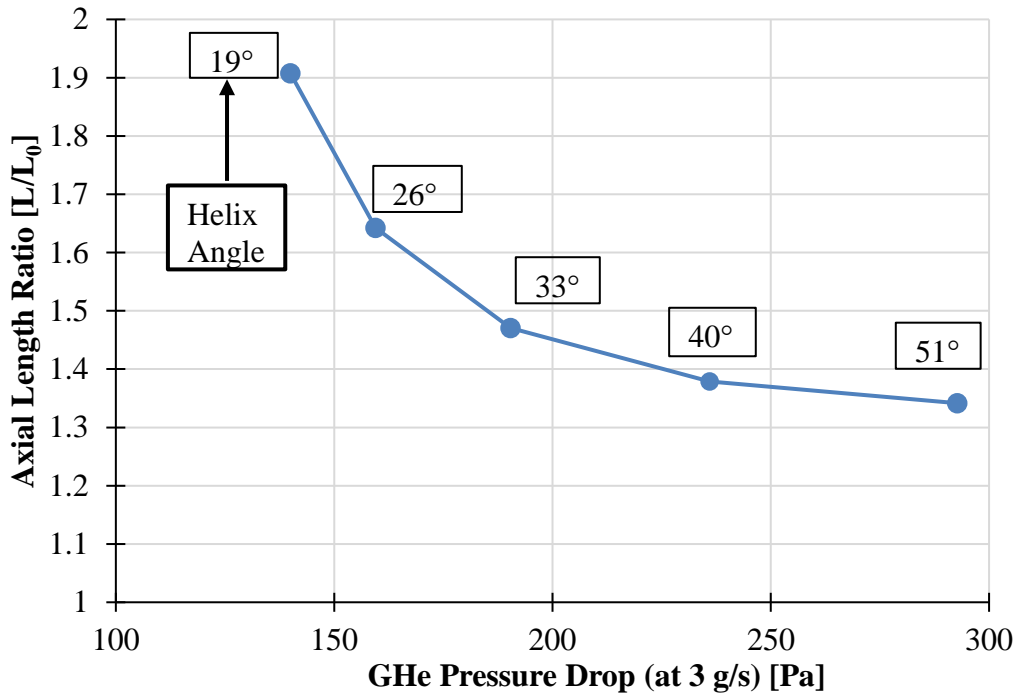


Figure 7-14: Required axial length for the 2K HX to obtain 84% effectiveness with various helix angles at 3 g/s flow rate.

Table 7-3: Comparison of improved 2K HX without axial length restriction with respect to the 2K HX_1 in the cryogenic systems.

Performance Parameters	2K HX_1 (in STF and cERL)	2K HX_1 (2 in series)	2K HX w/o axial length restriction
<i>Helical tube parameters</i>			
Tube OD (thickness)	Φ6 (1) mm	Φ6 (1) mm	Φ6 (1) mm
Helix diameter (pitch)	75 (9) mm	Φ75 (9) mm	Φ75 (8) mm
Number of loops	60	60	65
Helix angle	Unknown	13°	19°
<i>Total dimensions</i>			
2K HX axial length	554 mm	554 mm	520 mm
2K HX diameter	Φ82 mm	Φ82 mm	Φ82 mm
Bypass Area	Nil	Nil	4.7%
<i>Performance Parameters</i>			
Effectiveness @ 3 g/s	84%	83.3%	84%
GHe ΔP @ 3 g/s	600 Pa	270 Pa	140 Pa
LHe outlet temperature @ 3g/s	2.2 K	2.2 K	2.2 K
Vapor flash loss @ 3 g/s	9.4%	9.4%	9.4%

Parametric Study of the 2K HX 1

In Figure 7-14, the x-axis shows the GHe ΔP at 3 g/s flow rate and the y-axis shows the axial length ratio, which is the ratio of actual length (L) to the original length of one 2K HX_1 (L_0). For a helix angle $< 19^\circ$, it is not possible to obtain 84% effectiveness with the maximum length limit of 2 times the original 2K HX_1. The lowest GHe ΔP is 140 Pa, obtained at 19° helix angle to achieve $> 84\%$ effectiveness at 3 g/s. So, if two 2K HX_1 are considered in series, the GHe ΔP is reduced by 50% from 270 Pa to 140 Pa. As mentioned previously, the 2K refrigerator cold box of the STF and cERL cryogenic systems houses two 2K HX_1 with an unknown helix angle in series per cold box. Thus, comparing the improved 2K HX without an axial length restriction, as given in Table 7-3, with respect to already installed 2K HXs in the STF and cERL facilities, the improved design can reduce the GHe ΔP by 430%. The flash loss remains the same as the two 2K HX_1 in series but its lower GHe ΔP will improve cooling capacity for the superfluid helium cryogenic systems, which will be studied in the next chapter. The importance of lower GHe ΔP through 2K HXs will be shown in Chapter 8, as we know that lower the GHe ΔP , the higher is the flow rate the pumping system can pump at 3.13 kPa, to maintain 2.0 K temperature of He II.

Chapter 8. OPTIMIZATION OF THE SUPERFLUID HELIUM CRYOGENIC SYSTEMS AT KEK

8.1. Objective

In the last chapter, the performance of the 2K HX_1 was improved. In this chapter, the results obtained for the improved 2K HX designs will be employed in the cryogenic systems to conduct a system-based optimization. The main goal of the optimization study will be to maximize the He II production from the cryogenic systems at KEK. The 2K HX design which maximizes the He II production rate will be the optimized design for the superfluid helium cryogenic systems. In this study, the effect of the improved 2K HXs' GHe ΔP coupled with their effectiveness will be studied on the pumping system's ability to maintain constant pressure on He II at 3.13 kPa, hence maintaining its temperature at 2.0 K.

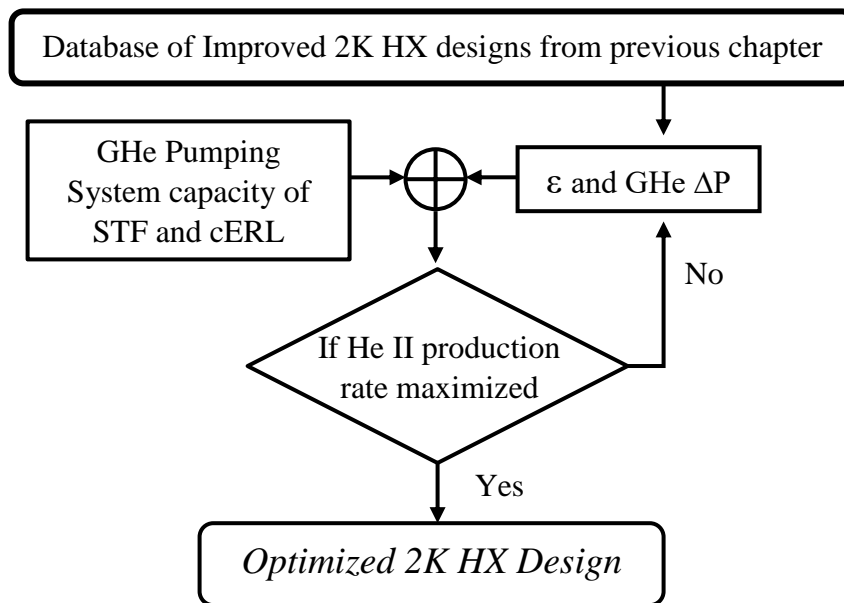


Figure 8-1: Algorithm for the optimization study for the superfluid helium cryogenic systems.

8.2. Effect of the GHe Pressure Drop on the Pumping System Capacity

As discussed in Section 2.2, a pumping system is an integral part of the superfluid helium cryogenic system and is heavily affected by the GHe ΔP through the 2K HX. The GHe ΔP through the 2K HX decides the flow rate of GHe that can be pumped out to maintain 3.13 kPa vapor pressure on the 2.0 K He II, hence directly effecting the production rate of He II from a cryogenic system. The pumping capacities of the cERL and STF pumping systems were determined experimentally with respect to the inlet pressure to the pumps, as shown in Figure 2-7, and will be utilized for the optimization studies.

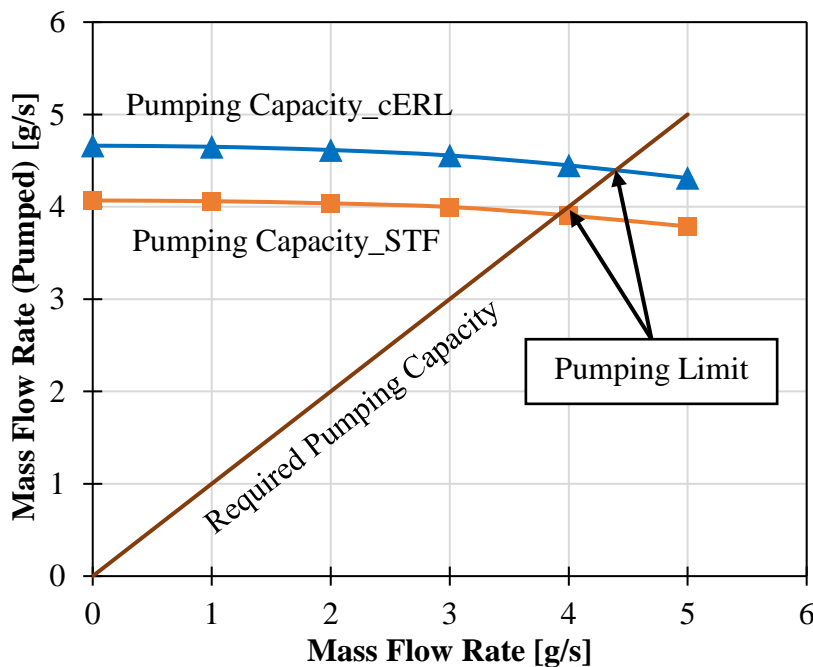


Figure 8-2: Pumping capacity determination using the data from the parametric study conducted for the 2K HX_1.

In Figure 8-2, the x-axis shows the mass flow rate of the GHe through 2K HX and the y-axis shows the mass flow rate of the GHe at the inlet of the pumping system. The plotted curves in Figure 8-2 are described below:

Optimization of the Superfluid Helium Cryogenic Systems at KEK

- *Required pumping capacity (RPC)*: This curve is a 45-degree line and shows the amount of fluid being pumped out by the pumping system corresponding to the mass flow rate through the 2K HX. This flow includes two components: evaporating He II and the vapor flash loss from the JT expansion.

$$\dot{m} = \dot{m}_{\text{He II}} + \xi \times \dot{m} , \quad (8.1)$$

where vapor flash loss, ξ , is the fraction of subcooled LHe that has flashed off in vapor form during the JT expansion. The vapor flash loss is determined from the known effectiveness and the outlet temperature of LHe for the 2K HX and is given by Equation 8-2:

$$\xi = \frac{\dot{m}_v}{\dot{m}} = \frac{[H_{h,o} - H_{h@ \text{sat}}]}{H_{fg}} , \quad (8.2)$$

where, \dot{m}_v is the mass flow rate of the flashed vapor, $H_{h@ \text{sat}}$ and H_{fg} are the enthalpy and the latent heat of He II at saturation pressure and temperature, respectively.

- *Pumping system capacity (PSC)*: With the known GHe ΔP at various mass flow rates, the inlet pressure to the pumping system can be determined and as a result the pumping capacity of the cryogenic systems can be plotted with respect to the mass flowing through them, similar to the curves shown in Figure 8-2.

The intersection of RPC and PSC plots in Figure 8-2 signifies the pumping limit (limiting point) for the cryogenic systems. For mass flow rates below that point, the flow is throttled towards the pumping system to maintain 3.13 kPa pressure on the He II bath, to cool the SRF cavities. For mass flow rates above the limiting point, the GHe ΔP through the 2K HX is too high for the pumps to maintain a constant (3.13 kPa) vapor pressure on the He II. As a result, the He II vapor pressure starts to rise above 3.13 kPa ($\text{He II} > 2.0 \text{ K}$) to compensate for the lower inlet pressure to the pumps, increasing the GHe density, which is not ideal for the SRF cavity operation. The amount of He II produced (HPR) or cooling capacity at the limiting point or at any flow rates, can be calculated by from Equations 8.1-8.3:

$$\text{HPR} = \dot{m}_{\text{He II}} \times \text{Latent Heat @ 2.0 K} . \quad (8.3)$$

8.3. Optimized 2K HX for the Cryogenic Systems at KEK

In the last chapter, with the bypass area of 4.7% and helical pitch of 8 mm, the helix angle was varied to obtain a set of improved designs for the 2K HX. In Figures 7-12 and 7-14, the performance for the improved 2K HXs with and without axial length restriction is known, for various combinations of effectiveness and GHe ΔP . That data will be interpolated using the obtained performance of the improved 2K HXs at various flow rates, shown in Figure 8-3, to determine the effectiveness and the GHe ΔP at the limiting point, hence determining the cooling capacity. As seen in Figures 8-4 and 8-5, the cooling capacity (different from pumping capacity) obtained for the superfluid helium cryogenics system is displayed for the improved 2K HXs with and without axial length restriction. The maxima of the cooling capacity in both figures provide the optimal 2K HX designs for the superfluid helium cryogenic systems and their performances are summarized in Tables 8-1 and 8-2. The optimal 2K HXs are as follows:

- a) If the axial length is limited similar to the 2K HX_1's length, the maximum He II production rate or cooling capacity was determined at a 26° helix angle, henceforth termed as 2K HX_2, as seen in Figure 8-4. It can produce 81.3 W and 91.5 W of He II for the STF and cERL cryogenic facilities, respectively, approximately 4% higher than the cooling capacity of 2K HX_1. The comparative details are shown in Table 8-1.
- b) Since with axial length restriction it was not possible to obtain 84% effectiveness, the results obtained from the studies conducted without axial length restriction were introduced to the cryogenic systems' optimization studies, and the results are shown in Figure 8-5 and summarized in Table 8-2. The 2K heat exchanger that produces the lowest GHe ΔP with an 84% effectiveness at 3 g/s is named as 2K HX_3.
- c) The cooling capacity of the cryogenic systems obtained from the 2K HX_3 is slightly higher than the 2K HX_2, with an added advantage of lowered LHe consumption by at least 2%, as the effectiveness is 5% higher than the 2K HX_2 at 3 g/s.

Optimization of the Superfluid Helium Cryogenic Systems at KEK

- d) As mentioned previously, the 2K refrigerator cold box of the STF and cERL cryogenic systems houses two 2K HX_1 (unknown helix angle) in series per cold box. It was determined experimentally that the GHe ΔP for the 2K HXs installed in the cERL is approximately 600 Pa at 3 g/s, as seen in Figure 2-8. So, comparing the 2K HX_3 with respect to already installed 2K HXs in the STF and cERL facilities, the optimized design (2K HX_3) has 430% lower GHe ΔP with 84% effectiveness, as shown in Table 8-2.
- e) The lower GHe ΔP for the 2K HX_3 improves the cooling capacity of the superfluid helium cryogenic systems by 15%, from 70 W and 80 W to 82 W and 92 W, respectively.

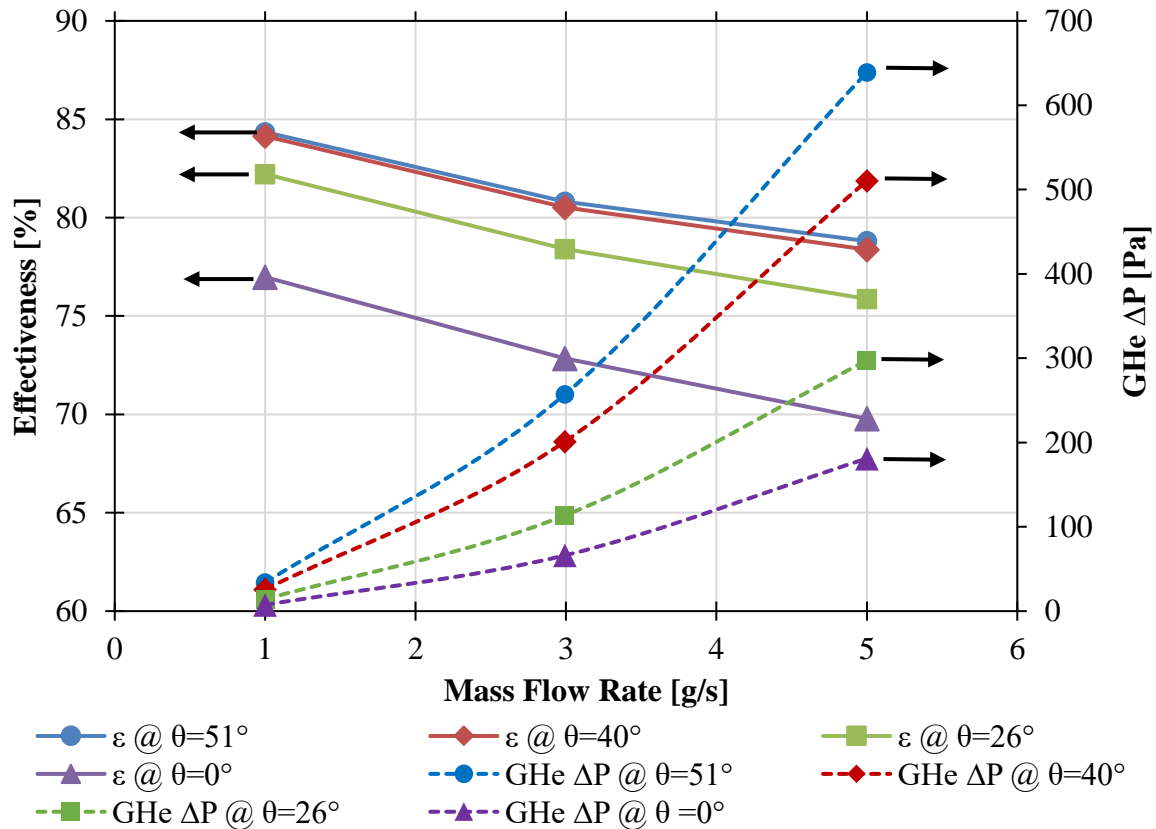


Figure 8-3: Effectiveness and GHe ΔP of the 2K HXs with varied helix angles and at different flow rates with bypass area of 4.7% and helical pitch of 8 mm.

Optimization of the Superfluid Helium Cryogenic Systems at KEK

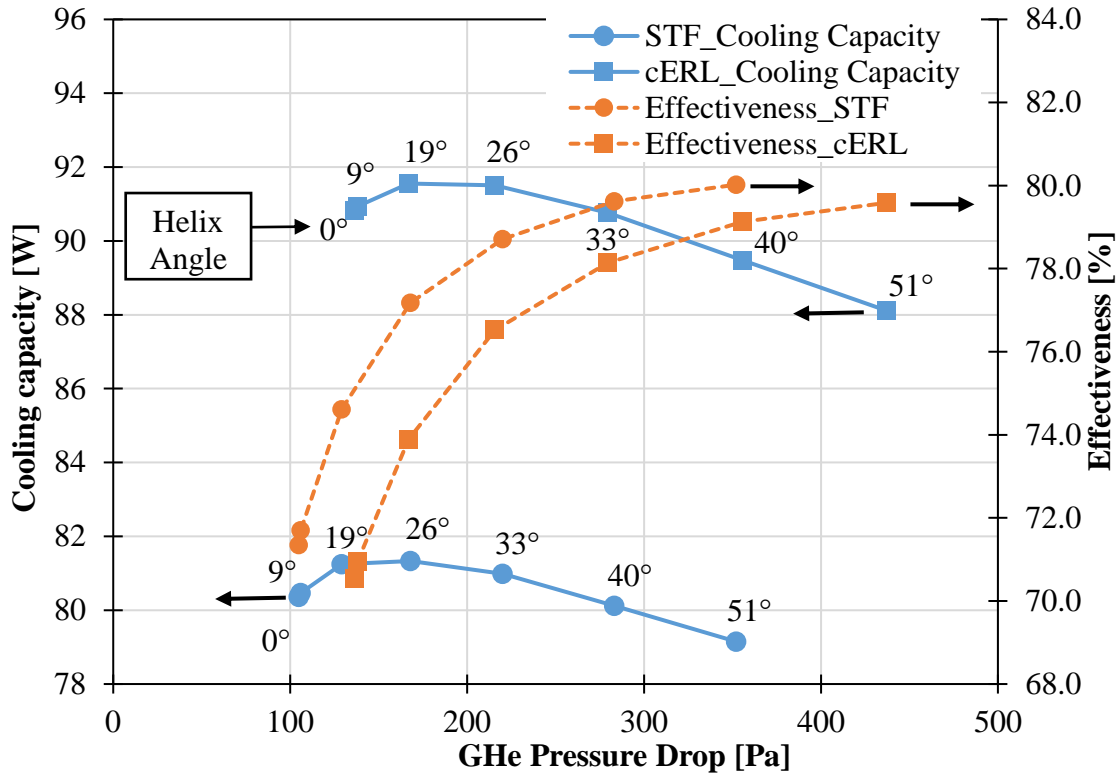


Figure 8-4: Cooling capacity and effectiveness of the 2K HXs with respect to the GHe ΔP at the limiting point with axial length restriction.

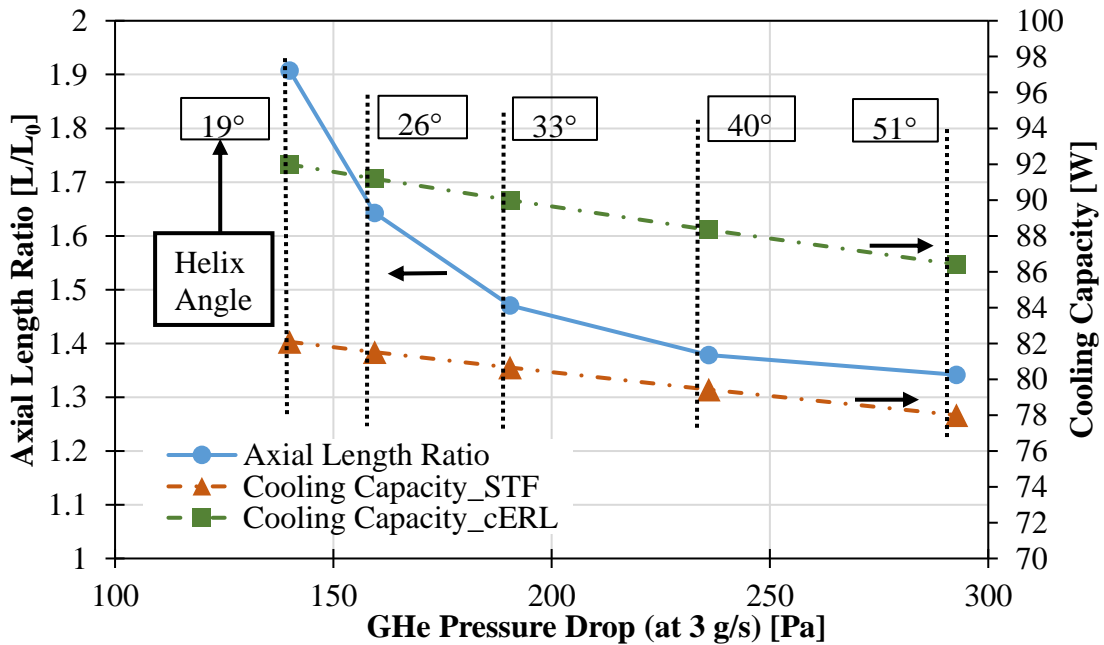


Figure 8-5: Cooling capacity of cryogenic systems for various helix angles at 84% effectiveness and 3 g/s flow rate without axial length restriction.

Optimization of the Superfluid Helium Cryogenic Systems at KEK

Table 8-1: Comparison of the cooling capacity for 2K HXs with axial length restriction.

Geometric Parameters	2K HX_1	2K HX_2
<i>Helical tube parameters</i>		
Tube OD (thickness)	Φ6 (t1) mm	Φ6 (t1) mm
Helix diameter (pitch)	75 (9) mm	Φ75 (8) mm
Number of loops	30	34
Helix angle	13°	26°
<i>Total dimensions</i>		
2K HX axial length	277 mm	279 mm
2K HX diameter	Φ82 mm	Φ82 mm
Bypass Area	Nil	4.7%
<i>Performance Parameters</i>		
Effectiveness @ 3 g/s	75%	78.4%
GHe ΔP @ 3 g/s	136 Pa	97 Pa
LHe outlet temperature @ 3g/s	2.5 K	2.36 K
Cooling capacity_STF @ limiting point	78.5 W	81.3 W
Cooling capacity_cERL @ limiting point	88 W	91.5 W

Table 8-2: Comparison of the cooling capacity for 2K HXs without axial length

Performance Parameters	2K HX_1 (in STF and cERL)	2K HX_1 (2 in series)	2K HX_3
<i>Helical tube parameters</i>			
Tube OD (thickness)	Φ6 (1) mm	Φ6 (1) mm	Φ6 (1) mm
Helix diameter (pitch)	75 (9) mm	Φ75 (9) mm	Φ75 (8) mm
Number of loops	60	60	65
Helix angle	Unknown	13°	19°
<i>Total dimensions</i>			
2K HX axial length	554 mm	554 mm	520 mm
2K HX diameter	Φ82 mm	Φ82 mm	Φ82 mm
Bypass Area	Nil	Nil	4.7%
<i>Performance Parameters</i>			
Effectiveness @ 3 g/s	84%	83.3%	84%
GHe ΔP @ 3 g/s	600 Pa	272 Pa	140 Pa
LHe outlet temperature @ 3g/s	2.2 K	2.2 K	2.2 K
Cooling capacity_STF @ limiting point	70 W	78.3 W	82.1 W
Cooling capacity_cERL @ limiting point	80 W	86.9 W	92 W

Chapter 9. EXPERIMENTAL AND NUMERICAL VERIFICATION OF THE OPTIMIZATION STUDY

9.1. 2K Heat Exchanger for Experimental Verification

In the previous sections, the design of the 2K HX₁ was optimized and to experimentally validate the optimization study, a design closer to the 2K HX₂ was manufactured. The geometric parameters of the heat exchanger design are given in Table 9-1. The manufacturing process was changed slightly to provide the required helix angle to the fins on the helical tube. A G10 comb like spacer was manufactured to provide a bypass area of 4.7% (or 1 mm shell gap) between the 2K HX₂ and its SS316L outer shell. Moreover, the spacer keeps the pitch of the helical tube (8 mm) uniform throughout the heat exchanger body. Three equally placed spacers surrounded the 2K HX body to provide a 4.7% bypass area. A picture of the manufactured 2K HX₂ with its CAD model is shown in Figure 9-1.

Table 9-1: Geometric parameters of the 2K HX₂ compared to the 2K HX₁.

Geometric Parameters	2K HX₁	2K HX₂
Tube OD (thickness)	Φ6 (t1) mm	Φ6 (t1) mm
Helix diameter (pitch)	75 (9) mm	Φ76 (8) mm
Number of loops	30	34
Helix angle	13°	27°
2K HX axial length	277 mm	279 mm
2K HX diameter	Φ82 mm	Φ82 mm
Bypass Area	Nil	4.7%

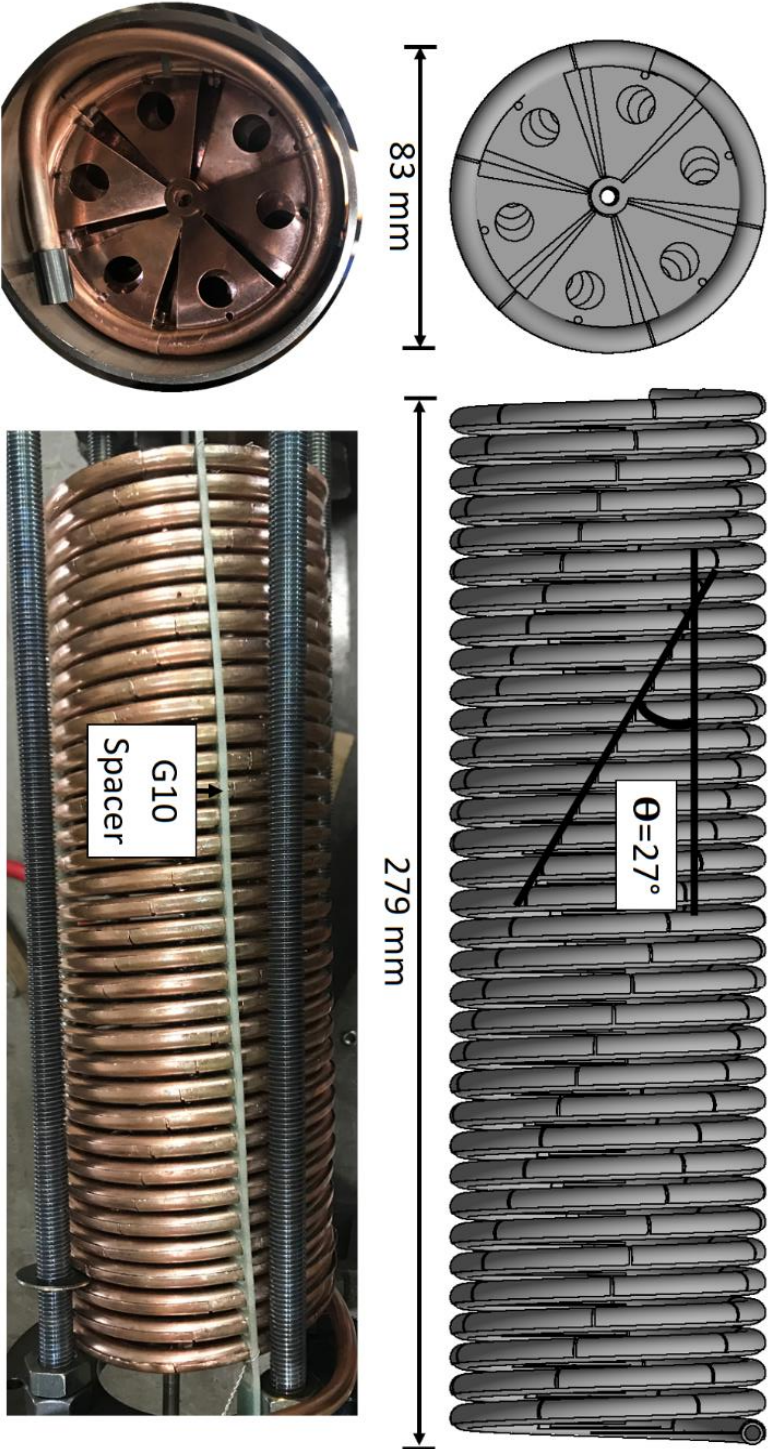


Figure 9-1: CAD model of the 2K HX_2 (above); the manufactured 2K HX_2 (below).

9.2. Experimental Results

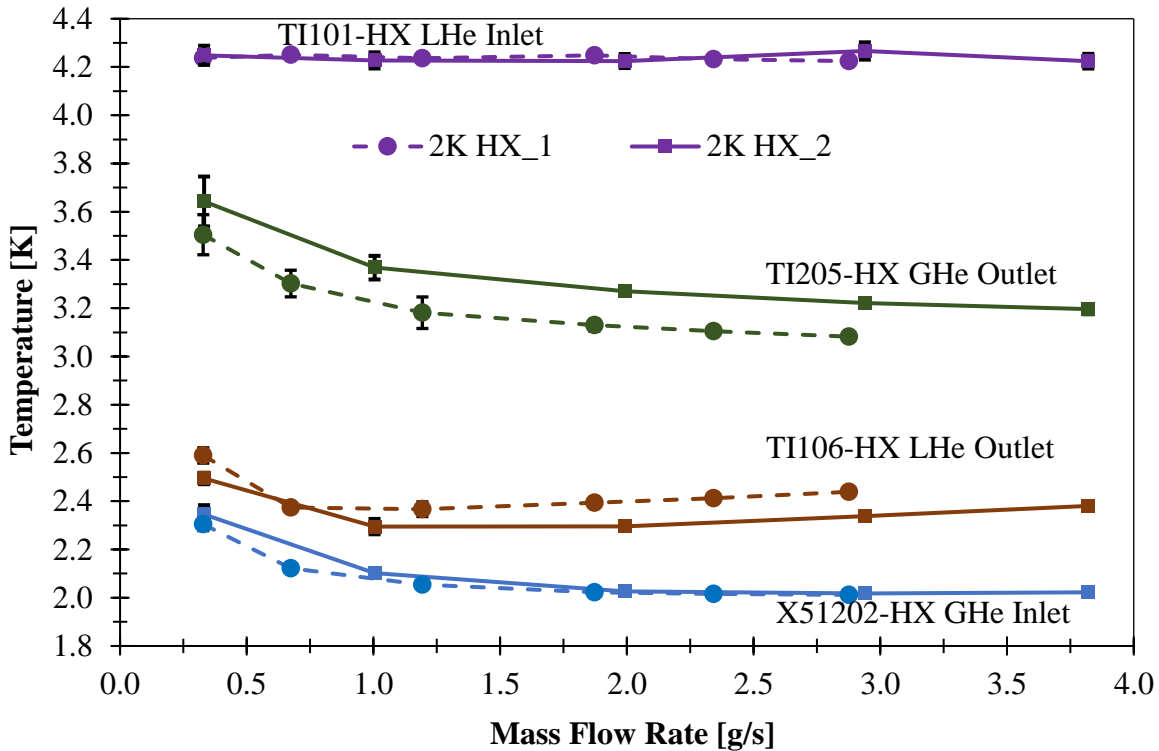


Figure 9-2: 2K HX_2 temperature data compared with the 2K HX_1 at various flow rates.

The performance of the 2K HX_2 was measured using the heat exchanger test stand and is shown in Figure 9-2. The 2K HX_2 performed better with respect to the 2K HX_1, producing approximately 100 mK lower LHe outlet temperature than the 2K HX_1, if the GHe inlet temperature remains at 2.0 K at 3 g/s. The rise in the outlet temperature of the GHe is higher than the drop in the LHe outlet temperature, this being due to the bypassing of the incoming 2.0 K GHe through the 4.7% bypass area, extracting heat in-leak from its SS316 L shell. Also, the higher helix angles in this heat exchanger gives higher heat transfer coefficient, hence higher outlet temperature for the GHe.

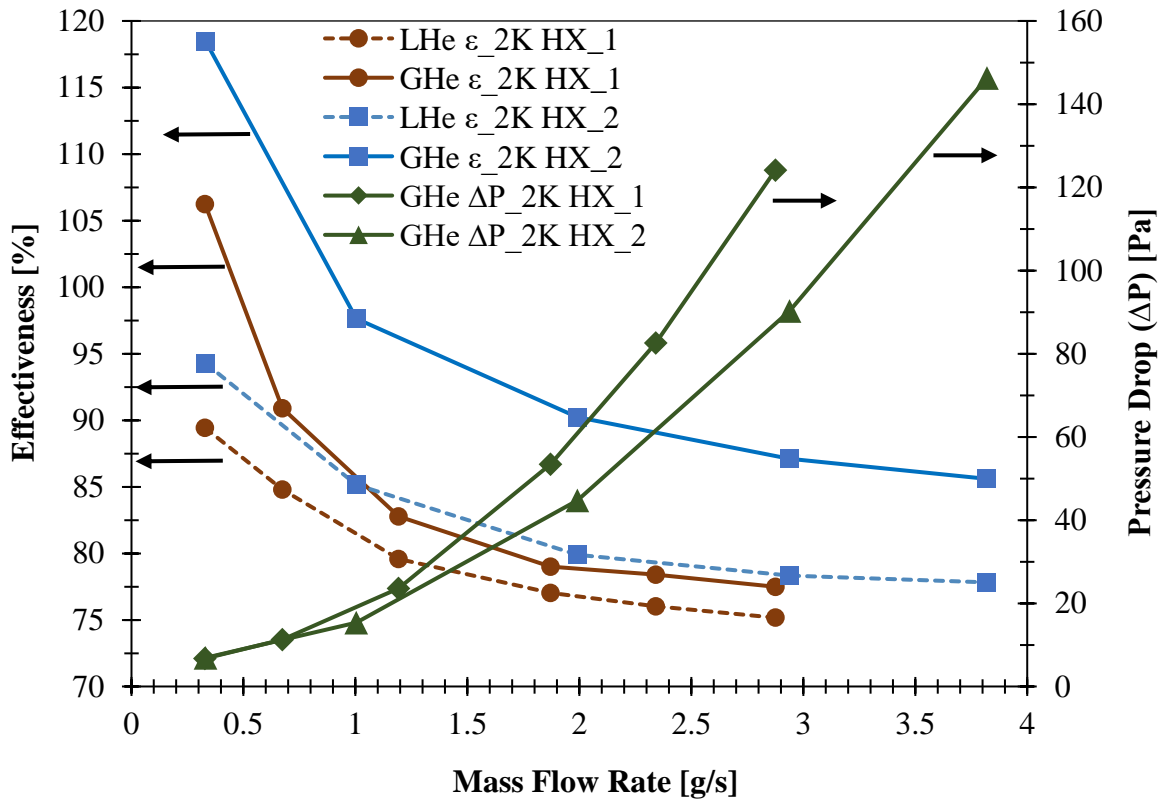


Figure 9-3: 2K HX_2 effectiveness and GHe ΔP compared to the 2K HX_1.

The performance of the 2K HX_2 compared to the 2K HX_1 is shown in Figure 9-3. The obtained LHe effectiveness of the 2K HX_2 was 4% higher, and the GHe ΔP was reduced by 40 Pa compared to the 2K HX_1 at 3 g/s flow rate. The 2K HX_2 has an improved performance with higher effectiveness and lower GHe ΔP . For 2K HX_2, the GHe effectiveness for the flow below 1 g/s shows an effectiveness > 100%, the reasoning for this kind of unusual behavior is given in Section 6.4.1. The effect of the heat in-leak is much more prominent for the 2K HX_2 compared to the 2K HX_1. This happens due to the heat in-leak from the ICF connection for the hot LHe (constant temperature source at 4.2 K) being carried out by the GHe flow from the 4.7% bypass area is more prominent for the 2K HX_2, which will keep on rising as the flow rate of GHe increases. Here, the heat in-leak increased from 0.33 W at 0.33 g/s to 3.8 W at 3.8 g/s, even if the heat in-leak from the surrounding thermal shield remains constant.

9.3. Comparison of the Numerical and Experimental Results for the 2K HX_2

A CAD model was created according to the manufactured heat exchanger geometry to verify the experimental results obtained for the 2K HX_2. The design parameters for the 2K HX_2 shown in Table 9-1 were realized in the manufactured 2K HX_2, and are replicated in its CAD model. The alteration that was necessary to be replicated in the CAD model was the helix diameter of the 2K HX, which had to be increased from 75 mm to 76 mm. The changes shown above reduce the error in the results obtained from the CFD simulation and experimental results. In Figure 9-4, it is noticeable that the effectiveness and GHe ΔP of the manufactured 2K HX is similar to its simulated CAD model at 3g/s flow rate. This simulation was done by considering a constant 2K HX body temperature of 3.6 K, to produce approximately 3.3 K fluid at the outlet to reproduce a condition similar to the actual experiment. The performance parameters of the numerical model for the 2K HX_2 with its experimental results are shown in Table 9-2 and Figure 9-4. The results obtained from the simulated model and the experimentally tested 2K HX are in good agreement with each other and within acceptable error.

Table 9-2: Comparison of experimentally tested 2K HX_2 with respect to 2K HX_1

Performance Parameters	2K HX_1	2K HX_2
<i>Helical tube parameters</i>		
Tube OD (thickness)	$\Phi 6$ (t1) mm	$\Phi 6$ (t1) mm
Helix diameter (pitch)	75 (9) mm	$\Phi 76$ (8) mm
Number of loops	30	34
Helix angle	13°	27°
<i>Total dimensions</i>		
2K HX axial length	277 mm	279 mm
2K HX diameter	$\Phi 82$ mm	$\Phi 83$ mm
Bypass Area	Nil	4.7%
<i>Performance Parameters</i>		
Effectiveness @ 3 g/s	75%	78.4%
GHe ΔP @ 3 g/s	136 Pa	90 Pa
LHe outlet temperature @ 3g/s	2.5 K	2.36 K

Experimental and Numerical Verification of the Optimization Study

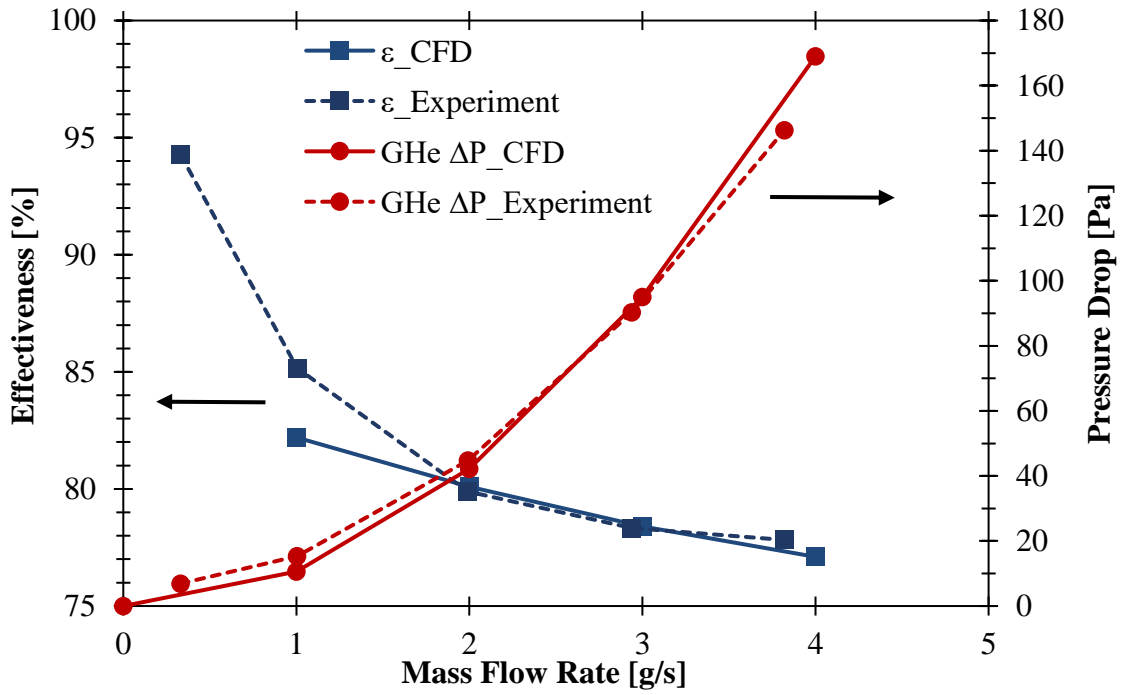


Figure 9-4: Effectiveness and GHe ΔP for the experimentally tested 2K HX_2 and its numerical model.

Chapter 10. CONCLUSION

The performance of the 2K HX_1 was determined experimentally using a heat exchanger test stand. It was found that the effectiveness of the 2K HX_1 was 75% at 3 g/s, less than the required 84% to produce 2.2 K LHe before the JT valve. At the STF and cERL cryogenic facilities, two 2K HX_1 were used in series, this arrangement produces 84% effectiveness due to the doubling of the heat transfer area for the 2.0 K GHe flowing through the heat exchangers. Although this will also double the GHe ΔP through the 2K heat exchangers attached in the cryogenic system. The high GHe ΔP in the 2K HXs combined with the pressure drop in the GHe return line, compels the pumping system to operate at lower inlet pressure to maintain 3.13 kPa vapor pressure on the 2.0 K superfluid helium. The original cooling capacity obtained from the STF and cERL pumping system was approximately 70 W and 80 W at 2.0 K He II, respectively.

The 2K HX_1 design was optimized to maximize the He II production rate from the superfluid helium cryogenic systems while improving its effectiveness and reducing the GHe ΔP . The required effectiveness of 84% at 3 g/s was obtained at a GHe ΔP of 140 Pa for the optimized 2K HX_3. This will improve the pumping capacity of the GHe pumping system, hence the higher He II production rate. The cooling capacity from the STF and cERL superfluid helium cryogenic systems can be improved from 70 W and 80 W at 2.0 K, to 82 W and 92 W respectively, with the aid of the 2K HX_3. This will reduce the cost of buying excess pumps to improve the He II production rate from the cryogenic systems. In the future, only one heat exchanger can act as a replacement for two in series per 2K refrigerator cold box to improve the pumping capacity through the vacuum pumps. The optimization study was validated experimentally by the heat exchanger test stand installed in tandem with the STF's GHe pumping system.

As a general rule suggested by L. Tavian et al. [36] for flow rates < 4.5 g/s, the GHe ΔP of < 100 Pa seems to be a good criteria for the 2K heat exchangers of the superfluid helium cryogenic systems, and this was also observed with the results obtained from the studies.

Conclusion

Moreover, the effectiveness should be $> 84\%$ to reduce the refrigeration load on the cryogenic plants, at that pressure drop. With the current design of the optimized 2K heat exchanger (2K HX_3), effectiveness of $> 84\%$ was achieved, but it was not possible to obtain a GHe ΔP of < 100 Pa at 4.5 g/s flow rate. Although, if the helix diameter of the 2K HX can be increased and the fin design can be modified, it will be possible to achieve that goal for the cryogenic systems at KEK.

Chapter 11. SUGGESTION FOR FURTHER IMPROVEMENT

The fin design can be changed to reduce the friction factor and increase the surface area for heat transfer. It is noticeable that the punched hole on the fin is a significant area that is lost for heat extraction from the LHe. The fin design can be improved to have Louvered-punched fins to keep the area that was lost before and improve the heat transfer capability of the 2K heat exchanger. These kinds of fins will have some sections of them parallel to the GHe flow, hence reducing the friction factor while increasing the heat transfer area.

An additional work that can be performed is to increase the size of this heat exchanger comparable to the ones that were tested at CERN, to compare the performance of this heat exchanger in scale with those 2K heat exchangers. If a better fin design is combined with increasing the size of this heat exchanger, the GHe pressure drop can be kept comparable to the ones at CERN.

REFERENCES

- [1] S. Cousineau, J. Holmes, and Y. Zhang, “Introduction to Accelerators : Evolution of Accelerators and Modern Day Applications,” *Uspas 2011*, 2011.
- [2] H. Wiedemann, *Partide Accelerator Physics I & II*, no. 1. 2003.
- [3] H. Podlech, “Superconducting versus normal conducting cavities,” *Cern Accel. Sch. High Power Hadron Mach. CAS 2011 - Proc.*, pp. 151–170, 2013, doi: 10.5170/CERN-2013-001.151.
- [4] L. Evans, “LHC machine,” p. 004, 2018, doi: 10.22323/1.084.0004.
- [5] “Operation of the XFEL Accelerator,” *Deutsches Elektronen-Synchrotron (DESY)*. .
- [6] S. W. Van Sciver, *Helium Cryogenics*, 2nd ed. Springer Berlin Heidelberg, 2012.
- [7] R. F. Barron, *Cryogenic Systems*. Oxford University Press.
- [8] P. Lebrun and L. Taviani, “Cooling with superfluid helium,” *CAS-CERN Accel. Sch. Supercond. Accel. - Proc.*, pp. 453–476, 2014, doi: 10.5170/CERN-2014-005.453.
- [9] L. Decker, C. Ueresin, and P. Treite, “Design of cold compressor systems in terms of operational and economical aspects,” *IOP Conf. Ser. Mater. Sci. Eng.*, vol. 101, no. 1, 2015, doi: 10.1088/1757-899X/101/1/012007.
- [10] V. Ravindranath *et al.*, “Process simulations for the LCLS-II cryogenic systems,” *IOP Conf. Ser. Mater. Sci. Eng.*, vol. 278, no. 1, 2017, doi: 10.1088/1757-899X/278/1/012106.
- [11] R. K. Shah and D. P. Sekulic, *Fundamentals of Heat Exchanger Design*. John Wiley & Sons.
- [12] P. Roussel, “Performance tests of industrial prototype subcooling helium heat exchangers for the Large Hadron Collider,” vol. 1429, no. May 2002, pp. 1429–1436, 2003, doi: 10.1063/1.1472174.

References

- [13] J. Yoshida, K. Hosoyama, H. Nakai, K. Hara, Y. Kojima, and K. Nakanishi, “Development of STF cryogenic system in KEK,” in *IEEE Particle Accelerator Conference (PAC)*, 2007, pp. 2701–2703, doi: 10.1109/PAC.2007.4440357.
- [14] P. K. Gupta and R. Rabehl, “Numerical modeling of a 2 K J-T heat exchanger used in Fermilab Vertical Test Stand VTS-1,” *Cryogenics (Guildf)*, vol. 62, pp. 31–36, 2014, doi: 10.1016/j.cryogenics.2014.03.018.
- [15] C. Adolphsen *et al.*, “The International Linear Collider Technical Design Report - Volume 3.I: Accelerator R&D in the Technical Design Phase,” 2013. [Online]. Available: <http://arxiv.org/abs/1306.6353>.
- [16] J. Polinski, M. Chorowski, P. Duda, Y. Bozhko, B. Petersen, and J. Schaffran, “Design and commissioning of vertical test cryostats For XFEL superconducting cavities measurements,” *AIP Conf. Proc.*, vol. 1573, no. February, pp. 1214–1221, 2014, doi: 10.1063/1.4860844.
- [17] H. Nakai *et al.*, “Superfluid helium cryogenic systems for superconducting RF cavities at KEK,” *AIP Conf. Proc.*, vol. 1573, pp. 1349–1356, 2014, doi: 10.1063/1.4860863.
- [18] A. Kumar *et al.*, “Experimental and numerical investigation of 2 K heat exchanger for superfluid helium cryogenic systems at KEK,” *IOP Conf. Ser. Mater. Sci. Eng.*, vol. 755, no. 1, 2020, doi: 10.1088/1757-899X/755/1/012061.
- [19] A. Kumar *et al.*, “Performance analysis for 2K heat exchanger for superfluid cryogenic system at KEK,” *IOP Conf. Ser. Mater. Sci. Eng.*, vol. 502, no. 1, 2019, doi: 10.1088/1757-899X/502/1/012051.
- [20] “ANSYS CFX-Solver Theory Guide.”
- [21] “ANSYS CFX-Solver Modeling Guide,” 2017.
- [22] “CFX-PRE.”
<https://intranet.birmingham.ac.uk/as/libraryservices/library/digitaltechnologyskills/d>

References

ocuments/public/cfxpre.pdf.

- [23] ANSYS, “ANSYS CFX-Pre User’s Guide,” 2013.
- [24] “HEPAK.” Horizon Technologies.
- [25] NIST, “Thermophysical properties of fluid systems.”
<https://webbook.nist.gov/chemistry/fluid/>.
- [26] N. T. Basse, “Turbulence intensity scaling: A fugue,” *Fluids*, vol. 4, no. 4, 2019, doi: 10.3390/fluids4040180.
- [27] F. Russo and N. T. Basse, “Scaling of turbulence intensity for low-speed flow in smooth pipes,” vol. 15, no. October 2015, p. 5986, 2004, doi: 10.1016/j.flowmeasinst.2004.02.001.
- [28] “TURBULENCE PART 3 - SELECTION OF WALL FUNCTIONS AND Y+ TO BEST CAPTURE THE TURBULENT BOUNDARY LAYER,” 2013.
<https://www.computationalfluidynamics.com.au/wp-content/uploads/2013/04/wallfunction.png>.
- [29] F. R. Menter, J. C. Ferreira, and T. Esch, “The SST Turbulence Model with Improved Wall Treatment for Heat Transfer Predictions in Gas Turbines,” *Int. Gas Turbine Congr. 2003*, no. 1992, pp. 1–7, 2003, [Online]. Available: http://nippon.zaidan.info/seikabutsu/2003/00916/pdf/igt2003tokyo_ts059.pdf.
- [30] F. P. Incropera and D. P. DeWitt, *Fundamentals of Heat and Mass Transfer*, 6th Editio. Wiley & Sons, 1996.
- [31] P. G. Kroeger, “Performance Deterioration in High Effectiveness Heat Exchangers Due to Axial Heat Conduction Effects,” *Adv. Cryog. Eng.*, pp. 363–372, 1967, doi: 10.1007/978-1-4757-0489-1_38.
- [32] NIST, “Material Properties: OFHC Copper (UNS C10100/C10200).”
https://trc.nist.gov/cryogenics/materials/OFHC_Copper/OFHC_Copper_rev1.htm.

References

- [33] W. M. Kays and A. L. London, *Compact Heat Exchangers*, Second. McGraw-Hill Book Company, 1964.
- [34] K. Sadic and L. Hongtan, *Heat Exchangers: Selection, Rating and Thermal Design*. CRC Press, 2002.
- [35] S. Ali, “Pressure drop correlations for flow through regular helical coil tubes,” *Fluid Dyn. Res.*, vol. 28, no. 4, pp. 295–310, 2001, doi: 10.1016/S0169-5983(00)00034-4.
- [36] L. Taviani, B. Jager, and P. Roussel, “A cryogenic test station for subcooling helium heat exchangers for LHC,” Geneva.
- [37] A. Adamczyk, S. Pietrowicz, and J. Fydrych, “Heat transfer resistances in the measurements of cold helium vapour temperature in a subatmospheric process line,” *IOP Conf. Ser. Mater. Sci. Eng.*, vol. 171, no. 1, 2017, doi: 10.1088/1757-899X/171/1/012139.
- [38] R. Müller and M. Süßer, “Comparison of cryogenic temperature sensor installation inside or outside the piping,” *AIP Conf. Proc.*, vol. 1218, pp. 1641–1646, 2010, doi: 10.1063/1.3422347.
- [39] N. Rott, “Thermally driven acoustic oscillations. Part II: Stability limit for helium,” *Zeitschrift für Angew. Math. und Phys. ZAMP*, vol. 24, no. 1, pp. 54–72, 1973, doi: 10.1007/BF01593998.
- [40] N. Rott, “Damped and thermally driven acoustic oscillations in wide and narrow tubes,” *Zeitschrift für Angew. Math. und Phys. ZAMP*, vol. 20, no. 2, pp. 230–243, 1969, doi: 10.1007/BF01595562.
- [41] H. Luck and C. Trepp, “Thermoacoustic oscillations in cryogenics. Part 3: avoiding and damping of oscillations,” *Cryogenics (Guildf.)*, vol. 32, no. 8, pp. 703–706, 1992, doi: 10.1016/0011-2275(92)90279-J.
- [42] “LCLS-II: A World-Class Discovery Machine,” *Stanford Linear Accelerator (SLAC)*. <https://lcls.slac.stanford.edu/lcls-ii>.

References

- [43] “First turns and successful storage of beams in the SuperKEKB electron and positron rings,” *High Energy Accelerator Research Organization (KEK)*, 2016.
<https://www.kek.jp/en/NewsRoom/Release/20160302163000/>.

ACKNOWLEDGMENTS

My first thanks and sincere gratitude goes to my supervisor **Prof. Nakai Hirotaka**, without his relentless help and constant guidance it would not have been possible for me to complete this work. He is not only an erudite supervisor but also an icon of inspiration whose encouragement inspired me to fulfill my tasks. He allowed me to make my own decisions, lots of mistakes and was patient enough to let me learn from them. He has helped me from prologue to epilogue and I remain ever grateful to him.

I am especially indebted to **Assoc. Prof. Nakanishi Kota** and **Assis. Prof. Shimizu Hirotaka** who has advised and inspired me days in and out with their constant support and experience. Their assistance throughout the course and useful discussions helped me improve this research tremendously. They always made sure to ask the right questions to improve the quality of the research presented in the thesis.

My special thanks to **Mr. Hara Kazufumi**, **Mr. Kojima Yuji** and **Mr. Honma Teruya** for their help and expertise. I learnt a lot from them about designing and experimentation techniques in the field of Accelerator cryogenics. Without their help it would not be possible to conduct such a large scale experiment. I am also thankful to the personnel of **Hitachi group** for assisting and supporting this work. Also, my special thanks to **Dr. Mori Shingo** for the fruitful discussions in understanding the basics of thermo-acoustic oscillations and Mathematica®.

I would also like to extend my gratitude to **The Graduate University for Advanced Studies (SOKENDAI)**, **High Energy Accelerator Research Organization (KEK)** and **Ministry of Education, Culture, Sports, Science and Technology (MEXT)** for allowing me to pursue Ph.D. course in this facility, providing the necessary support and funding to this work.

Parents are next to God and I would like to thank my parents **Hon. Lt. (IN) Dharam Prakash (Rtd.)** and **Mrs. Santosh Devi** for their numerous sacrifices and ever increasing unconditional love. Special thanks to my siblings **Mrs. Jyoti Sharma** and **Mr. Akshay Kumar** for providing much needed support throughout my Ph.D journey.

APPENDICES

A. Cernox Sensor Calibration Curves

All the data shown below was calibrated at 1 μ A excitation current to the uncalibrated Cernox® sensors with respect to a calibrated Cernox™ sensor and Baratron Pressure transmitter from Lakeshore® and MKS®, respectively.

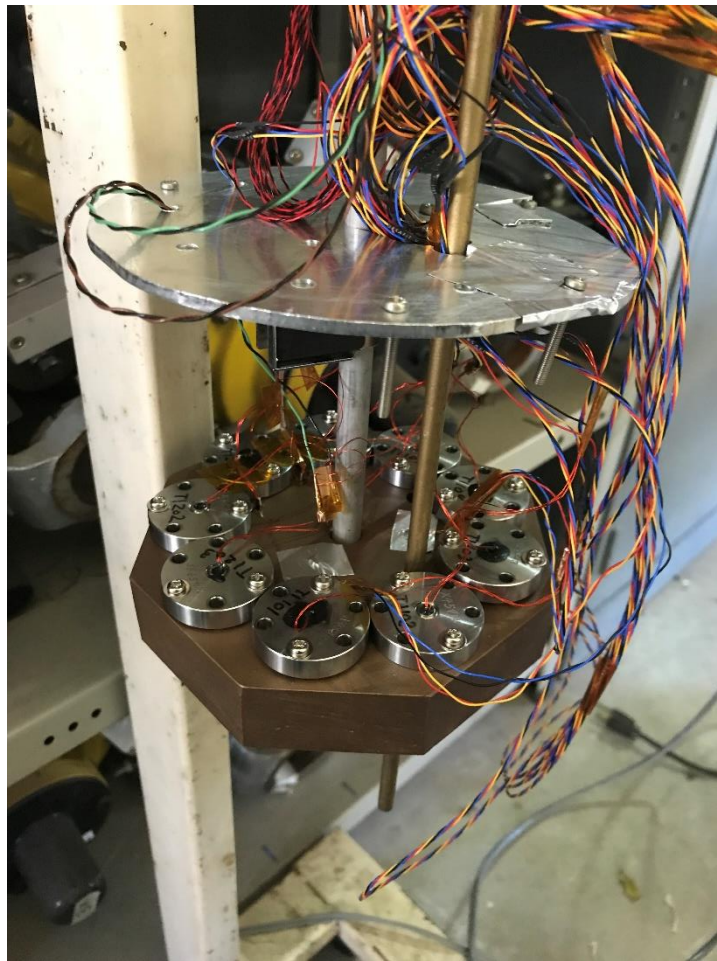


Figure A.1. Cernox sensor calibration setup

TI101

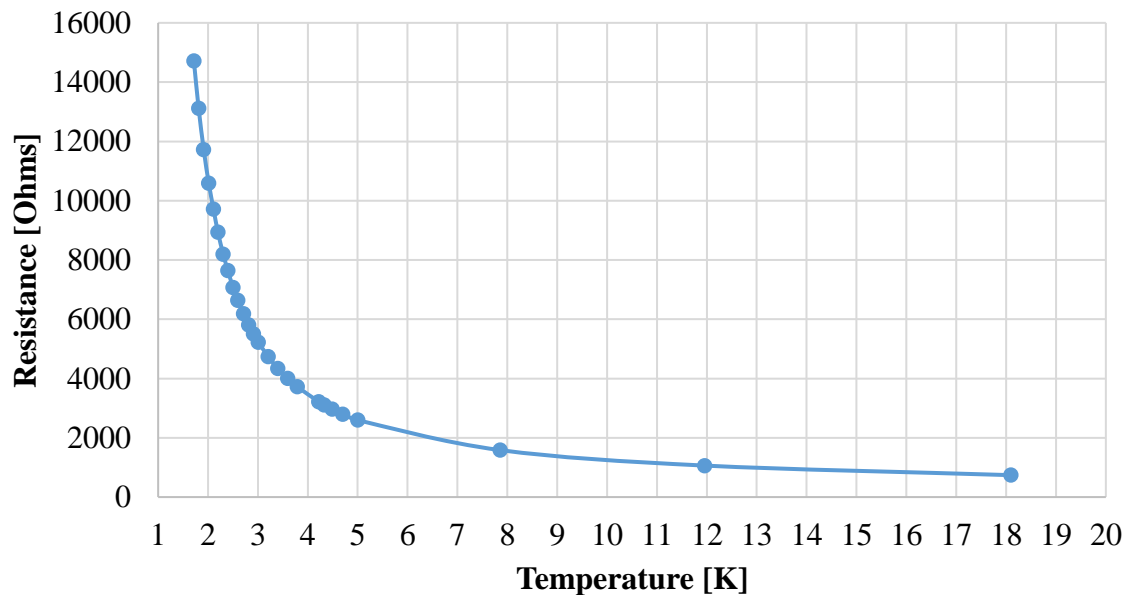


Figure A.2. TI101 Calibration curve

TI106

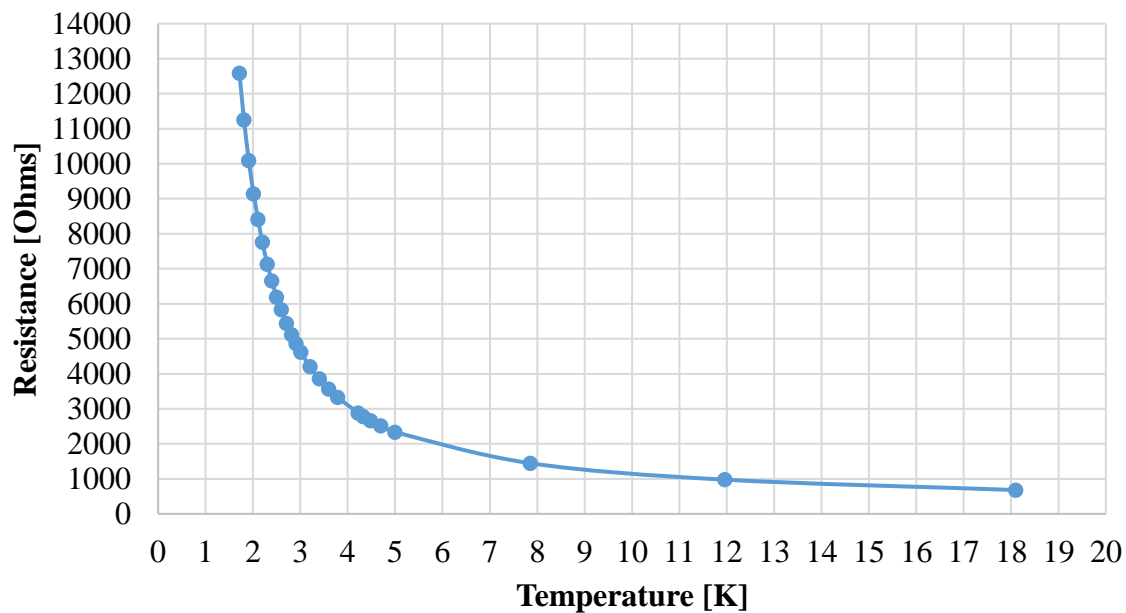


Figure A.3. TI106 Calibration curve

TI103

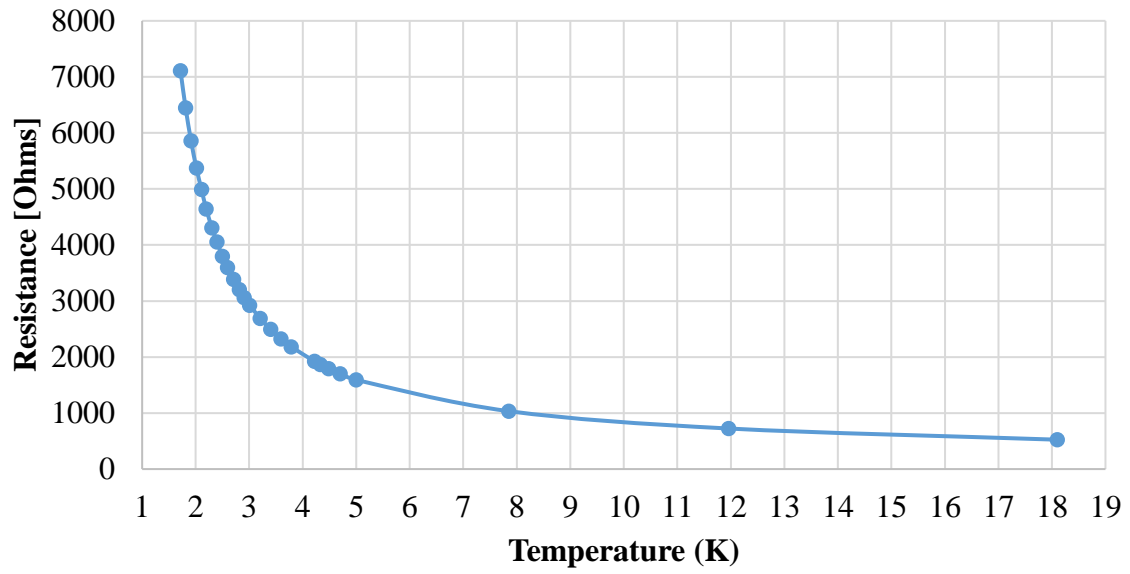


Figure A.4. TI103 Calibration curve

TI205

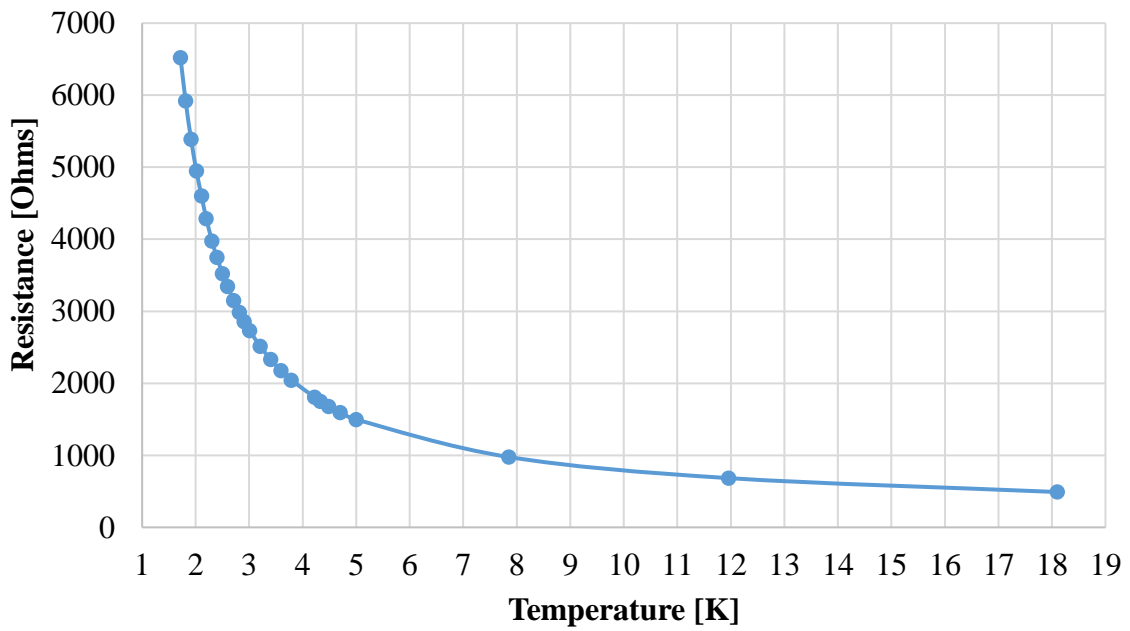


Figure A.5. TI205 Calibration curve

X51202

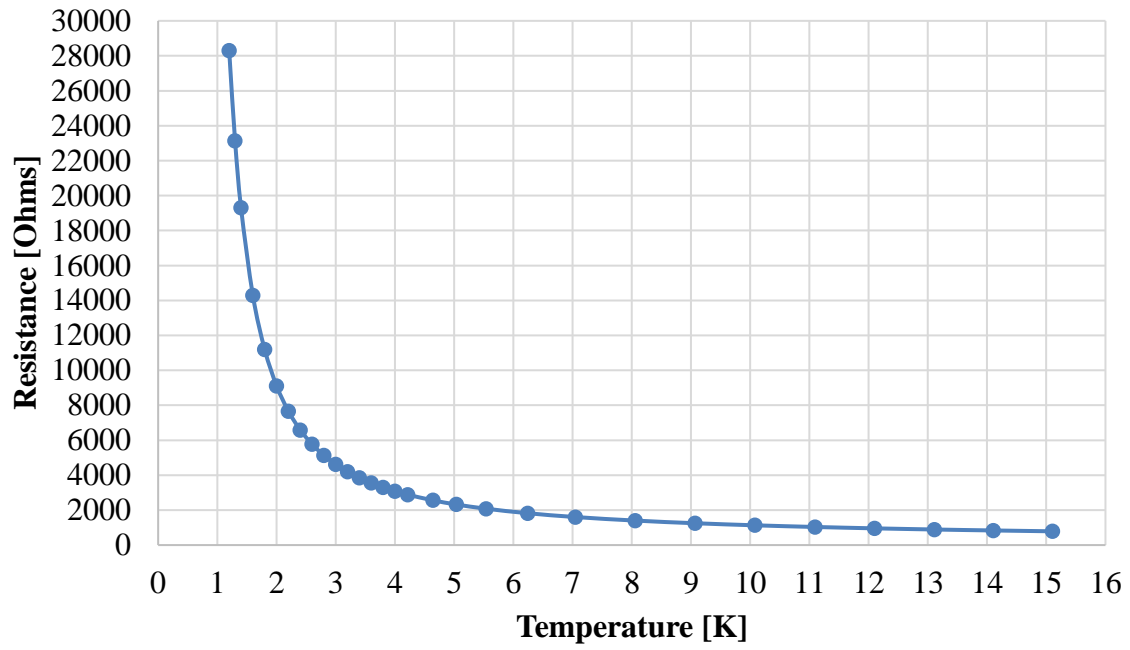


Figure A.6. X51202 Calibration curve

B. Property of Gaseous Helium

GHe Density at 2.8 kPa

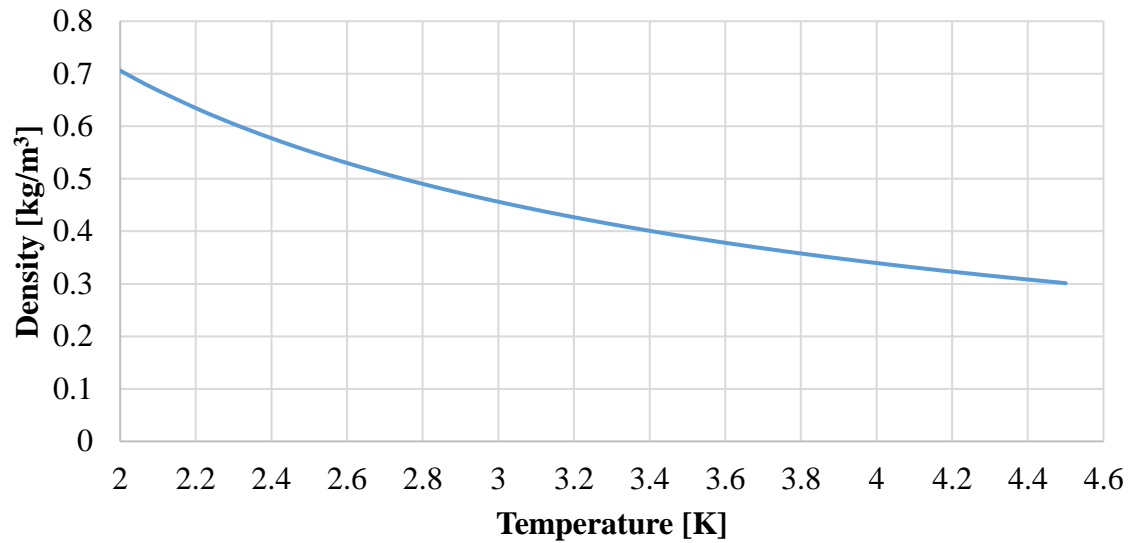


Figure B.1. Density variation of GHe w.r.t temperature at 2.8 kPa

GHe Specific Heat Capacity at 2.8 kPa

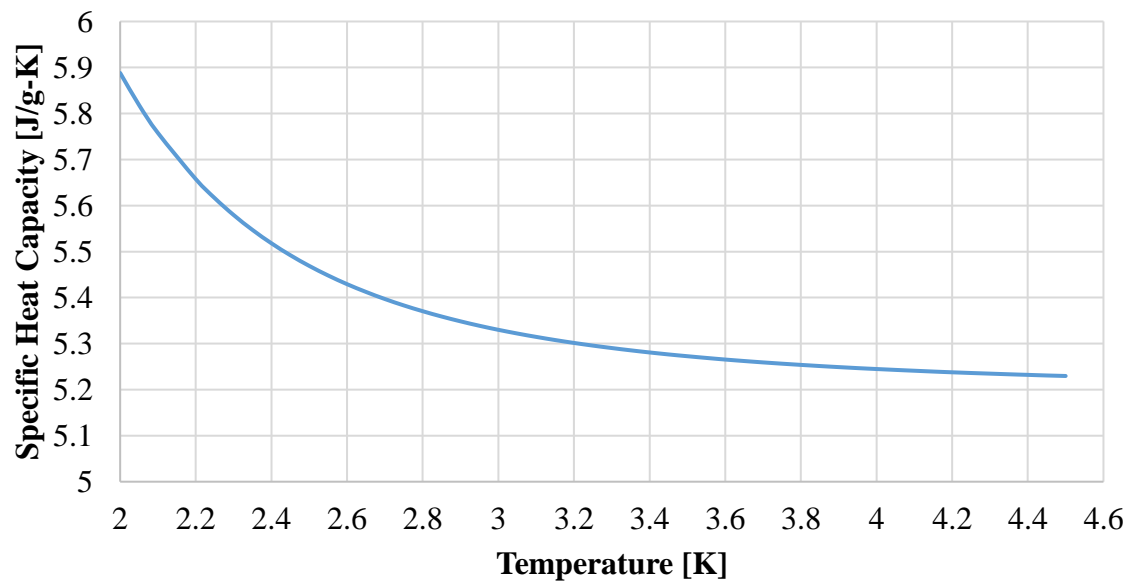


Figure B.2. Specific heat capacity variation of GHe w.r.t temperature at 2.8 kPa

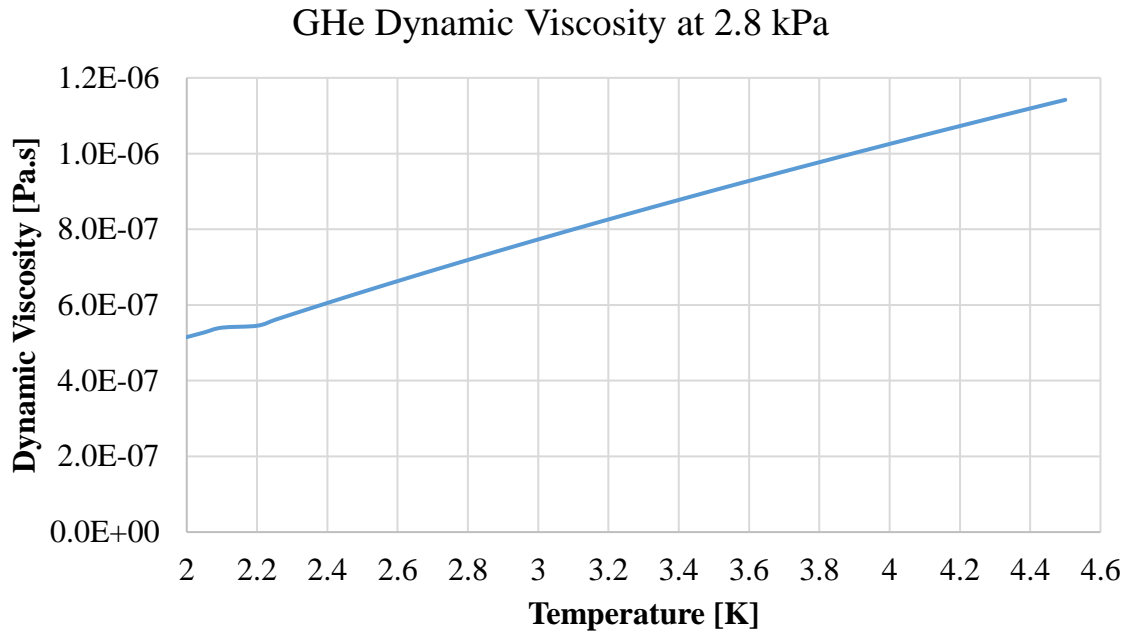


Figure B.3. Dynamic viscosity variation of GHe w.r.t temperature at 2.8 kPa

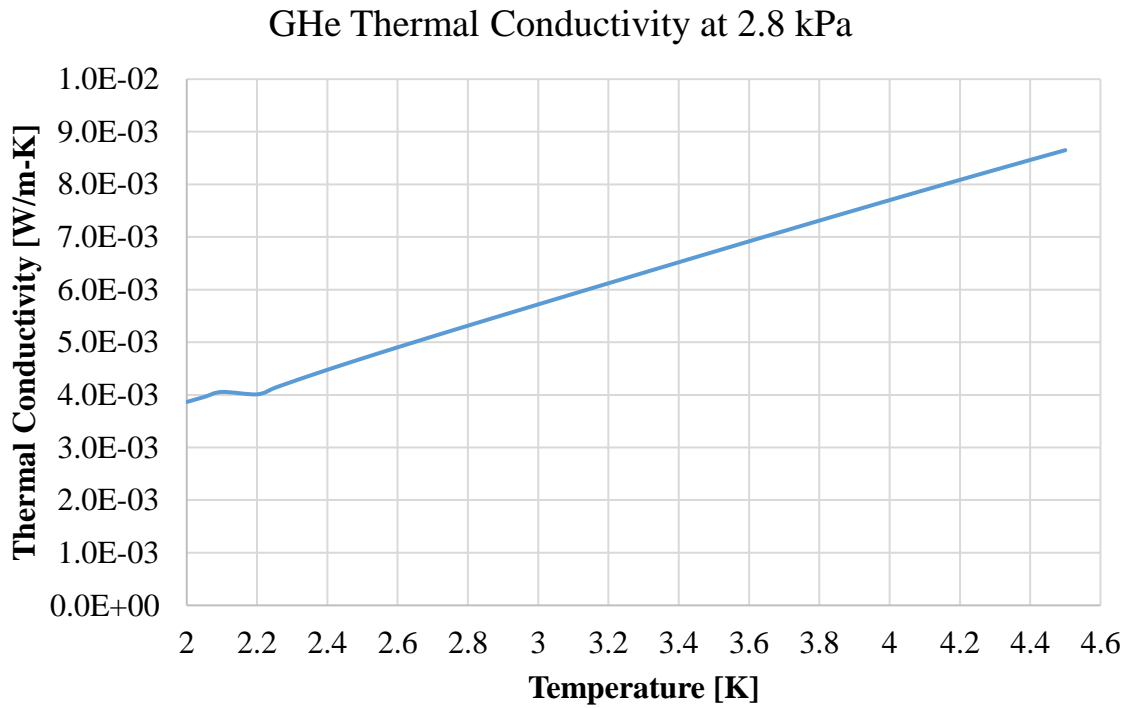


Figure B.4. Thermal conductivity variation of GHe w.r.t temperature at 2.8 kPa

C. Property of Liquid Helium

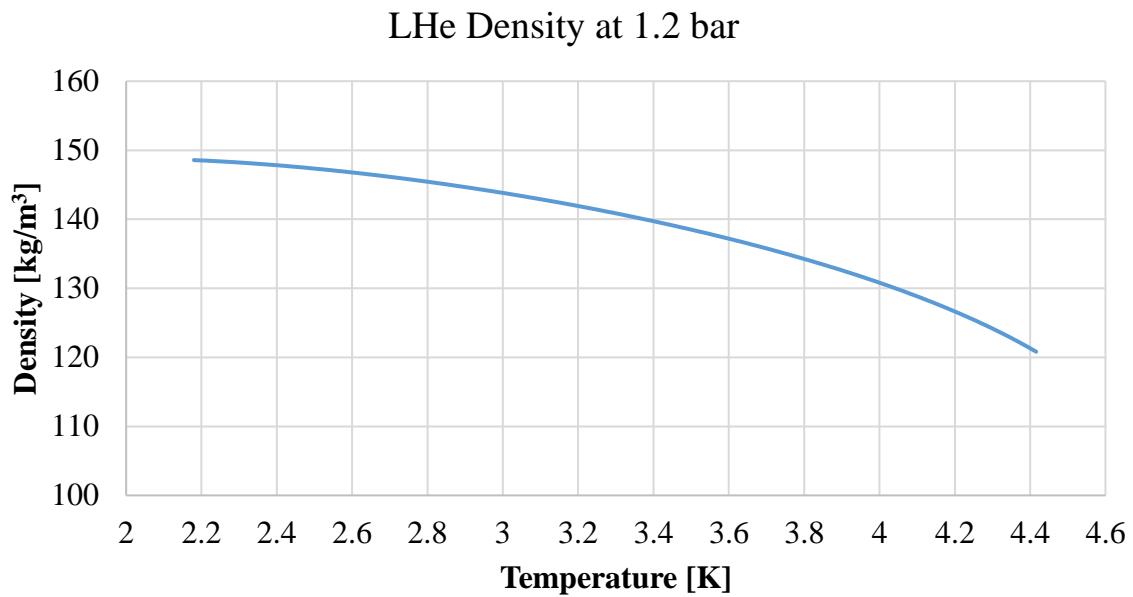


Figure C.1. Density variation of LHe w.r.t temperature at 120 kPa

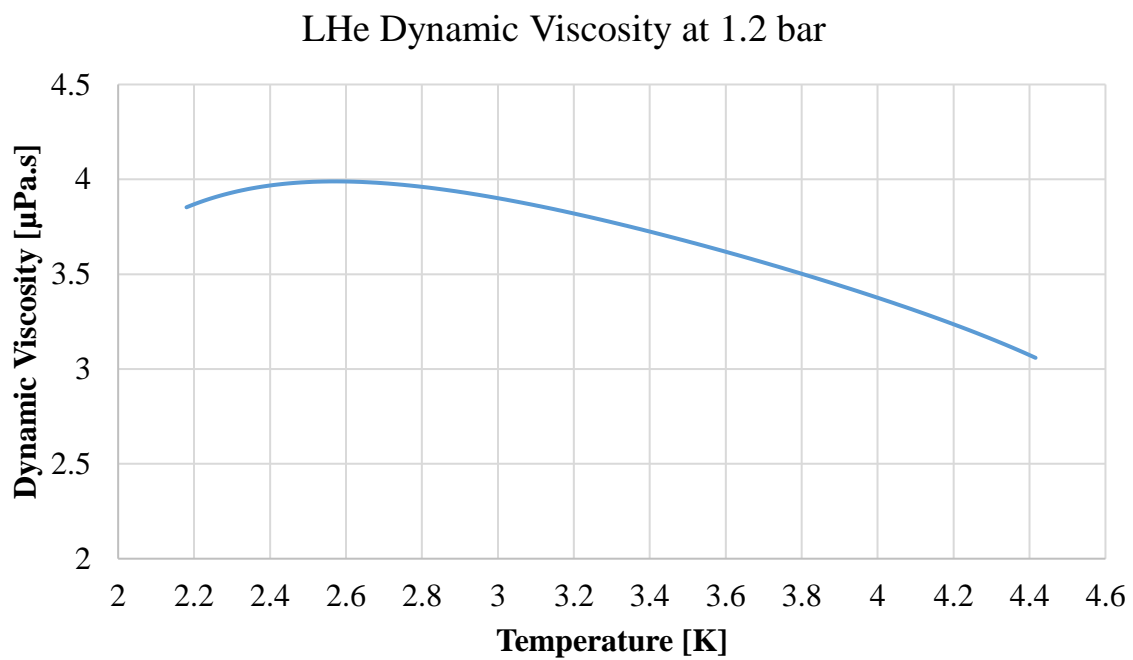


Figure C.2. Specific heat capacity variation of LHe w.r.t temperature at 120 kPa

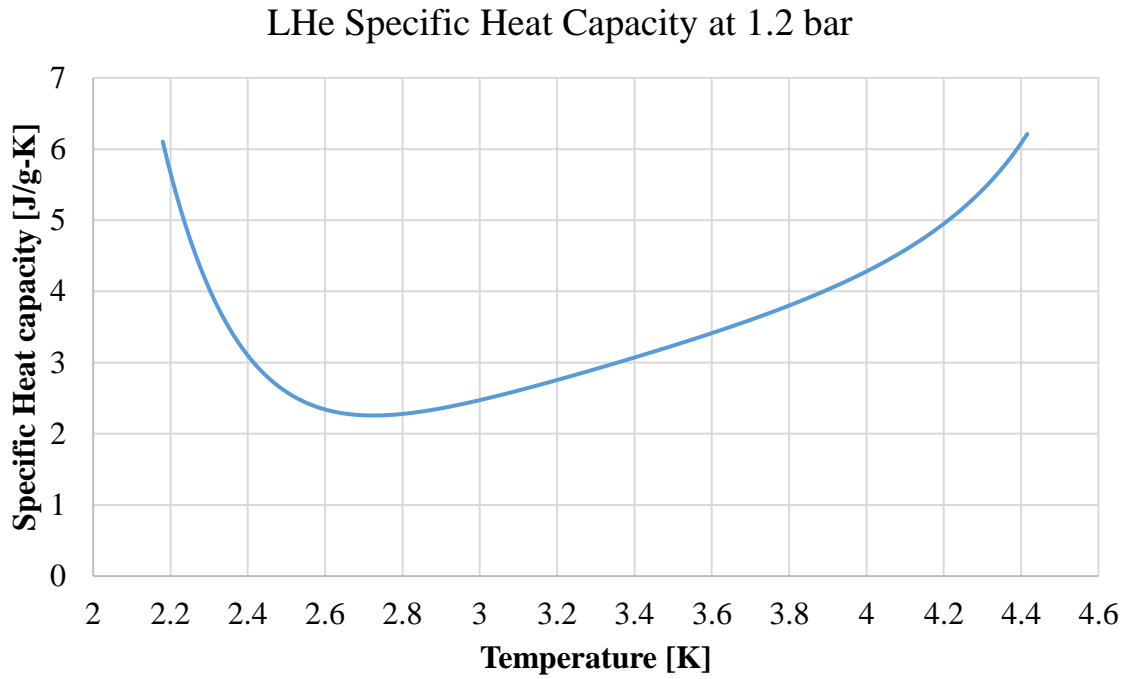


Figure C.3. Dynamic viscosity variation of LHe w.r.t temperature at 120 kPa

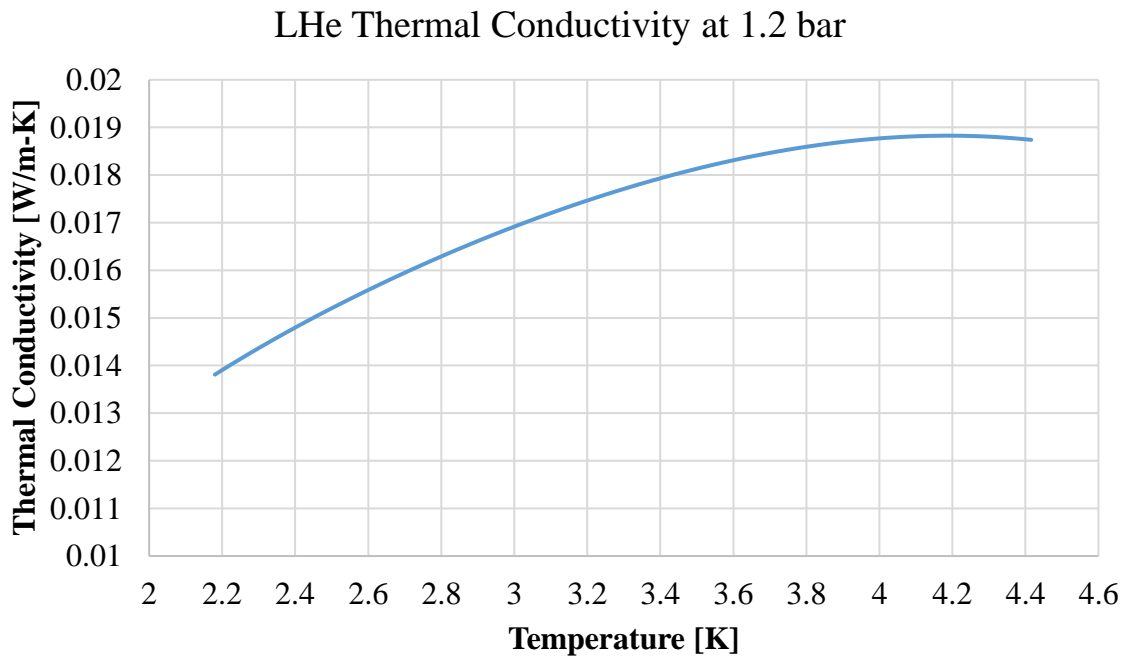


Figure C.4. Thermal conductivity variation of LHe w.r.t temperature at 120 kPa

D. Mathematica Code for Determining Heat Exchanger Temperature Profile.

```
In[15]:= lah = {2031.150226, -3544.562902, 2573.429763, -994.4315776, 215.7754937, -24.92801291, 1.19820922};
lac = {28.73496894, -34.30987546, 21.30627886, -7.135224617, 1.350769599, -0.136546524, 0.005744547};
(*Constants for curve fitting Specific Heat Capacity of fluids!*)

{Th'[x] == 
$$\frac{-UA}{\text{Sum}[lah[[i]] Th[x]^{i-1}, \{i, 1, 7\}] * 1000 * L * mh} (Th[x] - Tc[x]),$$

Tc'[x] == 
$$\frac{-UA}{\text{Sum}[lac[[i]] Tc[x]^{i-1}, \{i, 1, 7\}] * 1000 * L * mc} (Th[x] - Tc[x]), Tc[L] == TcL, Th[0] == Th0}$$

(*Governing equation for 2K HX!*)

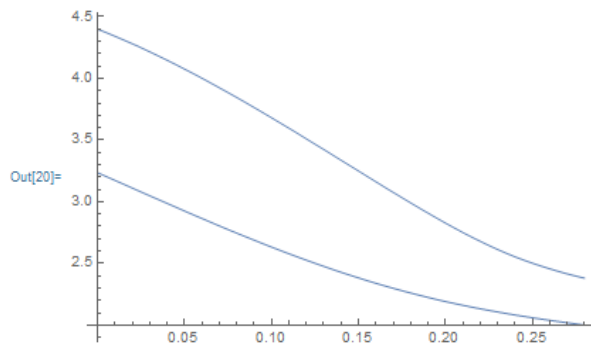
% /. {UA -> 23.8, mh -> 0.002992, mc -> 0.002992, L -> 0.28, TcL -> 2.0, Th0 -> 4.4}
(*Parameters and boundary conditions for governing equation!*)

sol = NDSolve[%, {Th, Tc}, x] (*Numerical Solution for the Governing Equation!*)
Plot[{Th[x], Tc[x]} /. sol, {x, 0, 0.28}]
Table[{Th[x], Tc[x]} /. sol, {x, 0, 0.28, 0.01}]
```

```
Out[17]:= {Th'[x] ==
- ((UA (-Tc[x] + Th[x])) / (1000 L mh (2031.15 - 3544.56 Th[x] + 2573.43 Th[x]^2 - 994.432 Th[x]^3 + 215.775
Th[x]^4 - 24.928 Th[x]^5 + 1.19821 Th[x]^6))),
Tc'[x] == - ((UA (-Tc[x] + Th[x])) / (1000 L mc (28.735 - 34.3099 Tc[x] + 21.3063 Tc[x]^2 - 7.13522 Tc[x]^3 +
1.35077 Tc[x]^4 - 0.136547 Tc[x]^5 + 0.00574455 Tc[x]^6))), Tc[L] == TcL, Th[0] == Th0}
```

```
Out[18]:= {Th'[x] == - ((28.4091 (-Tc[x] + Th[x])) / (2031.15 - 3544.56 Th[x] +
2573.43 Th[x]^2 - 994.432 Th[x]^3 + 215.775 Th[x]^4 - 24.928 Th[x]^5 + 1.19821 Th[x]^6)),
Tc'[x] == - ((28.4091 (-Tc[x] + Th[x])) / (28.735 - 34.3099 Tc[x] + 21.3063 Tc[x]^2 - 7.13522 Tc[x]^3 +
1.35077 Tc[x]^4 - 0.136547 Tc[x]^5 + 0.00574455 Tc[x]^6)), Tc[0.28] == 2., Th[0] == 4.4}
```

```
Out[19]:= {{Th -> InterpolatingFunction[ Domain: {{0., 0.28}}
Output: scalar ],
Tc -> InterpolatingFunction[ Domain: {{0., 0.28}}
Output: scalar ]}}
```



E. Supplementary Heat Exchanger Test Stand Pictures

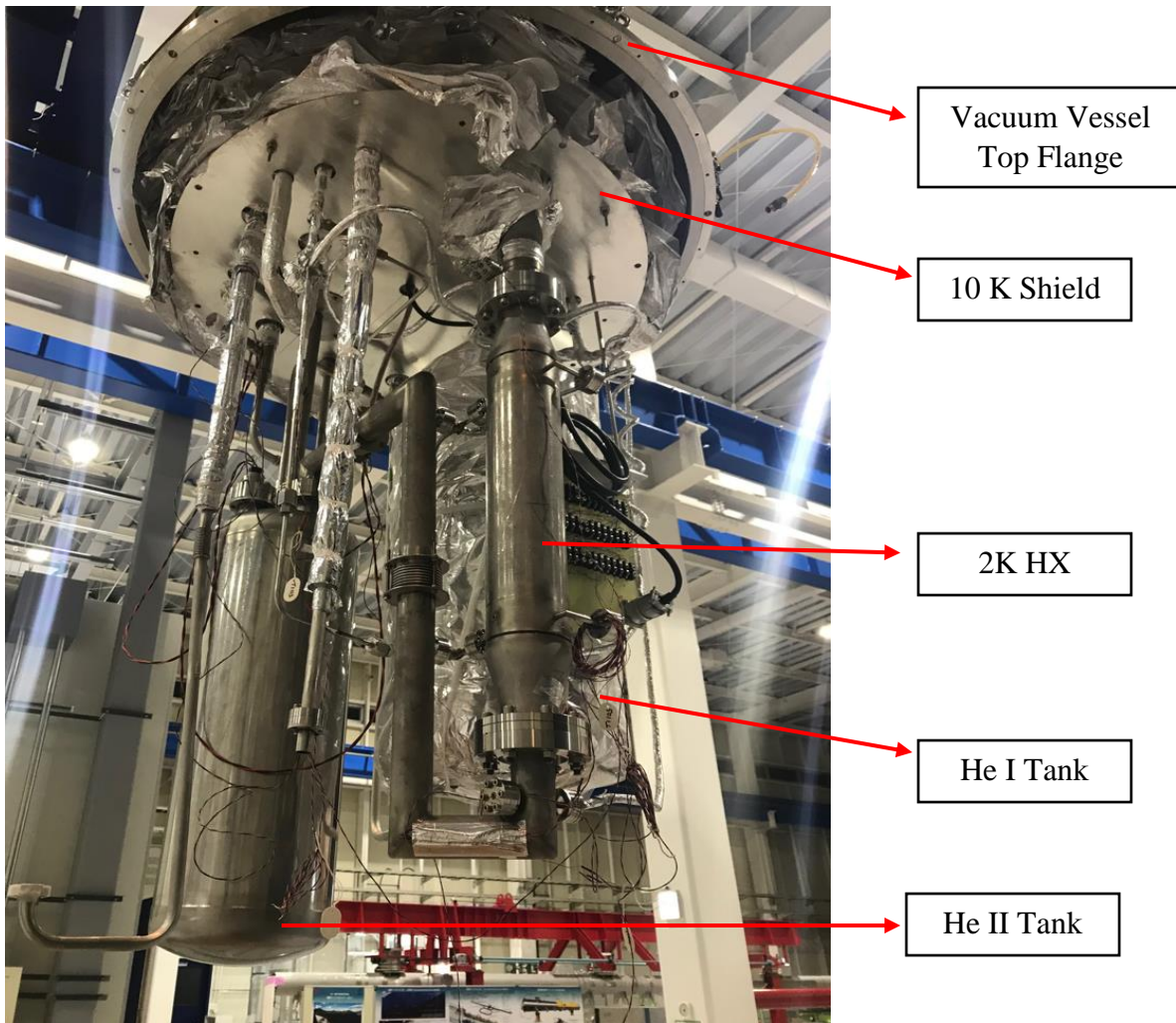


Figure E.1. Inside heat exchanger test stand's 2K cold box.

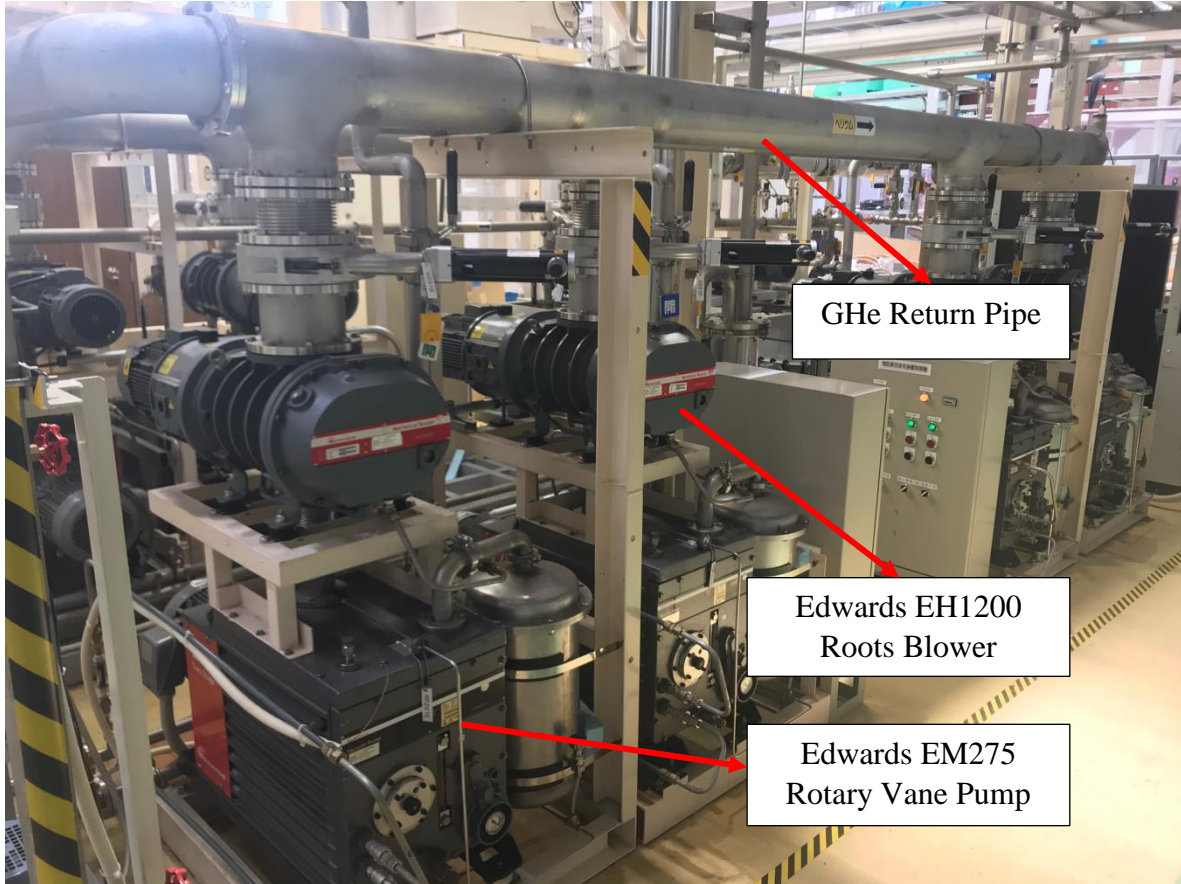
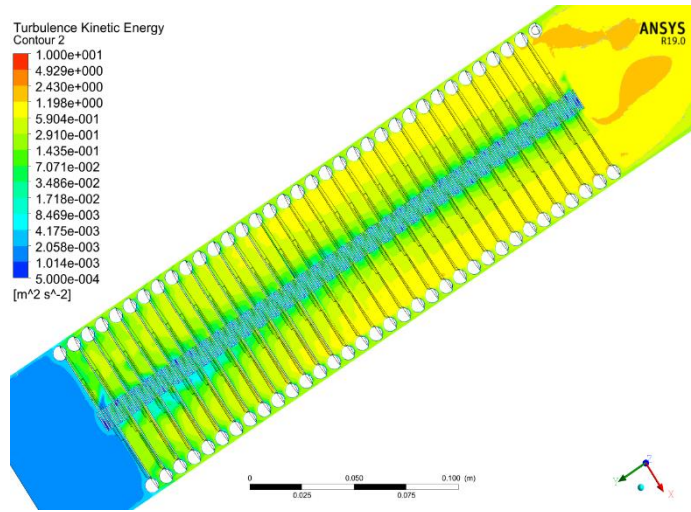
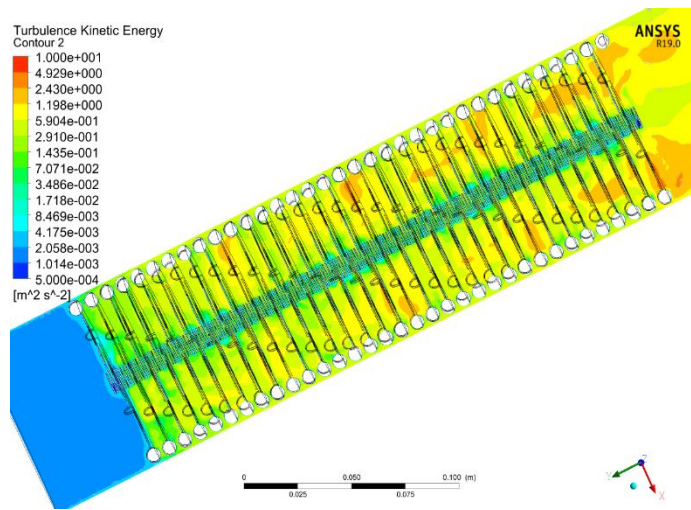


Figure E.2. GHe Pumping system at cERL

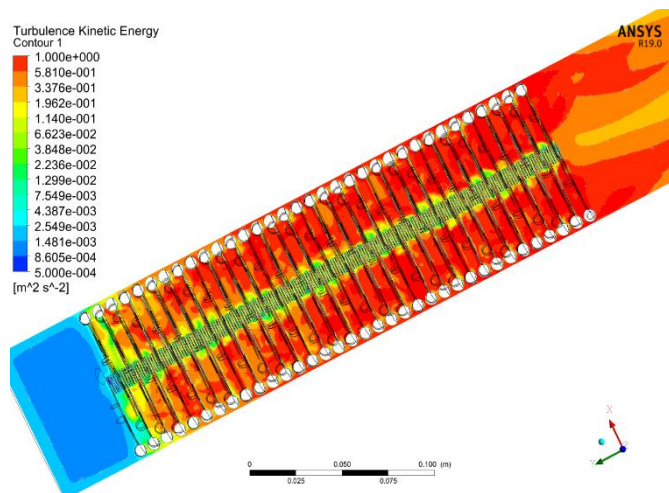
F. Supplementary Figures and Graphs



Helix angle: 0°



Helix angle: 33°



Helix angle: 51°

Figure F.1. Turbulence kinetic energy at various helix angle for Improved 2K HXs from figure 7-11 and 7-12.

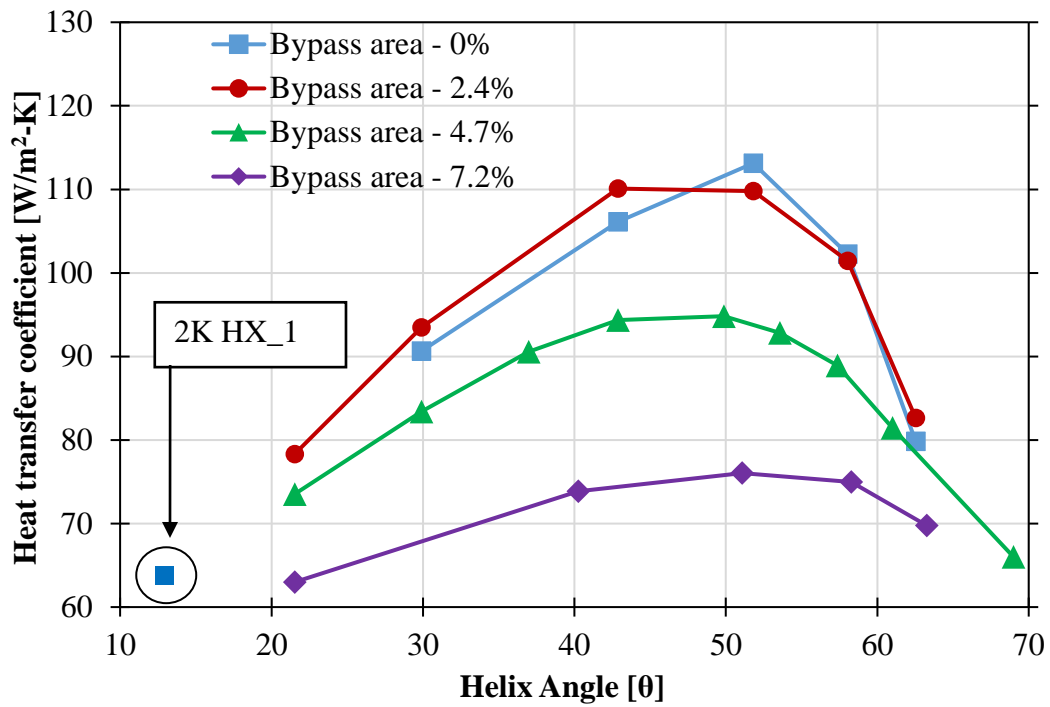


Figure F.2. Heat transfer coefficient for the 2K HXs with varied helix angle and bypass area at 3 g/s.

Appendices